

Spin-related transport phenomena in HgTe-based quantum well structures

Dissertation zur Erlangung des
naturwissenschaftlichen Doktorgrades der
Bayerischen Julius-Maximilians-Universität Würzburg

vorgelegt von
MARKUS KÖNIG
aus Würzburg

Würzburg
Dezember 2007

Eingereicht am 20.12.2007

bei der Fakultät für Physik und Astronomie

1. Gutachter: Prof. Dr. Hartmut Buhmann
 2. Gutachter: PD Dr. Lukas Worschech
 3. Gutachter: Prof. Dr. Sergey Ganichev
- der Dissertation.

1. Prüfer: Prof. Dr. Hartmut Buhmann
 2. Prüfer: PD Dr. Lukas Worschech
 3. Prüfer: Prof. Dr. Björn Trauzettel
- im Promotionskolloquium.

Tag des Promotionskolloquium: 04.04.2008

Doktorurkunde ausgehändigt am:

Contents

Introduction	1
1 HgTe based quantum wells	5
1.1 Band structure of HgTe-based quantum wells	7
1.2 Rashba spin-orbit interaction	11
1.3 Sample fabrication	15
1.4 Summary	18
2 Investigation of the band structure	21
2.1 Transition from n- to p-conductance	22
2.2 Landau levels in HgTe	30
2.3 Summary	38
3 The Quantum Spin Hall Effect	41
3.1 Introduction to the Quantum Spin Hall effect	42
3.2 Experimental observation of the Quantum Spin Hall insulator	45
3.3 QSH edge states in magnetic field	56
3.4 Temperature dependence of the QSH effect	70
3.5 Summary	77

4 Spin Hall Effects in doped HgTe QWs	81
4.1 Theory of Spin Hall Effects	83
4.2 Experimental investigation of the Spin Hall Effect	88
4.3 Interplay of SHE and QSHE	101
4.4 Summary	111
5 Transport in ring structures	115
5.1 General description of phase effects	117
5.2 Phase effects in semiconductor ring structures	120
5.3 Observation of the Aharonov-Casher effect	125
5.4 Measurements in high magnetic field	136
5.5 Summary	141
Summary and Outlook	145
Zusammenfassung und Ausblick	149

List of Publications

Parts of this thesis were already published in

- M. König, A. Tschetschetkin, E. M. Hankiewicz, J. Sinova, V. Hock, V. Daumer, M. Schäfer, C. R. Becker, H. Buhmann, and L. W. Molenkamp
Direct Observation of the Aharonov-Casher Phase
Phys. Rev. Lett. **96**, 076804 (2006).
- M. König, H. Buhmann, C. R. Becker, and L. W. Molenkamp
Phase effects in HgTe quantum structures
phys. stat. sol. (c) **4**, 3374 (2007).
- M. König, S. Wiedmann, C. Brüne, A. Roth, H. Buhmann, L. W. Molenkamp, X L. Qi, and S. C. Zhang
Quantum Spin Hall Insulator State in HgTe Quantum Wells
Science **318**, 766 (2007).
- M. König, H. Buhmann, L. W. Molenkamp, T. Hughes, C. X. Liu, X. L. Qi, and S. C. Zhang
The Quantum Spin Hall Effect: Theory and Experiment
J. Phys. Soc. Jpn. **77**, 031007 (2008).

Further publications

- Y S. Gui, C. R. Becker, J. Liu, M. König, V. Daumer, M. N. Kiselev, H. Buhmann, and L. W. Molenkamp
Current heating of a magnetic 2DEG in $Hg_{1-x}Mn_xTe/Hg_{0.3}Cd_{0.7}Te$ quantum wells
Phys. Rev. B **70**, 195328 (2004).
- R. Scheibner, E. G. Novik, T. Borzenko, M. König, D. Reuter, A. Wieck, H. Buhmann, and L. W. Molenkamp
Sequential and co-tunneling behavior in the temperature-dependent thermopower of few-electron quantum dots
Phys. Rev. B **75**, 041301(R), (2007).

Submitted for publication

- R. Scheibner, M. König, D. Reuter, A. Wieck, H. Buhmann, and L. W. Molenkamp
Quantum dot as thermal rectifier
available on-line at arXiv:cond-mat/0703514.

Further parts of this thesis are considered for publication.

Introduction

In recent years, spin-related phenomena have moved into the focus of solid state research. The primary reason is that the spin properties became experimentally accessible in electronic devices due to the ongoing progress in nanofabrication techniques. Manifold issues can now be addressed in solid state systems for the first time and studies are pursued for fundamental scientific purposes. Furthermore, an entire new area of applications opened up and the field of spintronics (= *spin + electronics*) developed [1,2]. Spintronic devices take advantage of the electron spin, whereas conventional ones rely solely on the charge. The main improvements compared to conventional devices include the reduced or maybe even vanishing dissipation in the system and decreased electrical power consumption. For the realization of spintronic devices, the major aspects are the creation, transportation, manipulation and detection of the electronic spin polarization.

It turned out that these tasks are more difficult to realize than expected. This is particularly the case, if spintronic applications are supposed to be implemented on semiconductor materials. For example, the injection of spin-polarization from a ferromagnetic metal is highly inefficient due to the difference in the density of states for the two components [3]. The search for ferromagnetic semiconductors, e.g., GaMnAs [4], or efficient spin injection, e.g., by tunnel contacts [5], guided most research projects.

A rather new idea is to use the intrinsic spin-orbit interaction for creation, manipulation and detection of spin accumulation or spin currents. Two-dimensional electron gases formed in semiconductor heterostructures are highly suitable systems.

The advantage of this approach is that the strength of the spin-orbit interaction can be locally controlled by the Rashba effect [6]. This rather direct method to affect the electron spin not only initiated considerable experimental effort, but also was very attractive to theoreticians and triggered the prediction of various effects and devices [7–10]. A prominent example is the Spin Hall effect [11–13]. When a charge current is driven in a system with a strong spin-orbit interaction, a transverse spin current is generated and results in a spin imbalance at the sample edges. This effect may be utilized for the creation of pure spin current and spin polarization. Furthermore, the spin-orbit interaction can affect the phase of the electron wave function in form of additional phase factors, the Berry phase [14] and the Aharonov-Casher phase [15]. This modulation of the electron phase led to the concept of a new type of spin-interference device [16]. The proposed ring structure represents a kind of spin-interference field effect transistor, in which the transmission can be controlled by spin-orbit induced phases. A spin field effect transistor had been suggested by Datta and Das [17], but ferromagnetic contacts are required in the latter device, which has proven to be an obstacle for the realization.

Recently, a new state of matter in a topological sense, the Quantum Spin Hall effect, has been proposed [18,19]. This novel state is characterized by non-dissipative transport of spin-polarized electrons in one-dimensional edge channels and thus has equivalently high potential for spintronic applications.

Quantum well structures based on HgTe appear to be very suitable for the investigation of fundamental spin-orbit effects. HgTe as a bulk material is a zero-gap semimetal, whereas a narrow energy gap opens up in a quantum well. First of all, two-dimensional electron gases in HgTe quantum wells exhibit high carrier mobilities. These result in a large mean free path comparable to the characteristic sample dimensions, which is a prerequisite for the manifestation of spin-related transport phenomena. In addition, the Rashba energy can reach values of up to 30 meV, which is several times larger than for any other semiconductor material, and can be tuned over a wide range [20–22]. Both attributes help to identify effects due to the

spin-orbit interaction like the spin Hall effect or phase effects. Finally, HgTe quantum wells feature very peculiar band structure properties. Depending on the actual well width, the band structure is either normal or inverted, i.e., the ordering of the energy states in the quantum well is reversed compared common semiconductors for the latter case. For samples with an inverted band structure, the existence of the quantum spin Hall effect was explicitly predicted [23].

Within the scope of this thesis, the transport properties of HgTe-based quantum well structures are studied with an emphasis on various spin-orbit effects. A general introduction to the specific properties of this material is provided in Chapter 1. Due to recent advances in the growth and fabrication, which are also described, high mobility devices with characteristic dimensions of only a few 100 nm were available, meeting the requirements for the observation of spin-related effects.

In Chapter 2, transport phenomena are discussed, which arise from the narrow energy gap and the peculiar band structure, respectively. The Fermi energy can be tuned from the conduction band to the valence band due to the small band gap in HgTe quantum wells, resulting in a transition from the intrinsic n -conductance to p -conductance. When the Fermi level of a sample with an inverted band structure is in the energy gap, a unique Landau level dispersion gives rise to a re-entrant quantum Hall state in magnetic field.

The latter property is a manifestation of the non-trivial insulator, which forms the basis of the Quantum Spin Hall state. Due to the energy gap of some 10 meV, the demonstration of the QSH effect seems feasible in HgTe, while it turned out to be not accessible for the initially suggested materials, i.e., graphene and strained GaAs, using currently available measurement techniques. The aim of the experiments presented in Chapter 3 is the verification of this yet unobserved state of matter and an analysis of its charge transport properties.

Unlike the QSHE, the Spin Hall effect has been demonstrated for various materials. On the one hand, the spin accumulation at the sample edges was shown for

semiconductors by means of optical methods [24–26]. On the other hand, a charge imbalance induced by a spin current, called the inverse spin Hall effect, was reported for metals [27–29]. However, an electrical detection of the SHE in semiconductors is still outstanding. Hankiewicz *et al.* proposed an H-shaped device based on a semiconductor with strong spin-orbit interaction [30], where the spin Hall effect results in a voltage signal and, consequently, can be detected in a purely electrical measurement. HgTe micro-structures according to the suggested layout are investigated in Chapter 4.

Furthermore, the spin-orbit interaction due to the Rashba effect can also be used to control charge transport in suitable devices. Our HgTe ring structures resemble the one proposed by Nitta *et al.* [16], where the transmission is governed by spin-orbit induced phases. While several groups have claimed an observation of the spin-orbit Berry phase [31–33], there is no evidence of the Aharonov-Casher for semiconductor materials so far. Thus, the experiments presented in Chapter 5 focus on a fundamental demonstration of the phase effects. Promising results were already obtained in previous work in this field [34].

Chapter 1

HgTe based quantum wells

Conventional semiconductor materials have been studied extensively in the past. On the one hand, two-dimensional electron gases (2DEGs) have been fabricated for III-V semiconductor compounds. For example, 2DEGs based on GaAs have highest mobilities and are consequently used for the investigation of quantum effects in the charge transport. On the other hand, II-VI wide gap materials like CdTe or ZnSe can be doped magnetically using Mn atoms. Unlike for III-V materials, this does not yield an additional charge doping. Thus, the magnetic properties can be modified without an influence on the electric properties. These materials have mainly been studied by means of optical methods, because there are major difficulties in the doping and the application of electrical contacts.

A particular group of semiconductor compounds are the narrow-gap materials. In such systems, the energy states can mix due to their low separation. Despite the resulting peculiar transport phenomena, there has been only a low interest in the narrow-gap material HgTe. This can be attributed to the rather low mobilities and difficulties in the processing of HgTe-based devices. Indeed, the optical properties of HgTe-based superlattices [35] and quantum well structures [36] have been investigated to some extent. But there are hardly any reports [37–39] on transport measurements in this material except for results obtained by the Würzburg group.

HgTe as a bulk material is a zero-gap semimetal. This leads to an inversion of the sequence of the subbands, when HgTe is used for the well layer in quantum well structures. In fact, the exact ordering of the states is determined by the confinement energy. A normal band structure is obtained for narrow quantum wells, while the band structure is inverted for wide quantum wells. Due to the inverted band structure, the electrons in the conduction band feature hole-like properties.

This hole-like character of the electrons in the conduction band gives rise to a large spin-orbit interaction of the Rashba type. For HgTe quantum wells, the Rashba splitting is much more pronounced than in any other semiconductor material.

Recently, a significant progress has been achieved in the growth of HgTe-based quantum well structures. These advances make samples with large mobilities available. Additionally, lithographical techniques were developed which meet the special requirements of HgTe quantum wells.

1.1 Band structure of HgTe-based quantum wells

In semiconductor materials, two-dimensional electron gases can be created by the fabrication of quantum well (QW) structures. In general, three types of quantum well structures formed in heterostructures can be distinguished. Here, the energy gaps of the used materials and the respective valence band offset (VBO) play the decisive role. In Fig. 1.1, the band edge profiles of the different types are shown. In a type-I QW [Fig. 1.1 (a)], both electrons and holes are located in the same layer, the QW layer between the barriers. In a type-II quantum well, the choice of the material for barrier and well layer determines where the electrons and holes are located, respectively. For a system as shown in Fig. 1.1 (b), the electrons are trapped in the QW layer, whereas the holes are free to move within the outer layers. When QW and barrier material are interchanged, the situation is reversed, i.e., the holes will be bound in the QW layer. A type-III quantum well is formed, when a semimetal is combined with a semiconductor [Fig. 1.1 (c)]. This kind of quantum well formation is unique to mercury-based compounds [35], because only for these symmetry-induced semimetals a negative energy gap $E_g = E_{\Gamma_6} - E_{\Gamma_8}$ can be obtained. As a barrier material, a semiconductor with a positive energy gap is used.

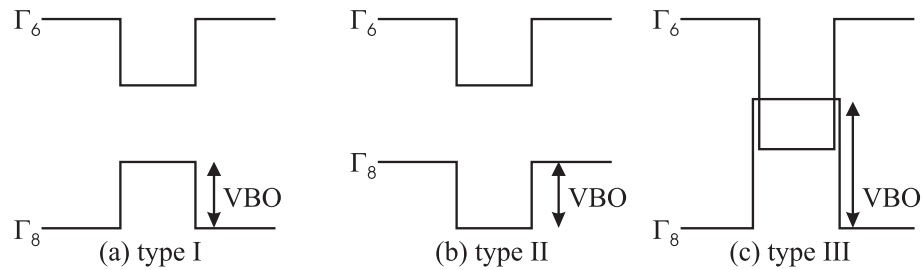


Figure 1.1: The three QW types are sketched schematically.

In this thesis, type-III HgTe quantum wells with barriers of $\text{Hg}_{0.3}\text{Cd}_{0.7}\text{Te}$ have been investigated. While HgTe as a bulk material has an energy gap of -300 meV, for QW structures the energy gap depends heavily on the QW width d_{QW} due to the quantum confinement. The evolution of the electronic subbands as a function of

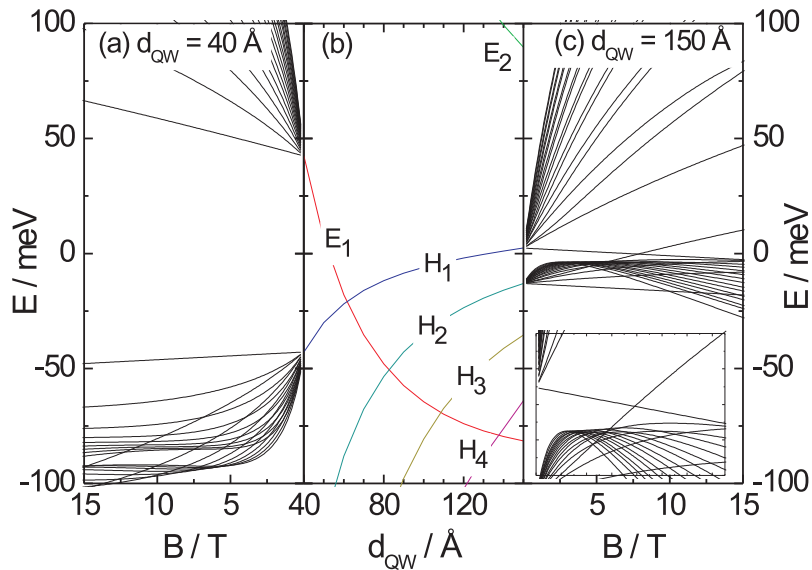


Figure 1.2: (a) and (c) show the Landau level dispersion for a 40 Å and a 150 Å QW, respectively. For clarity, only Landau levels from the lowest subbands of the conduction and the valence band are included. The inset in (c) shows a magnification of the crossing region. (b) Due to the quantum confinement, the position of the energy subbands depends heavily on the QW width. (The light-hole subbands are remote, so that they are not depicted.)

the QW width is shown in Fig. 1.2 (b). The notation of the subbands as electron (E)-, light-hole (L)- and heavy-hole (H)-like corresponds to the properties of the respective wave functions [40]. As can be seen, the H_1 -band and the E_1 -band cross for a critical QW width $d_{\text{crit}} \approx 63 \text{ \AA}$ [40]. For more narrow QWs the energy gap between the lowest subbands of the Γ_6 band and the Γ_8 band is positive. This order of the bands is referred to as a normal band structure, since it is common for most semiconductor materials. For increasing QW width, the confinement energy is reduced. Consequently, the lowest subband with Γ_8 symmetry lies above the lowest one with Γ_6 symmetry for $d_{\text{QW}} > d_{\text{crit}}$ and the energy gap is negative according

to the above definition. Thus, this kind of band structure is called inverted. For the band structure, self-consistent Hartree calculations have been performed using a 8×8 $\mathbf{k}\cdot\mathbf{p}$ model [41].

The small energy separation of the subbands causes to a mixing of the electron-like and hole-like states. This is reflected in the non-vanishing Bloch components of both the Γ_6 and the Γ_8 state for a single subband, especially for the E_1 - and H_1 -band which are closest to each other. The actual ratio of the Bloch components for the individual bands, indicating the degree of mixing of the states, depends on the QW width. For a normal band structure, the E_1 band is the lowest subband of the conduction band and the electrons have an electron-like character, i.e., the Γ_6 Bloch component is the dominant one. For an inverted band structure, the electrons from the H_1 subband, being the lowest state in the conduction band, are hole-like. This peculiar property, however, is not reflected in the band dispersion of the electronic states [Fig. 1.3 (a)]. While the conduction subbands, i.e., E_2 and H_1 , have an electron-like dispersion, the valence subbands are hole-like. The hole-like character of the electrons in the H_1 subband manifests itself in the response of the wave function to an asymmetric QW potential. Fig. 1.3 (b) shows the edge profiles of the Γ_6 and the Γ_8 band for an asymmetric quantum well with $d_{QW} = 120$ Å. The electron density distribution is shifted towards the maximum of the confining potential. This is contrary to the behavior expected for electrons, but can be explained by the hole-like character.

A unique dispersion of the Landau levels is obtained for QW structures with $d_{QW} > d_{crit}$. In this regime of an inverted band structure, the lowest Landau level (LL) originating from the H_1 -band contains a pure heavy hole state ($M = -3/2$). Consequently, this LL lowers its energy for increasing magnetic field. On the other hand, one of the valence band LLs has a more electronic character and shifts to higher energies in magnetic field. This leads to a crossing of these two peculiar LLs for a finite magnetic field. Its exact B -field value B_{cross} depends on the QW width. In Fig. 1.2 (c), the LL dispersion of the lowest subbands from the valence and the

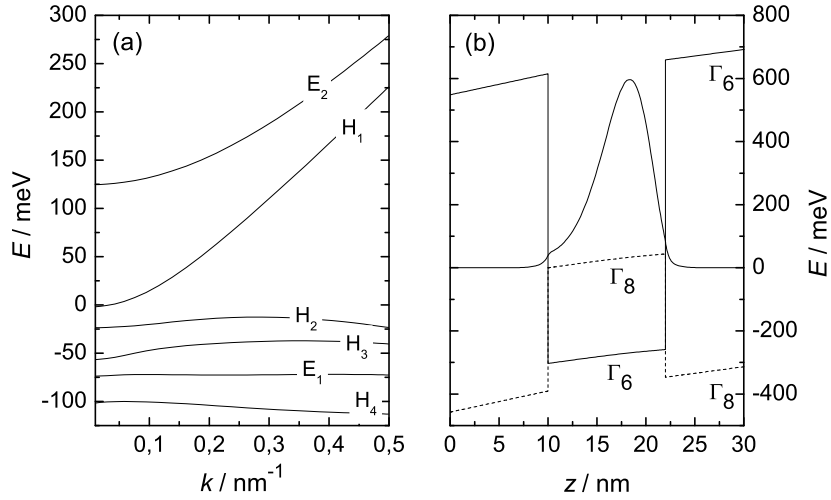


Figure 1.3: (a) The $E(k)$ -dispersion for $k \parallel (1, 0)$ is shown for a quantum well with $d_{QW} = 120 \text{ \AA}$. (b) Band edge profiles and electron density distribution for the H_1 subband are plotted for an asymmetric 120 \AA QW.

conduction band is shown for a QW width of 150 \AA . For this width, the LL crossing occurs at $B_{\text{cross}} \approx 8 \text{ T}$. For a normal band structure ($d_{QW} = 40 \text{ \AA}$), the energy gap between the lowest Landau levels in the conduction and valence band, respectively, opens up in magnetic field [Fig. 1.2 (a)].

The crossing of Landau levels for an inverted band structure was demonstrated experimentally by Schultz *et al.* [42]. They investigated a HgTe/CdTe QW structure with a well width of 122 \AA by means of far-infrared Fourier-transform spectroscopy. From the observation of several optical transitions as a function of Fermi energy and magnetic field, they concluded that the LL crossing occurs at $B \approx 12 \text{ T}$, which is in good agreement with the band structure calculations.

Experiments examining the LL crossing by magneto-transport measurements will be presented in section 2.2 for several structures with different QW widths d_{QW} . The unique LL dispersion is expected to be reflected in a re-entrant quantum Hall

state for finite magnetic field, when the Fermi energy is located within the fundamental gap for $B = 0$. This unusual behavior can be observed for samples with an inverted band structure.

1.2 Rashba spin-orbit interaction

For structures with an inversion asymmetry, the degeneracy of the electronic states can be lifted even in the absence of a magnetic field. The first possibility is an asymmetry of the underlying crystal structure. This bulk-inversion asymmetry (BIA) is present, e.g., in a zinc-blende structure, which is common for III-V and II-VI semiconductors. The BIA-induced splitting is described by the Dresselhaus term [43].

It was shown that this contribution to the spin splitting can be neglected for narrow-gap materials [44–46]. In such systems, the dominant mechanism is attributed to the structure inversion asymmetry (SIA) [6]. In this case, an asymmetry of the confining potential of the quantum well lifts the spin degeneracy. The structure inversion asymmetry can be caused by a built-in potential or by an external electric field.

The first experimental observation of a spin splitting due to the lack of inversion symmetry was achieved in GaAs/AlGaAs 2DEGs by Störmer *et al.* [47] and Stein *et al.* [48] in 1983. One year later, Bychkov and Rashba developed a theoretical model to describe the SIA-related spin-splitting [6].

The Hamiltonian of a two-dimensional system with spin-orbit interaction is given by

$$\hat{\mathbf{H}} = \hat{\mathbf{H}}_0 + \hat{\mathbf{H}}_{SO} = \frac{\hbar^2 k^2}{2m^*} + \alpha[\vec{\sigma} \times \vec{k}]\vec{\nu}, \quad (1.1)$$

where $\hat{\mathbf{H}}_{SO}$ is the so-called Rashba term [6]. In the above equation, m^* is the effective electron mass, \vec{k} the electron wave vector with $k = |\vec{k}|$, α the spin-orbit constant, $\vec{\sigma}$ are the Pauli spin matrices and $\vec{\nu}$ is a unit vector perpendicular to the plane of electron motion.

In some references [49, 50], the expectation value $\langle \alpha^* E_z \rangle$ is used instead of α . From this notation, it is obvious that the Rashba splitting depends on material-specific properties described by α^* [51] and on the effective electric field E_z . The origin of the Rashba splitting was discussed controversially [44, 49, 52–55]. A recent overview of the arguments is provided by Zhang *et al.* [20]. Experimental evidence was provided that the band-edge profile and penetration of the electron wave function into the barriers play an important role [56]. Recent theoretical investigations showed that the Rashba spin-splitting is controlled by the expectation value of the electric field, properties of the interfaces and spin-dependent boundary conditions [57].

Winkler and Rössler showed that the Rashba SO interaction leads to a spin splitting linear in k [49]:

$$E_{\pm} = E_0 \pm E_{SO} = \frac{\hbar^2 k_{\parallel}^2}{2m^*} \pm \alpha k_{\parallel}, \quad (1.2)$$

where k_{\parallel} is the in-plane component of the electron wave vector. This linear dependence of the Rashba splitting on the wave vector k is valid for electrons. According to Winkler [50], the Rashba splitting for heavy-hole systems is given by

$$E_{SO} = \pm \beta k_{\parallel}^3, \quad (1.3)$$

and the Rashba splitting energy for a given value of k_{\parallel} is

$$\Delta_R = E_+ - E_- = 2E_{SO} = 2\beta k_{\parallel}^3 \quad (1.4)$$

As can be seen from Eqs. (1.2) and (1.3) the Rashba splitting vanishes for $k = 0$. Thus, there is no difference in energy between the two spin-split states, but rather there are two different values for k at the Fermi energy E_F . Due to the different dispersion of the two branches, a difference in the population the spin-split subbands is obtained. The carrier densities n_{\pm} for the two subbands in a heavy-hole system with a total density n_S are given by

$$n_{\pm} = \frac{1}{2}n_S \pm \frac{\sqrt{2}m^*\beta n_S}{\hbar^2 X} \sqrt{\pi n_S(6 - 4/X)} \quad (1.5)$$

with

$$X = 1 + \sqrt{1 - 4\pi n_S \left(\frac{2m^*\beta}{\hbar^2} \right)^2} \quad (1.6)$$

It has to be noted that the electrons in the two branches of each subband cannot be identified as spin-up and spin-down, because their eigenstates are not linearly polarized and the net magnetic moment vanishes for $B \rightarrow 0$ ¹.

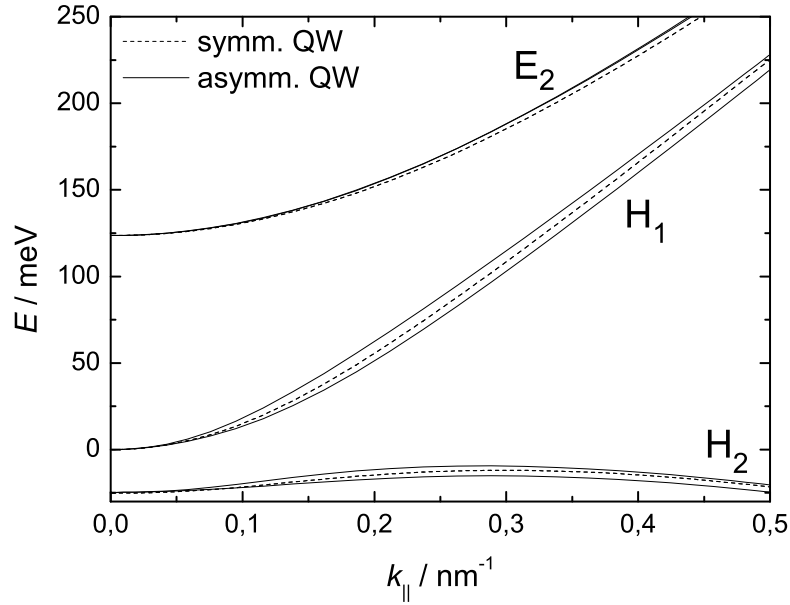


Figure 1.4: The band dispersion was calculated for a QW with a width of 120 Å. For a symmetric QW (dashed lines), the subbands are degenerate. In a asymmetric QW (solid lines), the splitting of the H-bands is much larger than for the E₂-subband.

Fig. 1.4 shows the spin-split subbands for a HgTe QW structure with a QW width of 120 Å. For a symmetric quantum well, all subbands are degenerate. An asymmetry of QW potential lifts the spin degeneracy for all subbands. As implied by Eqs. 1.2

¹ To emphasize this, the term "chiral splitting" is sometimes used instead of "spin splitting" in literature [58].

and 1.3, the size of the splitting depends on the character of the subbands. While the heavy-hole-like bands H_1 and H_2 are strongly split, the splitting for the electron-like subband E_2 is much smaller. For small k , the splitting of the H-subbands is proportional to k^3 , whereas the splitting of the E_2 -band is linear in k . This is in good agreement with the above theoretical models. However, the splitting saturates and even decreases for larger k (Fig. 1.5). This non-monotonous behavior can be attributed to the non-parabolicity of the subbands [49] and an increase of the effective energy gap for large k [57].

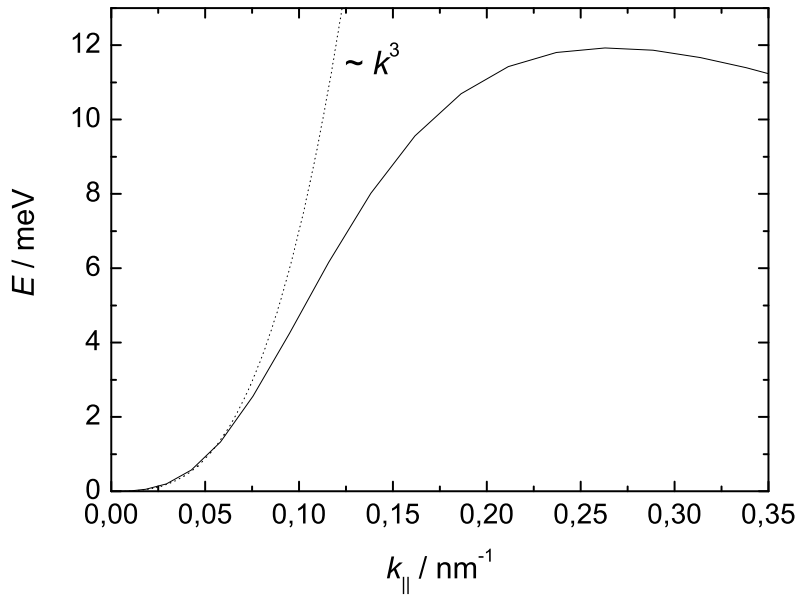


Figure 1.5: The splitting of the H_1 -subband (cf. Fig. 1.4) can be approximated by a k^3 -dependence for small k -values.

For HgTe-based QW structures with an inverted band structure, the Rashba SO interaction is enhanced due to the heavy-hole-like character of the electrons in the lowest conduction subband. For suitable devices, a Rashba splitting of up to 30 meV has been observed [20–22]. This is several times larger than the splitting in III-V narrow-gap semiconductors, where values of the Rashba splitting energy up

to approximately 10 meV have been reported [56, 59–61]. Additionally, the Rashba splitting in HgTe QWs can be tuned over a wide range. When a sample is doped symmetrically, the Rashba splitting vanishes. The application of an external voltage to a gate electrode induces an asymmetry of the potential around the QW layer, and the electrons experience an electric field which gives rise to a Rashba splitting. For intrinsically symmetric quantum wells, the Rashba splitting vanishes for $V_g \approx 0$ but can be tuned to finite values of up to 15 meV by an external gate voltage [20]. In contrast, an asymmetric doping causes a finite Rashba splitting even for $V_g = 0$. The asymmetry is increased by applying a suitable voltage, yielding a splitting up to the largest value mentioned above [22].

1.3 Sample fabrication

The results presented in the scope of this thesis were obtained from HgTe-based QW structures. To utilize the particular properties of a normal and an inverted band structure, respectively, samples with a QW width d_{QW} in the range from 45 Å to 120 Å were investigated. The structures have been grown by molecular beam epitaxy (MBE)². Fig. 1.6 shows a schematic sketch of the layer sequence. The $\text{Hg}_{0.3}\text{Cd}_{0.7}\text{Te}$ barriers are *n*-type modulation-doped either on one or both sides of the QW with Iodine. This doping leads to an asymmetric or symmetric potential for the quantum well, respectively. The relevant properties of the investigated samples, e.g., QW width and symmetry of doping, will be given in each section.

Recently, advances in the growth of HgTe-based QW structures were achieved [63]. Several modifications, e.g., an increase of the width of the spacer between the quantum well and the doping layer, resulted in an enhancement of the carrier mobility μ . Thus, samples with mobilities of several $10^5 \text{ cm}^2/(\text{Vs})$ even for low densities $n < 5 \cdot 10^{11} \text{ cm}^{-2}$ were available for our measurements. For such sample properties,

² Details of the MBE growth of HgTe-based semiconductor compounds can be found in Refs. 62 and 20.

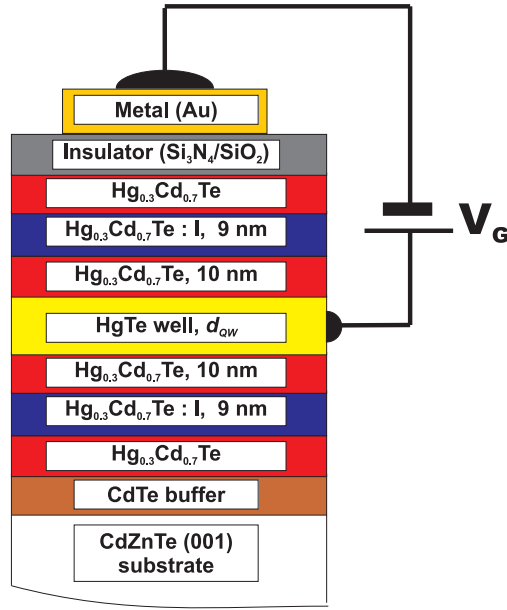


Figure 1.6: The width d_{QW} of the HgTe quantum well (here doped symmetrically) ranges from 45 Å to 120 Å.

the mean free path exceeds the typical sample dimensions. This allows for the investigation of quantum effects which otherwise would be destroyed by scattering.

From the MBE grown quantum wells, devices were fabricated by means of optical and electron beam (e-beam) lithography. For the optical lithography, standard recipes for semiconductor processing can be applied. For nanostructured devices fabricated by e-beam lithography, however, the customary processes for other semiconductor materials imply bake-out temperatures up to 200°C for the polymethylmethacrylate (PMMA). Due to the low growth temperature of 180°C for the HgTe layer, the use of elevated temperatures would cause an interdiffusion of well and barrier materials. Consequently, all lithographical processes are to be restricted to temperatures well below the growth temperature.

A special process was developed for the first nanostructures based on HgTe QWs, in which a standard photoresist was used for the e-beam lithography as well [64]. While this method enabled the fabrication of devices on a sub-micron scale, it turned

out that the resist is oversensitive to the electron beam and back-scattered electrons. The overexposure of the resist resulted in an enlargement of the pattern transferred to the sample. Recently, a process has been developed, in which PMMA can be used with a bake-out temperature of only 80°C. Using this resist for e-beam lithography yields a better agreement between the design transferred to the sample by the electron beam and the resulting device.

After the pattern has been transferred to the sample, a Ti layer is evaporated. After the lift-off, the remaining Ti pattern serves as a mask for the successive etching. The first nanostructures were fabricated by wet chemical etching. Due to the homogeneous etching, this method leads to an undercutting, i.e., the structure is etched from the sides as well. The undercutting can be reduced, if dry plasma etching is used instead. Furthermore, samples fabricated by dry etching show a higher mobility than devices made by wet chemical etching [63]. This new etching process was available for most of the samples discussed below³. After the etching, the Ti mask is removed by dipping the sample into hydrofluoric acid.

When the mesa is structured, a super-lattice of Si₃N₄ and SiO₂ with a total thickness of 110 nm is deposited by plasma-enhanced chemical vapour deposition (PECVD). This layer serves as an insulator between the semiconductor and the metal (Au) layer⁴ on top of the structure, which is used as a top-gate. By applying a voltage to the gate, the carrier density n , the mobility μ and the Rashba splitting Δ_R can be modified [20, 63].

It is necessary to apply large voltages for a maximum effect on the carrier density and the Rashba splitting. However, it was shown that the influence of the gate voltage is limited [22]. When a positive gate voltage is applied, the carrier density of the 2DEG increases. For a sufficiently large voltage, the conduction band edge

³ The plasma source was put into operation during the work on this thesis.

⁴ Between the insulator and the Au layer, a Ti layer of a few 10 nm serves as an adhesion promoter.

of the top semiconductor layer is at the same level as the chemical potential of the 2DEG. Then, electrons from the can tunnel from the QW layer to the insulator-semiconductor interface and occupy surface states at lower energies. The interface can now be seen as a capacitor plate parallel to the top gate and the 2DEG, respectively. Any further increase of the gate voltage will only increase the voltage drop over the insulator, while the semiconductor remains unaffected, yielding a maximum for the density in the 2DEG. When the gate voltage is lowered again subsequently, the density decreases immediately. The surface states remain charged until they are lifted above the chemical potential. Finally, tunneling of electrons from the surface states to the 2DEG leads to a saturation of the carrier density in the 2DEG for sufficiently large negative voltages. The charging and discharging of the surface states does not only limit the variation of the carrier density, but also results in a hysteresis of the gate-voltage dependence of the carrier density in the 2DEG. It can be inferred from this model that the hysteresis loop is reproducible as long as the gate voltage range is not changed, i.e., the gate-dependent density is reproduced for a repeated variation of the gate voltage between two extremal values. Furthermore, it was stated that a hysteresis-free behaviour is possible as long as the surface states have not been populated, which is the case for moderate gate voltages.

Consequently, a dependence of n , μ and Δ_R on the gate voltage can be established in a controlled way. When only small changes of the sample properties are required, the device can be operated in the hysteresis-free range. For large gate voltages, the variation of density and Rashba splitting is limited due to the influence of the surface states. However, the behavior is reproducible for a cycle in gate voltage.

1.4 Summary

For this thesis, HgTe-based type-III QW structures were investigated. The negative band gap of bulk HgTe gives rise to an inverted band structure for wide quantum wells, i.e., $d_{QW} > 63 \text{ \AA}$. For narrow QW layers, the energy states are shifted due to the confinement in such way that a normal band structure emerges. For all QW

widths discussed here, the separation of the subbands in energy is small enough to enable a mixing of the states. This is reflected in a hole-like character of the electrons in the conduction band for samples with an inverted band structure. One consequence of this enhanced mixing of the states is a unique LL dispersion. Landau levels from the valence and the conduction band cross for a finite magnetic field. Furthermore, the hole-like character yields a Rashba splitting of the conduction band, which is several times larger than for any other semiconductor material.

The quality of the QW structures has recently been improved by advances in the MBE growth, so that high mobilities were achieved even at low electron densities. A refinement of the lithographical process allows for the fabrication of devices with dimensions down to the order of 100 nm. Due to the progress in both fields, devices were available to study the peculiar properties of HgTe-based quantum well structures. The small sizes additionally make quantum effects experimentally accessible.

Chapter 2

Investigation of the band structure

HgTe as a bulk material is a zero-gap semimetal. A narrow energy gap appears when it is used as a QW layer. Then, the band structure is inverted for wide quantum well layers. For a decreasing QW width, the confinement energy increases, so that the inversion of the energy states is lifted for quantum wells with a width below a critical value $d_{\text{crit}} \approx 63 \text{ \AA}$. For both band structure regimes, the states mix due to their low separation in energy.

QW structures with a well width between 45 \AA and 120 \AA were investigated for this thesis. In this range, the band gap does not exceed 80 meV . While the gap is larger for $d_{\text{QW}} < 45 \text{ \AA}$, it is limited due to the confinement of the energy subbands otherwise. Because of the narrow band gap, it is possible to shift the Fermi energy from the conduction band to the valence band. This is reflected in a transition from n - to p -conductance. The mixing of the states for an inverted band structure causes a unique LL dispersion. Two Landau levels originating from the conduction band and the valence band, respectively, cross for a finite magnetic field. This crossing occurs within the energy gap, giving rise to a re-entrant quantum Hall state. The transition from an insulator to a conducting state in a magnetic field due to the peculiar LL dispersion has not been reported so far as well. This chapter provides experimental studies of these two transport phenomena based on the peculiar band structure of HgTe quantum well structures.

2.1 Transition from n- to p-conductance

For a variety of investigations on semiconductor structures, the application of a voltage to a gate electrode on top of the device has been utilized to achieve a change of the carrier density. This results in a shift of the Fermi with respect to the energy bands¹. For instance, the Fermi level is lowered, when the carrier density is decreased and, consequently, less states are occupied. Generally a linear relation is observed for the dependence of the electron density n on the gate voltage V_g :

$$n(V_g) = \alpha \cdot (V_g - V_{th}), \quad (2.1)$$

where $\alpha = \frac{\partial n}{\partial V_g}$ is the gate voltage induced change of the carrier density and V_{th} the threshold voltage. As can easily be seen from Eq. 2.1, the 2DEG is entirely depleted for $V_g = V_{th}$.

The linear dependence of the density on the gate voltage according to Eq. 2.1 has also been observed for HgTe-based 2DEGs [20, 22]. In these studies, the application of the gate voltage yielded a change of both the carrier density and the Rashba splitting. Even though it was possible to vary the density over a wide range, a total depletion of the 2DEG was not achieved for the used gate voltages. This can be attributed to the rather high intrinsic densities, i.e., for $V_g = 0$, $n \approx 1 \cdot 10^{12} \text{ cm}^{-2}$ in the investigated samples. In addition, Al_2O_3 was used as an insulator between the semiconductor and the gate electrode for these devices. For this insulator, the risk of an electrical breakthrough restricted the gate voltage to rather low values, providing another limitation for the variation of the carrier density.

For the work presented in this chapter, Hall bars with a length L and a width W of $600 \text{ }\mu\text{m}$ and $200 \text{ }\mu\text{m}$, respectively, were fabricated from structures with intrinsic densities $n \leq 5 \cdot 10^{11} \text{ cm}^{-2}$. When a negative gate voltage is applied, the electron density is decreased. The depletion of the 2DEG is reflected in an increase of the Hall

¹ Strictly speaking, the Fermi energy stays constant and the energy subbands are shifted with respect to the Fermi energy. Nevertheless, the more descriptive picture of shifting the Fermi energy will be used throughout the thesis.

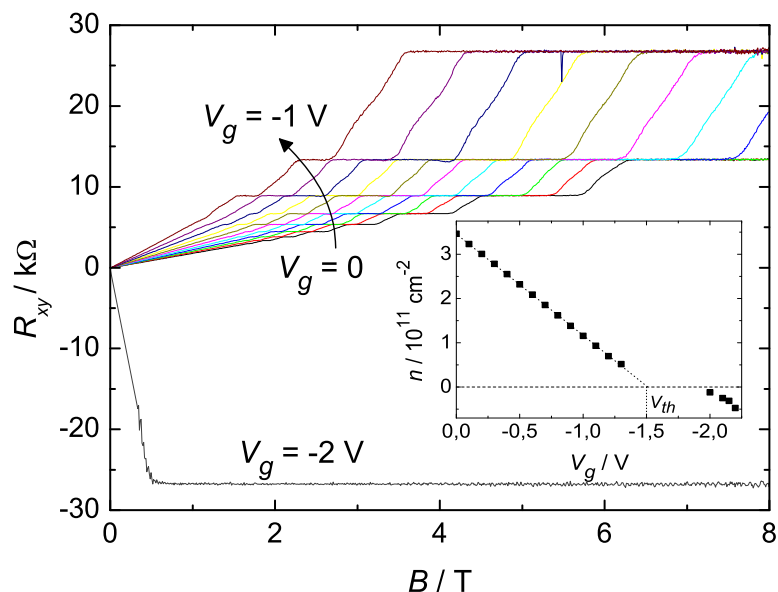


Figure 2.1: The Hall resistance R_{xy} was measured for various gate voltages. The inset shows the gate-voltage dependent carrier density, which was deduced from the Hall measurements.

coefficient (Fig. 2.1). Here, the linear dependence of the density on V_g (cf. Eq. 2.1) has been found for densities down to $n \approx 5 \cdot 10^{10} \text{ cm}^{-2}$ (inset of Fig. 2.1). Lower densities are not observed, although the threshold voltage has not been reached yet. In this case, the transmission through the sample is suppressed by potential fluctuations which inhibit diffusive transport and only allow for hopping transport. In this transport regime, the electron density can not be determined by Hall measurements. It is also possible that the Fermi energy is locally shifted into the energy gap due to potential fluctuations and the sample becomes insulating in that part. Finally, the Fermi energy is shifted into the fundamental gap for the entire device. Due to the large sample dimensions, potential fluctuations or local insulating regions result in the same behavior as an insulating state for the entire device. Thus, one can not distinguish between these two regimes, when only the experimental results shown in this chapter are considered.

For large negative voltages, conductance is observed again. It can be learned from the Hall resistance (Fig. 2.1) that the transport is now hole-mediated, i.e., the Fermi energy is located in the valence band. Unlike for n -conductance, only a weak change of the carrier density is observed in the p -conducting regime as a function of gate voltage. Since the transition to p -conductance requires high negative voltages, the influence of the gate voltage on the two-dimensional hole gas might be limited due to the screening effects described in Ref. 22 (cf. Sec. 1.3). In addition, the change of carrier density can also be restricted by a low density of states close to the valence band (VB) maximum. In this case, a shift of the Fermi energy within the VB does not provide the same variation of the density as for the conduction band, where the density of states is larger. In fact, the dispersion of the valence band depends strongly on the QW width. Hence, it depends on the properties of the individual sample, which reason is predominant for the limitation of the p -density.

The longitudinal resistance R_{xx} as a function of V_g reflects the transition from n - to p -conductance as well (Fig. 2.2). For a decreasing electron density the resistance rises until it reaches a maximum for the insulating regime, which is several orders of magnitude larger than for the n -doped regime². When the Fermi energy finally is shifted into the valence band and the sample consequently becomes p -conducting, R_{xx} decreases again by some orders of magnitude.

To our knowledge, a signature in transport for a transition from n - to p -conductance via an intermediate insulating regime has not been shown for other materials so far. A direct transition from n - to p -conductance is possible and has been reported for the zero-gap material graphene [65].

The transition from n - to p -type has been observed for several samples with different QW widths. For $45 \text{ \AA} \leq d_{QW} \leq 120 \text{ \AA}$, the band gap does not exceed 80 meV.

² The obtained finite resistance and the noisy signal for the insulating regime are artefacts due to difficulties in performing an exact measurement of $I = 0$. In addition, the device resistance for the insulating regime is approximately of the same order than the input resistance of the instruments.

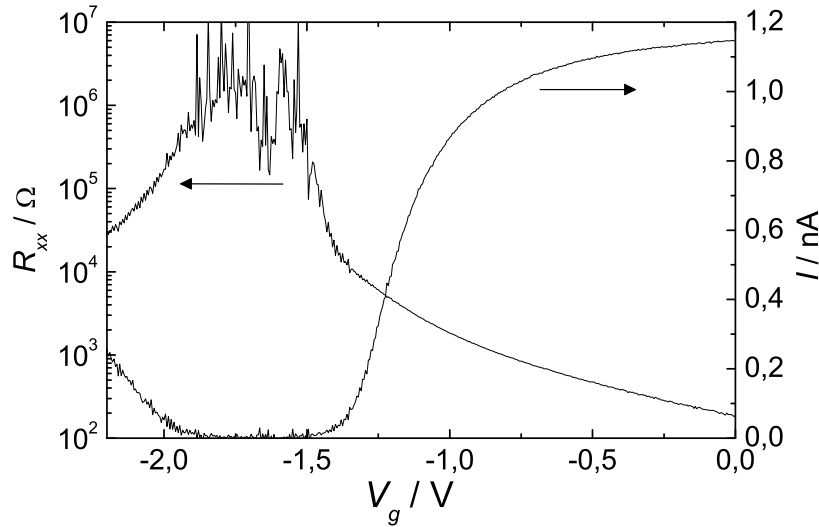


Figure 2.2: The longitudinal resistance R_{xx} and the sample current I are plotted as a function of the applied gate voltage.

Since the feasible variation of the Fermi energy is larger, it can be shifted from the conduction band to the valence band, if the intrinsic electron density is sufficiently low.

A relation between the width-dependent energy gap and the insulating range in the gate voltage could not be established. This can be explained by the rather large voltages which are usually required to reach the p -conducting regime for the intrinsically n -doped samples. As it was shown in Sec. 1.3, the influence of the gate on the 2DEG can be reduced by surface states. Due to the screening of the gate potential, deviations from the linear gate-voltage dependence of the density (cf. Eq. 2.1) can be expected. The influence of the surface states increases with the absolute value of V_g , finally giving rise to a saturation of the carrier density. For high intrinsic doping, large voltages are required for the depletion of the 2DEG and the sample will remain in the insulating state for a larger voltage range than for a device with a low intrinsic carrier density, even though the band gap is identical.

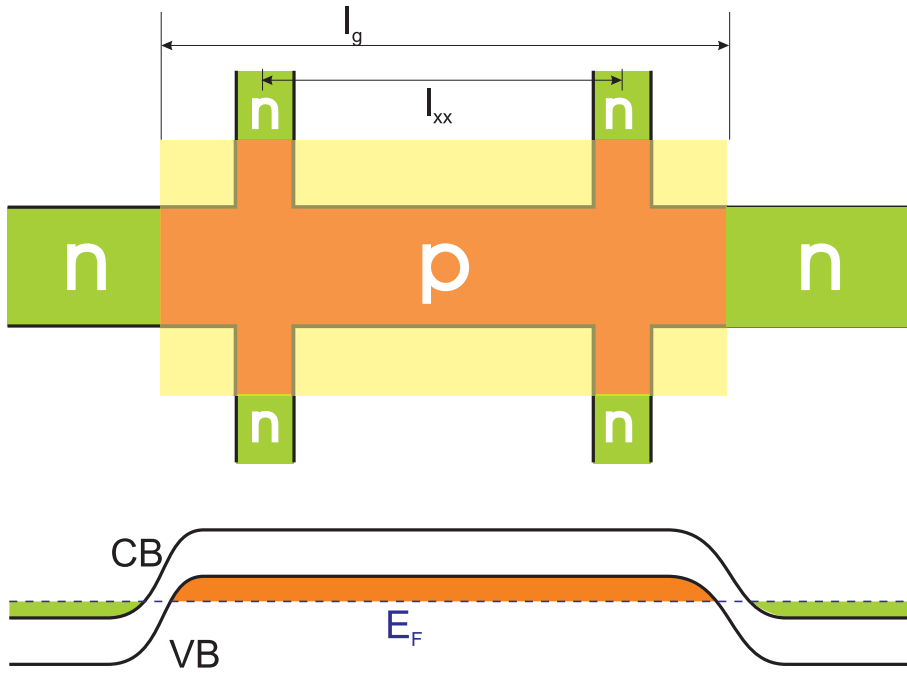


Figure 2.3: The top figure shows the carrier species in a typical Hall bar device for negative gate voltages $V_g < V_{th}$: the region under the gate electrode (yellow) becomes p -conducting (orange), whereas the leads remain n -type (green). The corresponding band edge diagram is sketched in the bottom figure: for the leads, the Fermi energy (dashed line) is in the conduction band, while it is in the valence band for the gated region.

The observed transition from n - to p -conductance raises the question, how transport is possible in the p -type regime at all. Since the samples are intrinsically n -doped and the leads are not covered by the top-gate, the 2DEG in this region remains n -type, independent of the gate voltage (Fig. 2.3). The entire device consequently consists of a p -type region connected to n -type contacts, when the gated region is tuned to p -conductance. As can easily be seen from the band edge diagram, thin insulating regions occur at the interfaces between the n -doped leads and the gated p -region. As a result, the sample contains two interfaces regarding the carrier type; for a given direction of current, one is a transition from n to p , while the other one is

of reversed order. The interfaces can be considered as diodes; one of them is always set in conducting direction and the other one is in reversed direction, independent of the bias voltage. Consequently, transport should be suppressed by the reversed diode for such a device.

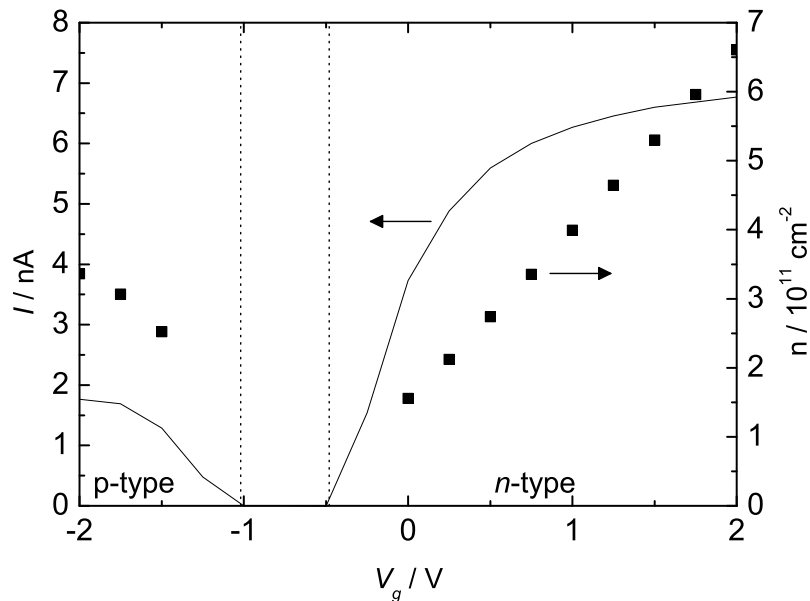


Figure 2.4: The sample current (solid line) and the carrier density (squares) are shown as a function of gate voltage. The voltage range covers the transition from *n*- to *p*-conductance via an intermediate insulating regime.

However, Esaki showed that transport through a reversed diode is possible due to tunneling [66]. For our devices, the tunneling resistance can be estimated by employing a simple model. For sake of simplicity, it is assumed that the voltage measurements are not affected by the *p* – *n* transition in each voltage probe. Thus, the four-terminal resistance $R_{4\text{term}}$ depends only on the density and mobility of the carriers in the gated region. For the two-terminal resistance $R_{2\text{term}}$, one has to distinguish between *n*- and *p*-conductance for the gate-covered region. In the *n*-

regime, the ohmic contacts to the 2DEG, the ungated leads and the gate-covered 2DEG contribute to $R_{2\text{term}}$. The total resistance of the ohmic contacts and the n -doped leads is independent of the gate voltage and can be described by a constant value R_{cont} . The resistance R_{gate} of the gated region depends on the carrier density and mobility, which are varied by V_g . It can be calculated from $R_{4\text{term}}$, when the dimensions of the top gate are known: $R_{\text{gate}} = \frac{l_g}{l_{xx}} R_{4\text{term}}$, where l_g is the gate length and l_{xx} is the distance between the voltage probes used for the four-terminal measurement (cf. Fig. 2.3). For a p -type device the tunneling resistance R_{tunnel} due to the $n-p$ interfaces has to be added to R_{cont} and R_{gate} to obtain $R_{2\text{term}}$. According to Esaki [66], the tunneling behavior depends on the density of states of the p - and the n -region. To keep the estimation of the tunneling resistance simple, R_{tunnel} is assumed to be constant. This simplification is justified, because the density of states for the n -doped side of the diode is constant anyway. As described above, usually only a small change in the carrier density is possible for the p -type region and the change in the density of states can be neglected here. From these considerations, a tunneling resistance of some few 10 k Ω is determined for various devices with different QW widths. This resistance value is sufficiently low to allow for charge transport through the reversed diode. However, R_{tunnel} is larger than the size of the contact resistance R_{cont} , which is usually below 10 k Ω , and the resistance of the two-dimensional hole gas (2DHG). Thus, the tunneling resistance due to the $n-p$ transition at the gate boundary is the main reason for the reduced transmission through the p -conducting regime. As can be seen in Fig. 2.4, the current for the p -conducting regime is significantly smaller than for the n -regime, even though the carrier densities are comparable, e.g., for a gate voltage of -2.0 V and -0.75 V, respectively.

The current in the p -conducting regime is additionally limited by an increased resistivity of the 2DHG. As can be determined from magneto-transport measurements, the hole mobility is approximately one order of magnitude smaller than the electron mobility for an identical carrier density. The difference in mobility can be explained by the effective mass, which is approximately one order of magnitude

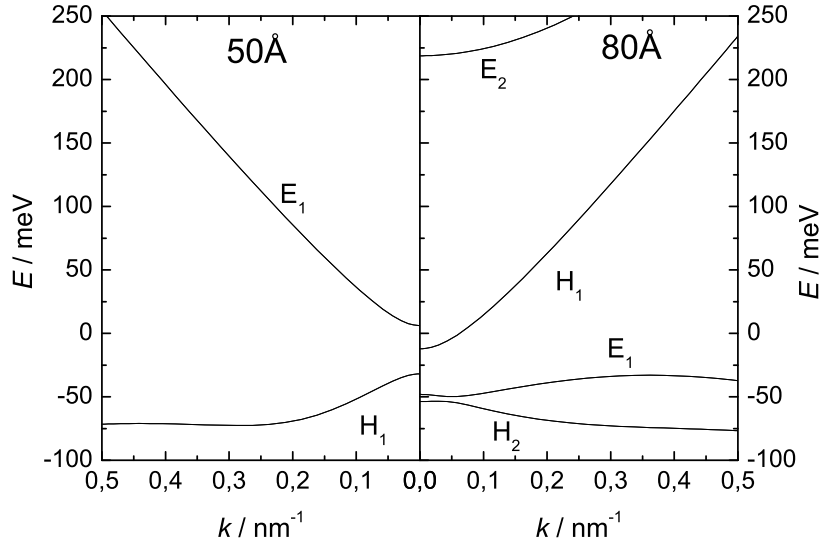


Figure 2.5: The $E(k)$ dispersion is shown for a 50 Å QW (left) and an 80 Å QW (right). Remote bands are omitted to establish a better comparability of the k -dependence of the individual subbands.

larger for the valence band than for the conduction band. In the Drude transport theory, the mobility is given by $\mu = \tau m^*/e$, where τ is the scattering time. The difference in the effective mass for conduction and valence band is reflected in the band dispersion (Fig. 2.5): The energy of the conduction band shows a significant dependence on k , yielding a small effective mass $0.02 m_e < m^* < 0.04 m_e$ [67, 68]. In contrast, the valence band is almost flat, which suggests a much higher effective mass according to $m^* = \hbar^2 \left(\frac{\partial^2 E}{\partial k^2} \right)^{-1}$. Using the band structure calculations for an 80 Å QW (cf. Fig. 2.5), an effective mass of approximately $0.2 m_e$ is obtained for the E_1 band.

It can be concluded that the small band gap of HgTe-based quantum wells makes a tuning of the sample from the intrinsic n -conductance to p -conductance possible, if sufficiently large negative gate voltages are applied. While the Fermi level crosses

the energy gap between the conduction band and the valence band, the sample is in an insulating state. When the gate-covered region is in the p -conducting regime, the sample is turned into an n - p - n structure. The finite current through the reversed diode, which is formed at one of the n - p interfaces, can be explained by tunneling. Thus, transport experiments in both the n - and the p -type regime are feasible.

2.2 Landau levels in HgTe

As it was shown in the previous section, the Fermi energy can be shifted into the energy gap by a gate voltage. For devices with an inverted band structure the energy gap will close for a finite magnetic field due to the unique Landau level dispersion (cf. Sec.1.1.1). While the underlying LL crossing has already been observed in optical measurements [42], there has been no experimental investigation of this peculiar property by means of electrical transport measurements so far.

To explore the LL dispersion, measurements in an external magnetic field have been carried out. When a 2DEG is subjected to a perpendicular magnetic field, the electrons condense on Landau levels. The electronic states are quantized at energies

$$E_N = (N + 1/2)\hbar\omega_c, \quad (2.2)$$

where N is the Landau quantum number and $\omega_c = eB/m^*$ is the cyclotron frequency with the effective electron mass m^* . For simplicity, terms describing the Zeeman effect and the Rashba splitting have been neglected. This leads to a discrete density of states at the above energies

$$D(E) = \frac{1}{2\pi l_B^2} \sum_N \delta(E - E_N) \quad (2.3)$$

with the magnetic length $l_B = \sqrt{\hbar/eB}$. The quantization of the energy states in a magnetic field manifests itself in the transport properties of the 2DEG. When the separation of the Landau levels is considerably larger than the broadening of the levels, one has to distinguish between two transport regimes. In both of them,

the longitudinal resistance R_{xx} reflects the density of states at the Fermi energy in the bulk. For $E_F = (N + 1/2)\hbar\omega_c$, the Fermi energy is located in a Landau level and the electronic states of the corresponding Landau level are delocalized over the entire bulk. This makes backscattering possible and a large resistance is observed (Fig. 2.6). If the Fermi energy in the bulk lies between two Landau levels, however,

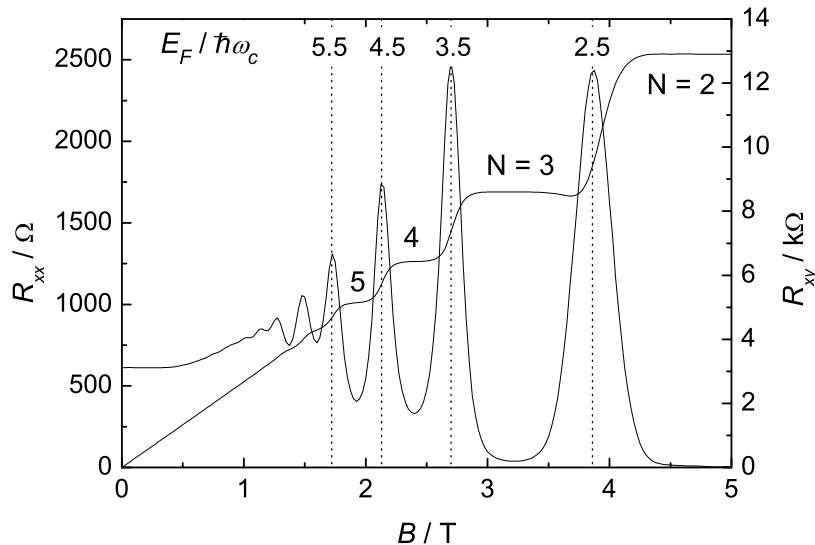


Figure 2.6: The longitudinal resistance R_{xx} and the Hall resistance R_{xy} are plotted as a function of the external magnetic field. The respective Fermi energies are given for the SdH maxima and the transitions between the quantum Hall plateaus, which appear for $E_F = (N + 1/2)\hbar\omega_c$.

the transport occurs only in the edge channels³. Then, no backscattering is possible, because the channels at opposite edges are widely separated, and the longitudinal resistance vanishes. The resulting oscillatory behavior of the longitudinal resistance in magnetic field was observed for the first time by Shubnikov and de Haas in 1930 [70] and has been referred to as Shubnikov-de Haas (SdH) oscillations since that time.

³ A comprehensive review of the edge-state transport has been published by Haug [69].

When the magnetic field is too low to cause a separation in energy between the Landau levels, the Hall resistance R_{xy} increases linearly as a function of magnetic field:

$$R_{xy} = \frac{B}{ne}, \quad (2.4)$$

where n is the carrier density in the 2DEG. For high magnetic fields, the Landau levels are clearly separated and plateaus according to the quantum Hall effect (QHE) [71] can be observed (see Fig. 2.6) with

$$R_{xy} = \frac{h}{e^2} \frac{1}{N}. \quad (2.5)$$

Here, the Landau quantum number N gives the number of Landau levels below the Fermi energy. The transitions between the QHE plateaus occur, when a Landau level crosses the Fermi energy.

Since both the longitudinal and the Hall resistance show distinct features, whenever a Landau level crosses the Fermi energy, the experimental observation of Shubnikov-de Haas oscillations and the QHE grant experimental access to the evolution of the Landau levels in magnetic field.

Measurements in a magnetic field up to 8 T have been performed to investigate the Landau level dispersion of the conduction band (CB). When the gate voltage is lowered for a fixed magnetic field, the Landau levels are subsequently shifted above the Fermi energy. The number N of occupied Landau levels is determined from the quantum Hall resistance $R_{xy} = \frac{h}{e^2} \frac{1}{N}$. The results for an 80 Å QW are shown for various magnetic field values (Fig. 2.7). For $N > 1$, the experimental data is in good agreement with the theoretical LL dispersion. However, the transition to $N = 0$, i.e., to insulating behavior, is not consistent with the theoretical model. The unexpected transition to an insulator can be explained by density fluctuations in the 2DEG. These fluctuations have been verified by Hall measurements on different voltage probes of the same sample, yielding different carrier concentrations. When the Fermi energy is close to the conduction band minimum, one region of the device can already be turned into an insulator while the 2DEG in the vicinity of the volt-

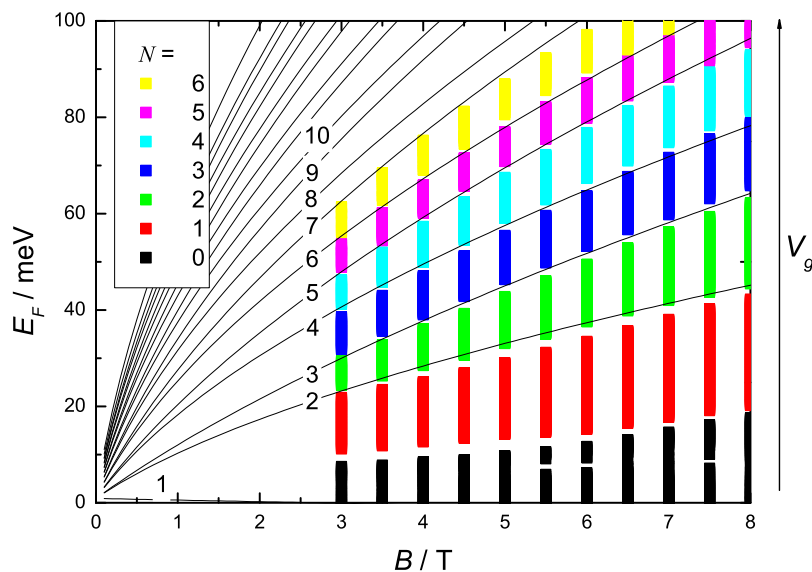


Figure 2.7: The experimentally determined Landau quantum numbers N (colour coded), depending on the B -field and the gate voltage, are in good agreement with the theoretical calculations for the Landau level dispersion (black lines).

age probes is not entirely depleted yet. Nevertheless, transport through the device will not be possible due to that insulating region and the entire sample will be seen insulating.

For low electron densities ($n \leq 8 \cdot 10^{10} \text{ cm}^{-2}$), a transition to an insulating state is observed for a finite magnetic field (Fig. 2.8)⁴. The transition can be understood by the LL dispersion. When the Fermi energy is close to the CB minimum, the lowest Landau level will cross E_F for a magnetic field B_{crit} . In principle, this transition occurs for all Fermi energies at a certain magnetic field, but B_{crit} is experimentally accessible only for low densities. Since no Landau level from the conduction band is

⁴ Corresponding behavior is also observed for low hole densities, if the device is in the p -conducting regime.

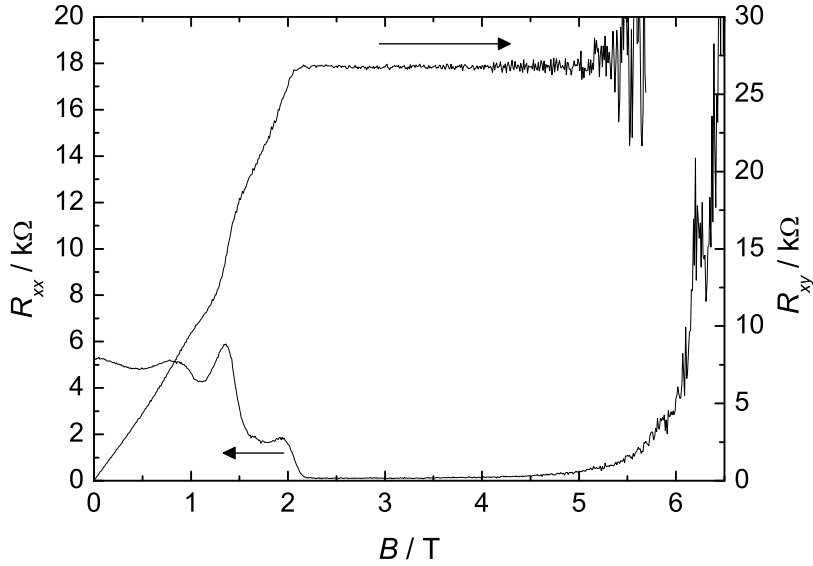


Figure 2.8: R_{xx} and R_{xy} are measured for a sample with a low electron density.

below the Fermi energy for $B > B_{\text{crit}}$, the sample is insulating. The B -field value for the transition is shifted towards smaller values for decreasing densities, i.e., lower Fermi energies, due to the monotonic behavior of the lowest Landau level in magnetic field.

While the transition to an insulator for finite magnetic field is observed independently of the QW width, one has to distinguish between a normal and an inverted band structure, when the Fermi energy is located in the fundamental gap for $B = 0$. For a normal band structure, the gap between the lowest Landau levels of the valence band and the conduction band, respectively, opens up in magnetic field. Consequently, the sample remains insulating when a magnetic field is applied.

In contrast, conductance can be established in magnetic field for a sample with an inverted band structure (Fig. 2.9). Even though the device is insulating for $B = 0$, a transition to a conducting state is observed for a finite magnetic field $B_{\text{crit},1}$. When

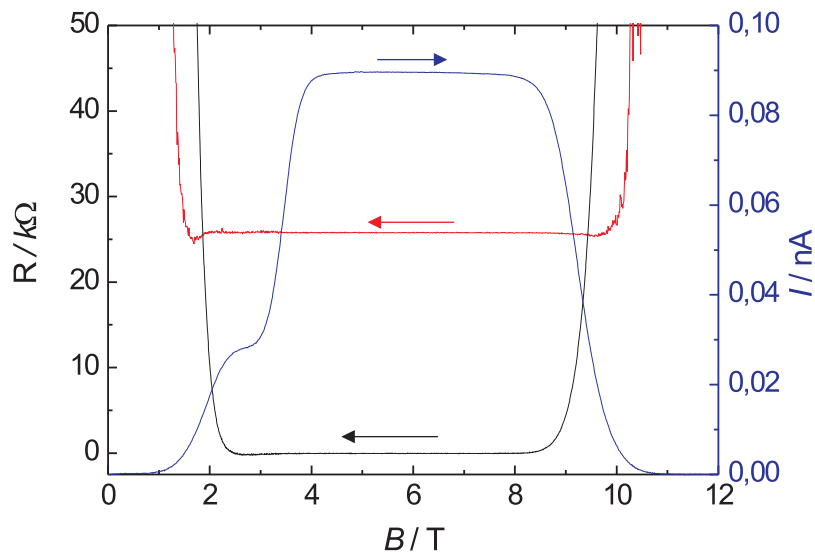


Figure 2.9: Longitudinal resistance (black), Hall resistance (red) and sample current (blue) are shown as a function of B . The gate voltage is such that the sample is insulating for $B = 0$.

the magnetic field is increased further, the sample becomes insulating again at $B_{\text{crit},2}$. This unique transition is attributed to the peculiar LL dispersion. For a magnetic field close to zero, the Fermi level is located between the lowest Landau levels of the conduction band and the valence band. When the magnetic field is increased, these two peculiar Landau levels shift into the energy gap. At the first critical value $B_{\text{crit},1}$, the CB Landau level crosses the Fermi level. Subsequently, exactly one occupied Landau level is below E_F , resembling the familiar quantum Hall state. This is reflected in a transport properties corresponding to the QHE regime; R_{xx} vanishes and R_{xy} is quantized at h/e^2 . For $B = B_{\text{crit},2}$, the Landau level originating from the valence band crosses the Fermi level. For larger fields, E_F will be located in the energy gap again and insulating behavior is observed.

When the Fermi level is lowered further into the gap, the conducting regime in magnetic field, $B_{\text{crit},1} \leq B \leq B_{\text{crit},2}$, narrows, until E_F finally reaches the crossing

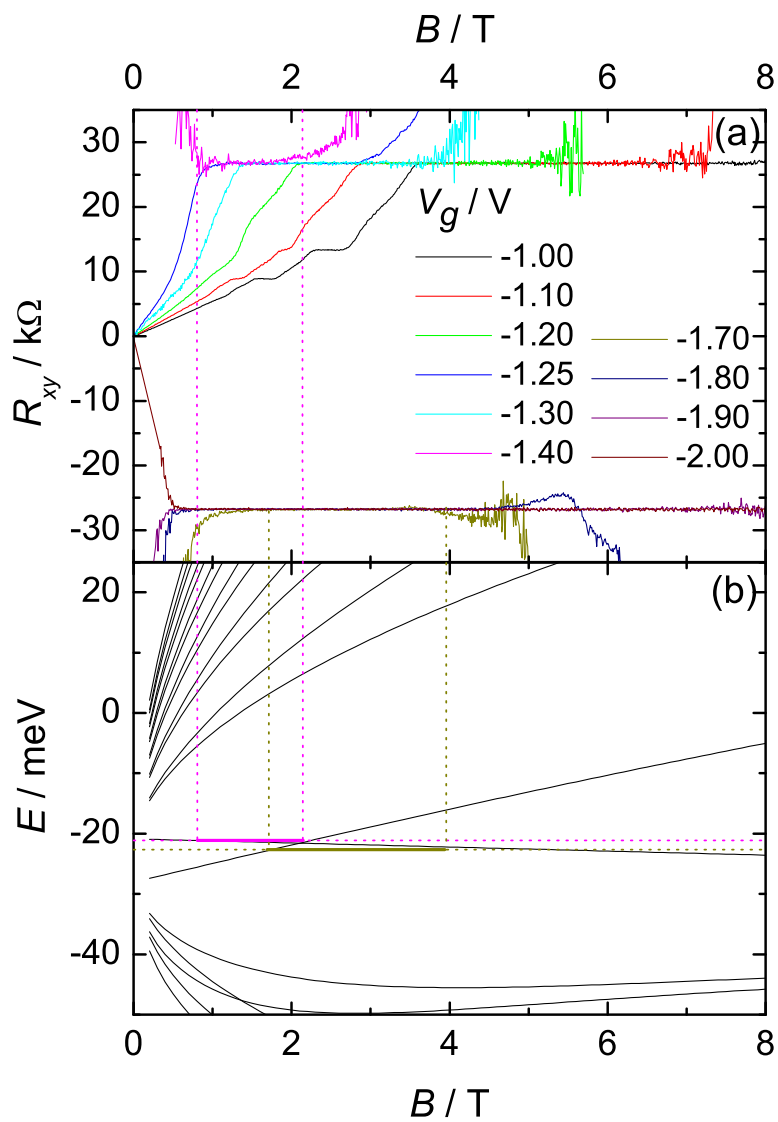


Figure 2.10: (a) The Hall resistance is presented for various gate voltages. (b) The calculated LL dispersion (black lines) is in good agreement with the experimental results (indicated by dashed vertical lines).

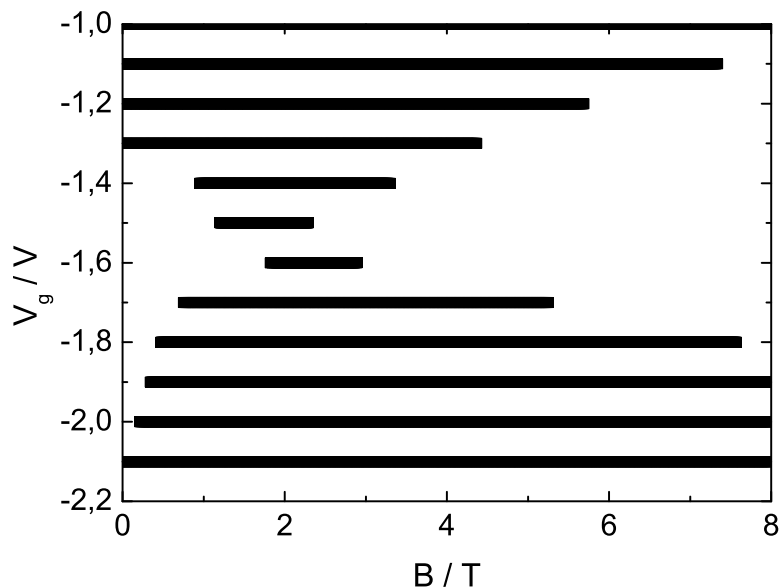


Figure 2.11: The horizontal lines indicate the B -field range, in which the sample is conducting for the respective gate voltage. The conducting regime is smallest when V_g approaches -1.6 V.

point $E(B_{\text{cross}})$. For Fermi energies below the LL crossing point, a p -conducting QH state appears in magnetic field. As shown in Fig. 2.10, the B -field values for the transition between the conducting and the insulating regime depend on the gate voltage. For $-1.4 \text{ V} \geq V_g \geq -1.9 \text{ V}$, the Fermi energy is located in the energy gap at $B = 0$. The B -field range, for which the sample is conducting, depends on the exact value of the gate voltage. For the entire transition from clear n -conductance to p -conductance, the experimental results are consistent with the theoretical modelling of the LL dispersion (Fig. 2.10). When the sample is insulating for $B = 0$, both a transition to an n -conducting state ($V_g = -1.4 \text{ V}$) and to a p -conducting state ($V_g \leq -1.7 \text{ V}$) can be observed for a suitable gate voltage.

Using this method, the dispersion of the lowest Landau levels can be mapped experimentally. For several samples with an inverted band structure, a good agreement

with the LL dispersion was obtained. In addition, the quite exact determination of the B -field value for the LL crossing can verify the nominal value⁵ of the QW width. For instance, the results shown in Fig. 2.11 were obtained on a sample which was designed as a 55 Å QW, implying a normal band structure. However, the observation of the LL crossing indicates an inverted band structure and a QW width of $d_{QW} \approx 65$ Å can be deduced from $B_{\text{cross}} = (2.0 \pm 0.3)$ T

In conclusion, a unique re-entrant quantum Hall state has been observed for devices with an inverted band structure. While the sample is insulating for $B = 0$, a conducting state appears at a certain magnetic field. For an even higher field, the sample is turned into an insulator again. These transitions can be explained by the peculiar LL dispersion, causing a crossing of Landau levels originating from the conduction band and the valence band, respectively, within the energy gap. The experimental observation of the LL crossing allows for a precise determination of the QW width. In contrast, the band gap of a sample with normal band structure opens up in magnetic field, so that the sample remains insulating when the Fermi energy is in the gap for $B = 0$.

2.3 Summary

In this chapter, the peculiar band structure of HgTe quantum well structures was studied by transport experiments. Since the band gap is not exceeding 80 meV for the investigated structures, the Fermi energy can be shifted from the conduction band to the valence band by applying a negative gate voltage. This leads to a transition from n - to p -conductance via an intermediate insulating regime, which is observable in our experiments. A low intrinsic carrier density is a prerequisite for this transition, because the influence of the gate is limited due to screening of the potential. While the carrier type in the gated region can be changed, the leads remain n -type, independent of the gate voltage. Hence, the sample contains a

⁵ For several reasons, the thickness of MBE grown can deviate from the value aimed for.

reversed diode at one of the boundaries between the n - and the p -region. Employing a simple model, the tunneling resistance of the reversed diode can be estimated to be only some few $10\text{ k}\Omega$, which permits charge transport through the device.

Samples with an inverted band structure, i.e., $d_{QW} < d_{\text{crit}}$, show unusual transport properties, when the Fermi energy is located in the energy gap. While the sample is insulating for $B = 0$, a finite magnetic field can induce a transition to a conducting state. For larger magnetic fields, the sample becomes insulating again. This effect can be explained by the crossing of Landau levels originating from the valence and conduction band, respectively, due to the inverted band structure.

To our knowledge, both the tuning from n - to p -type and the transition from an insulating to a conducting state in magnetic field have not been observed so far in transport measurements.

Chapter 3

The Quantum Spin Hall Effect

In recent years, spin Hall effects have aroused a lot of interest both theoretically and experimentally [11–13, 24, 25]. This emerging interest is not only founded in the relevance for the fundamental scientific understanding of the effect, but is also based on its possible applications in the field of semiconductor spintronics. For spin Hall systems, the spin current flows without dissipation. However, the accompanying charge current is subject to the general transport properties of the doped semiconductor, which makes the combined system of charge and spin current dissipative. To avoid the objectionable dissipation due to the charge transport, it is necessary to separate the spin transport from the charge transfer through the device. In this context, the so-called Quantum Spin Hall (QSH) effect was predicted [18, 19]. In a QSH system, edge states transport yields quantized spin and charge conductance, while the bulk is insulating. Since the transport of the spin-polarized carriers in the QSH channels is non-dissipative, QSH systems are considered to be ideal candidates for spintronics devices.

Bernevig *et al.* predicted the existence of a QSH state for HgTe QW structures with an inverted band structure [23]. This prediction is verified by measurements on various devices presented in this chapter, providing the first experimental observation of the QSH effect. Beyond this, the influence of an external magnetic field and the temperature on the QSH state are investigated.

3.1 Introduction to the Quantum Spin Hall effect

A dissipation-less spin current was predicted to flow in a so-called Spin Hall insulator (SHI), whereas the charge conductance is zero in such a system [72]. This SHI state is expected to appear in zero-gap and narrow-gap materials such as Hg-based and Pb-based semiconductor compounds. When the material is undoped, the Fermi level is located in the energy gap which makes it insulating with respect to the charge transport. For zero-gap materials, an energy gap at the Γ point can be opened by uniaxial strain. Even though the charge conductance vanishes, the spin-conductance is non-zero because of unequal Fermi distributions for the holes in the light- and heavy-hole subbands in these systems. Motivated by this initial suggestion, a quantized spin Hall effect was proposed [18,19]. Like for a SHI system, the Fermi energy in the bulk is located in the energy gap for such a system. However, the spin current can be carried by edge states, also allowing for non-dissipative charge transport. Due to the analogy to the well-known quantum Hall effect (cf. Sec. 2.2), this effect is called the quantum spin Hall (QSH) effect.

In their prediction of the QSH effect [19], Bernevig and Zhang utilized the fact that the spin-orbit Hamiltonian of a two-dimensional system can be expressed by $\hat{H}_{SO} \sim E\sigma_z(xp_y - yp_x)$ which resembles the term describing a perpendicular magnetic field $\hat{H} \sim B(xp_y - yp_x)$. This similarity suggests that the electric field E entering the SO Hamiltonian can be represented by an effective magnetic field, causing Landau level-like edge states for the two spin subsystems¹. Since the spin σ_z of the electron enters the SO Hamiltonian, the effective B -field points in opposite direction for spin-up and spin-down electrons. Consequently, spin-up and spin-down electrons counter-propagate at a given edge (Fig. 3.1). Considered separately, the edge states are (anti-)chiral states. Due to the reversed chirality for electrons with opposite spin, the total system of the states at a given edge forms a helical liquid [73].

¹ Using an effective mass model, Kane and Mele demonstrated the quantization of the spin conductance for graphene. The existence of the QSH edge states in that material was shown introducing a tight-binding model [18].

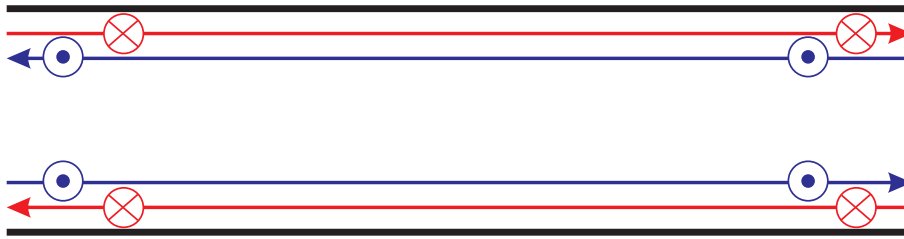


Figure 3.1: In a QSH system, electrons with opposite spin move in different directions at a given edge.

Kane and Mele introduced a Z_2 classification for the topological description of the novel time reversal invariant system [74]. Similar to the topological index describing the charge quantum Hall effect [75], QSH systems can be characterized by a topological number Δ as well². This integer describes the number of pairs of helical states at one edge [18, 23]. For a QSH insulator, Δ is an odd number. The counter-propagating edge states at a given edge form a Kramers pair and time reversal invariant perturbations cannot destroy the topological order. It was shown that the edge states are robust against weak magnetic disorder and electron-electron interaction [73, 78]. Since backscattering can be neglected, transport in the edge channels is non-dissipative and both spin and charge conductance are quantized: for the spin conductivity, $\sigma^s = e/(2\pi)$ is obtained and the charge conductivity is quantized with $\sigma = 2e^2/h$. However, when a phase transition to $\Delta = \text{even}$ occurs, the hybridization of the edge modes opens up a gap even at the sample edge, turning the sample into a spin Hall insulator [79].

Amongst other materials [18, 76, 80], the existence of the QSH insulator has been predicted for HgTe/CdTe quantum wells [23]. In this description³, the electronic states are given by a relativistic Dirac equation. Due to the large separation of the other subbands, only the E_1 and the H_1 band are considered in an effective

² In some references, the topological index for the QSH state is called I [74, 76] or Z_2 [77] instead.

³ The following description is based on the prediction by Bernevig *et al.* [23].

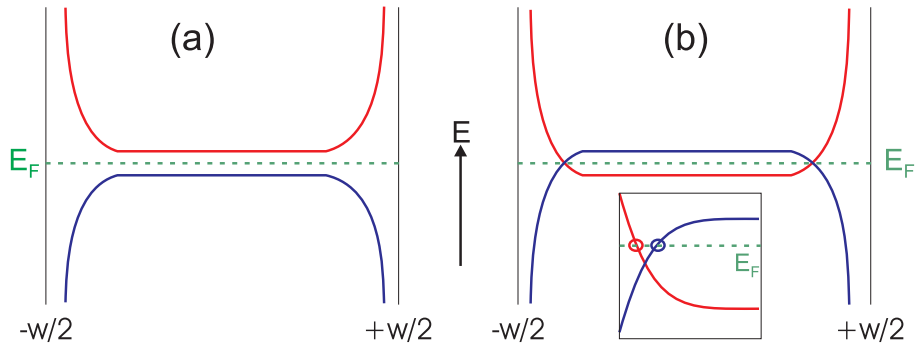


Figure 3.2: The spectrum of the lowest states in valence and conduction band is sketched schematically. (a) For a normal band structure, the Fermi energy is located in the energy gap for the entire sample. (b) When the band structure is inverted, the Fermi energy is in the gap for the bulk as well. However, the energy states cross the Fermi energy at the edges, forming the QSH channels (inset).

four-band model. Here, the E_1 band basically consists of the two spin states of the s orbital. The H_1 band is composed of the spin-orbit coupled p orbitals $|p_x + ip_y, \uparrow\rangle$ and $|-(p_x - ip_y), \downarrow\rangle$. The significant parameter of this model is the Dirac mass M , which is equivalent to the energy difference between the E_1 and the H_1 band at the Γ point. For a normal band structure, i.e., $d_{QW} < 63 \text{ \AA}$, the E_1 band lies above the H_1 band and M is positive, while an inverted band structure is identified by a negative Dirac mass. The resulting sign change of M at the phase transition for $d = d_{\text{crit}}$ leads to a variation of the topological number by 1. Hence, the sample is in the QSH state for one side of the transition, but represents a trivial insulator for the other side. Applying a tight-binding model, it is shown that the nontrivial QSH insulator state exists for an inverted band structure. Fig. 3.2 illustrates the lowest states of the valence and conduction band, respectively. For a normal band structure, the gap increases at the sample edge. This provides a trivial insulating state, when the Fermi energy is in the energy gap ($M > 0$). However, the situation changes drastically for an inverted band structure. The Fermi energy in the bulk is in the gap as well, but M is negative due to the inverted band structure. Close to

the sample edge, the two states cross, establishing a domain wall between a region with $M < 0$ in the bulk and one with $M > 0$, which is connected to the vacuum. Since the QSH states originating from the conduction and valence band cross, the existence of QSH edge channels is ensured for all Fermi energies within the band gap [see inset of Fig. 3.2 (b)]. Due to the crossing of the states, a QSH insulator can not be adiabatically deformed into a trivial insulator. In this precise sense, the QSH insulator represents a topologically new state of matter.

3.2 Experimental observation of the Quantum Spin Hall insulator

For the experimental investigation of the QSH effect, several devices have been fabricated from HgTe-based QW structures. The QW width of the individual structures was in the range from 45 Å to 120 Å. While samples with $d_{QW} < 63$ Å have a normal band structure, a larger QW width causes an inversion of the band structure. From these QW structures, Hall bar devices with different dimensions ($L \times W$) were fabricated (see Fig. 3.3). All devices presented below can be turned into an insulator by applying moderate gate voltages due to a low intrinsic ($V_g = 0$) electron density. Unless stated otherwise, the experiments were done in a $^3\text{He}/^4\text{He}$ dilution refrigerator at base temperature $T < 30$ mK using standard AC lock-in measurement techniques.

For various devices presented in this chapter, the nature of the band structure was investigated by magneto-transport measurements as introduced in Sec. 2.2. For structures with a small QW width $d_{QW} < d_c$, the energy gap between the lowest Landau levels increases in magnetic field confirming the normal band structure. On the other hand, the LL crossing for devices with an inverted band structure allows for a precise determination of the QW width. Fig. 3.4 shows the theoretical B -field values (cf. Sec. 1.1) for the Landau level crossing for quantum wells with an inverted

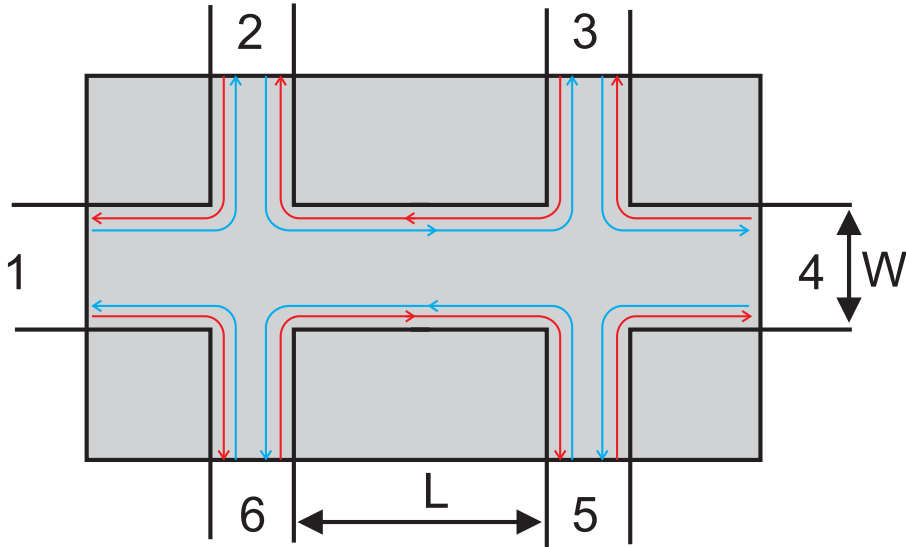


Figure 3.3: The schematic sketch of the devices shows the QSH edge states under the gate (shaded region). The ungated parts of the sample are n -type.

band structure (red circles). These values are used to adjust the QW width of the investigated samples (blue squares). The possible error in the measurement of B_{cross} results in a small uncertainty in the experimental determination of the QW width.

According to the Dirac model introduced in the previous section, it can be shown that the LL crossing only occurs for an inverted band structure. In this model, the two Landau levels closest to the energy gap are given by $E_{\pm} = C \pm M - (D \pm B)l_c^{-2}$. Here, B , C and D are material-specific parameters⁴, M is the Dirac mass and $l_c = \sqrt{\frac{\hbar}{eB_{\perp}}}$ the magnetic length according to the perpendicular magnetic field B_{\perp} . The condition for the LL crossing, $E_{+} = E_{-}$, leads to $B_{\text{cross}} = \frac{\hbar M}{eB}$. Since the parameter B is negative in general, a LL crossing will only appear for $M < 0$, i.e., for an inverted band structure. The above expression for B_{cross} applies very well for $d_{\text{QW}} \leq 85 \text{ \AA}$, if the dependence of the energy gap on the QW width is considered (cf.

⁴ Note that the parameter B of the Dirac model is not related to the magnetic field. The notation as B is chosen according to Ref. 23. To avoid confusion, the magnetic field is given with an index in this context, e.g., B_{\perp} .

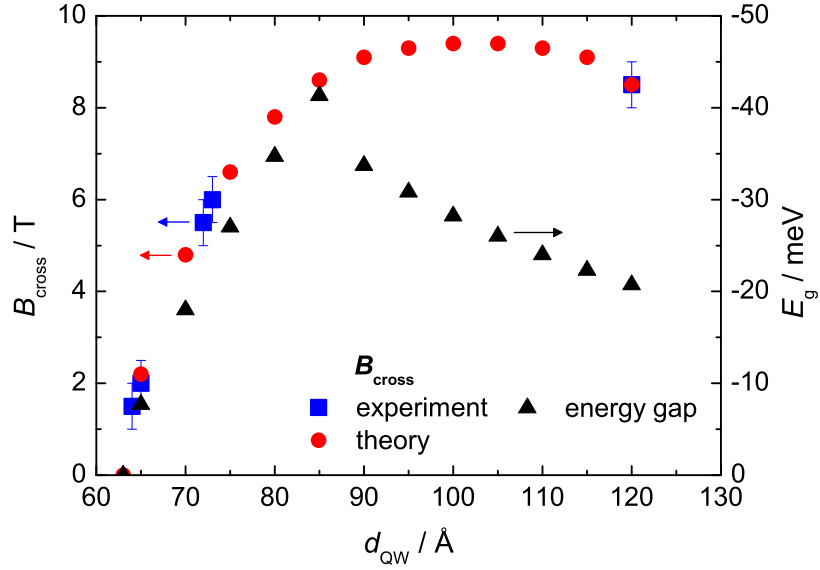


Figure 3.4: The B -field value of the LL crossing is determined experimentally (blue squares) and calculated theoretically (red circles). For the energy gap E_g (black triangles), the negative values indicate the inverted band structure.

Fig. 3.4). For $d_{QW} \approx 85 \text{ \AA}$, the E_1 band falls below the H_2 band (cf. Fig. 1.2). This makes the four-band Dirac model based solely on the E_1 and the H_1 band invalid and the LL crossing for wider QWs can not be deduced from the above expression. Anyway, the LL crossing was observed for such QWs as well, confirming the inverted band structure. Using this method, it can be established experimentally⁵, if the devices have a normal or an inverted band structure.

Fig. 3.5 shows the longitudinal resistance $R_{14,23} = U_{23}/I_{14}$ (cf. Fig. 3.3) as a function of the applied gate voltage for two Hall bar structures with dimensions

⁵ The method is not appropriate to verify the exact QW width for $d_{QW} > 80 \text{ \AA}$. In this regime, the variation of B_{cross} is comparable to the uncertainty in the experimental value. However, the existence of the LL crossing satisfactorily shows the inverted band structure.

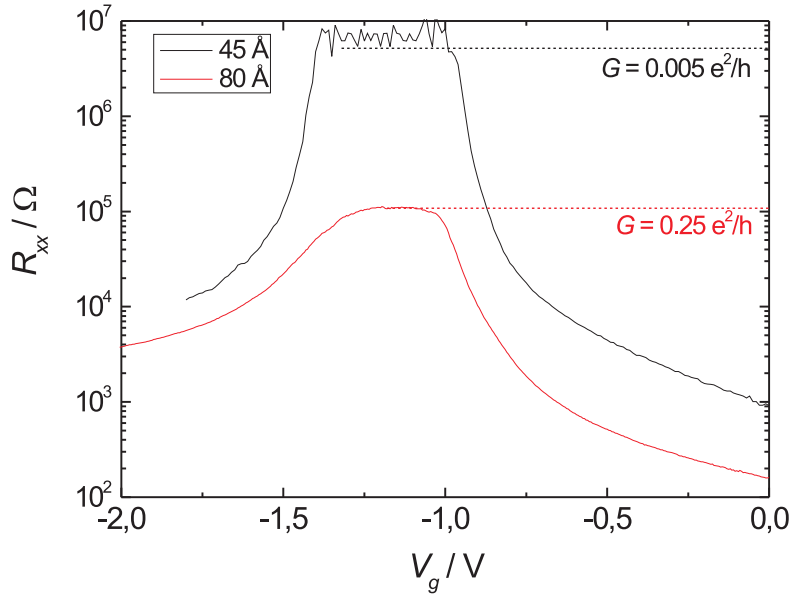


Figure 3.5: The longitudinal resistance is measured as a function of the gate voltage for a 45 Å QW (black) and a 80 Å QW (red), respectively.

($L \times W$) = ($20 \mu\text{m} \times 13.3 \mu\text{m}$) and a QW width of 45 Å and 80 Å, respectively⁶. Both devices are intrinsically n -doped. When a negative voltage is applied, the longitudinal resistance is increased due to the depletion of the 2DEG. One can clearly distinguish between two different regimes when the devices are tuned to the insulating state for $V_g \approx -1.0$ V. For the 80 Å QW, a longitudinal resistance of approximately 100 kΩ is observed, which corresponds to a conductance of $G \approx 0.25 e^2/h$ (red trace). In contrast, the resistance of the 45 Å sample is about two orders of magnitude larger and the conductance is almost zero (black trace). In fact, the observed resistance $R \sim 10 \text{ M}\Omega$ can be attributed to the intrinsic noise level of the lock-in setup used for the measurements. For both samples, the resistance again decreases

⁶ For both samples, the nominal QW width has not been verified by the LL dispersion. However, due to its large separation from d_{crit} , the samples are clearly in the normal and inverted band structure regime, respectively.

to approximately $10 \text{ k}\Omega$ for $V_g \approx -2.0 \text{ V}$, when the sample is p -conducting. As a result of additional experiments on several other devices with different QW width, the behavior in the insulating regime can be associated with the type of the band structure: All samples with an inverted band structure, i.e., $d_{QW} > 63 \text{ \AA}$, showed a finite resistance stays not exceeding $100 \text{ k}\Omega$, whereas conductance was entirely suppressed for samples with a normal band structure. This significant distinction is a clear indication of the existence of the QSH state for devices with an inverted band structure, even though the observed resistance values do not match the theoretical prediction.

For a four-terminal configuration, a vanishing resistance was predicted theoretically, while the two-terminal resistance, e.g., $R_{2\text{term}} = U_{14}/I_{14}$, is expected to be quantized at $h/(2e^2)$ [23]. The deviation of the resistance from the predicted value can be explained by the properties of the contacts. In the theoretical prediction, ideal contacts to the QSH edge states were assumed, i.e., the potential of the edge states can be probed without any influence due to the contacts. In the investigated samples, the contacts are always n -doped, which can not be considered as ideal with respect to the QSH states. Unlike for a quantum Hall system, the edge states in a QSH system propagate in both directions at a given edge (cf. Fig. 3.3). Originating from different sources, the edge states reaching the same contact carry a different potential. In the n -type contacts, the edge states necessarily equilibrate and backscattering becomes possible. Hence, the voltage difference between neighbouring contacts does not vanish even though they are connected by non-dissipative edge channels. A simple Landauer-Büttiker formalism [81] can be applied to determine the influence of the n -doped contacts. The current I_i in a contact i (cf. Fig. 3.3) can be calculated from

$$I_i = (e/h) \sum_j T_{ij}(\mu_j - \mu_i).$$

Since the edge states are non-interacting, the transmission coefficient T_{ij} is unity for neighbouring contacts and zero otherwise. In the measurements, a current I is injected from contact 1 to contact 4, i.e., $I_1 = -I_4 = I$, while I_i vanishes for all

other contacts serving as voltage probes. When total equilibration of all edge states in each contact is assumed, a four-terminal resistance of $(h/2e^2)$ is obtained. The two-terminal resistance is determined by the number of the voltage probes between the current source and drain. Between each pair of neighbouring contacts, a voltage $V_i = I \cdot (h/e^2)$ drops, adding up to a total voltage drop of $(n + 1)V_i$, where n is the number of voltage probes. This yields a two-terminal resistance of $(3h)/(2e^2)$ for a Hall bar geometry with two voltage probes on each side as shown in Fig. 3.3.

While the influence of the n -doped contacts causes a finite resistance contradicting the initial theoretical prediction [23], it still does not give a conclusive picture for the observed four-terminal resistance of around 100 k Ω . However, the enhanced resistance can be explained by potential fluctuations within the sample. Due to the narrow energy gap, these fluctuations can create local n - and p -conducting regions embedded in the insulating region under the gate. In a quantum Hall system, the position of the edge states is determined by a local Fermi energy corresponding to a half-integer filling factor (cf. Sec. 2.2). Therefore, the edge channels will evade potential fluctuations and dissipationless transport is conserved. In contrast to the QH regime, the position of the QSH edge states depends on the dispersion of the energy states close to the sample edge. The spatial separation of the QSH states from the sample edge can be regarded as constant independent of possible potential fluctuations. Consequently, the edge states will enter each conducting region located at the sample edge (Fig. 3.6). These regions appear due to potential fluctuation which are caused, e.g., by impurities or the roughness of the interfaces between the well and both barrier layers. Furthermore, a fluctuation of the well width by one mono-layer is conceivable despite the high accuracy of the MBE growth. A variation of d_{QW} shifts the energy levels. Thus, the Fermi energy is possibly not located within the gap for the entire device. Like for the n -doped contacts, this leads to an equilibration of the potential carried by the edge states. Since the otherwise independent edge states can interact, backscattering is possible and yields an increase of the voltage drop.

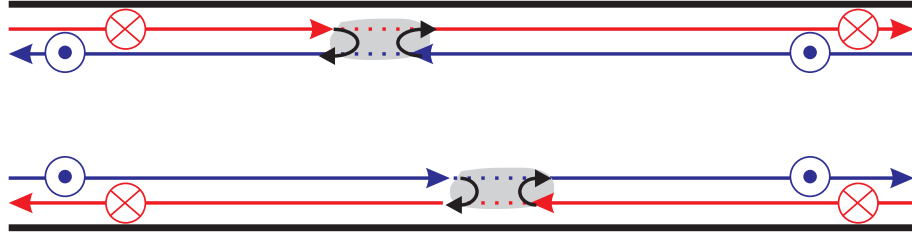


Figure 3.6: When the QSH edge states (red and blue) enter a doped region (grey), the edge states can interact.

As a second mechanism, inelastic scattering can contribute to the longitudinal resistance. While the edge states are robust against elastic scattering, inelastic scattering can give rise to backscattering. Using realistic parameters for n -doped samples ($n = 5 \cdot 10^{11} \text{ cm}^{-2}$ and $\mu = 10^5 \text{ cm}^2/\text{Vs}$), an elastic mean free path $\lambda_e \approx 1.2 \mu\text{m}$ is obtained. The inelastic mean free path λ_i can be estimated to be several times larger. This assumption is corroborated by the interference effects observed in ring structures with a radius of $1 \mu\text{m}$, which will be presented in Ch. 5. The circumference can be seen as a lower limit for the inelastic mean free path, because inelastic scattering would destroy the phase coherence. In addition, other experiments on HgTe QW devices, which have densities and mobilities comparable to the values given above, show phase coherence for lengths up to $20 \mu\text{m}$ [34]. Taking these experimental findings into account, an inelastic mean free path of at least $10 \mu\text{m}$ is a reasonable estimate⁷. Since the mean free path decreases with the electron density, its value in the insulating regime will be smaller than for an n -doped sample and inelastic backscattering may occur on a length scale of the order of $1 \mu\text{m}$ for the QSH regime. Hence, the distance between the voltage probes exceeds the inelastic mean free path and the longitudinal is expected to be larger than $h/(2e^2)$, which is consistent with the experimental results. The length-dependence of the QSH conductance also explains, why the conductance vanishes for macroscopic Hall bars, i.e., $L \geq 600 \mu\text{m}$, and the devices show trivial insulating behavior (cf. Fig. 2.2).

⁷ A comparable ratio of inelastic and elastic mean free path was found for GaN quantum wells [82].

Hall bars with a length of $1 \mu\text{m}$ were fabricated from a 65 \AA QW⁸ to show the quantization of the resistance at $h/(2e^2)$ for the insulating regime. According to the above estimation, the sample dimensions are of the same order as the inelastic mean free path. In this case, backscattering can be neglected and a longitudinal resistance of $h/(2e^2)$ is expected. For two devices with $L = 1 \mu\text{m}$, a resistance of approximately $18 \text{ k}\Omega$ is observed in the insulating regime, i.e., R is slightly above $h/(2e^2)$ (Fig. 3.7). A full transition to the p -conducting regime could not be achieved, because the intrinsic carrier concentration of the 2DEG was increased due to the electron-beam lithography needed for the fabrication. The deviation from the quantized value in the insulating regime can be explained by residual backscattering. The QSH states follow the sample edge into the voltage probes, which are also tuned into the QSH regime by the top gate (cf. Fig. 3.3). In the investigated structures, the voltage probes are covered by the gate on a length of 500 nm and the total length of the edge states adds up to $2 \mu\text{m}$, which most probably exceeds the inelastic mean free path.

The width of the two devices is $0.5 \mu\text{m}$ and $1.0 \mu\text{m}$, respectively. The difference for the n -conducting regime is attributed to bulk properties. For the ($W = 1 \mu\text{m}$) device, a defect in the bulk can explain the reduced transmission through the n -type sample, yielding an almost constant resistance. The resistance in the insulating regime, however, is independent of the sample width. This is in contrast to the behavior for bulk-mediated transport, where the resistance is expected to scale like $R \propto W^{-1}$. Unlike for bulk conductance, the resistance for edge state transport is independent of the sample width as long the channels on opposite edges are clearly spatially separated. Hence, the results confirm the existence of the QSH edge states for the insulating regime.

The fluctuations on the signal, which appear in the insulating regime, are reproducible and not caused by, e.g., electrical noise in the measurement setup. They can be attributed to quantum interference effects, which depend strongly on the

⁸ This is the nominal value, the actual QW width might be slightly larger.

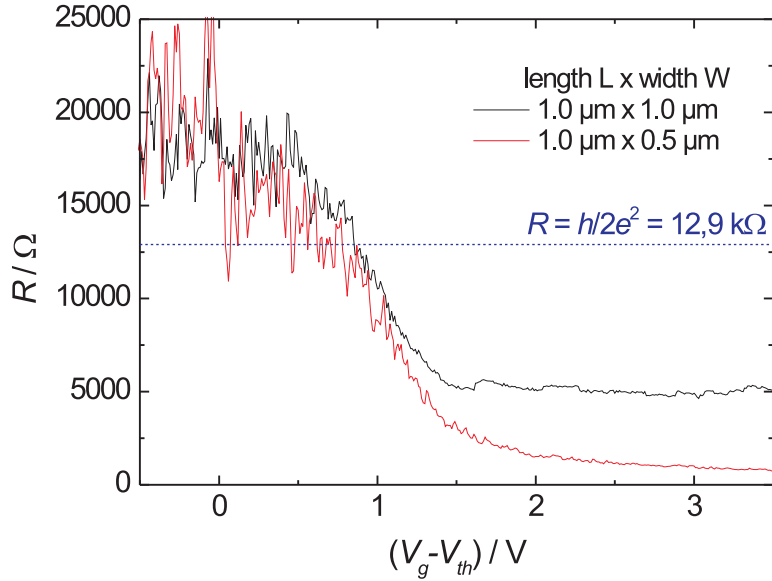


Figure 3.7: For two devices with $L = 1 \mu\text{m}$, the longitudinal resistance in the insulating regime is close to $h/(2e^2)$.

interface between the QSH region and the n -type contacts. This is confirmed by temperature-dependent measurements (Fig. 3.8). While the fluctuations are clearly visible at $T \approx 30 \text{ mK}$, the signal is much smoother at $T = 4.2 \text{ K}$. The transport in the QSH states as such remains apparently unaffected by the increase of temperature⁹ and a conductance close to $2e^2/h$ is observed in the insulating regime for both traces. Both measurements were done on the same ($1 \mu\text{m} \times 0.5 \mu\text{m}$) device using the same measurement setup so that spurious effects due to the lithographical process or specific properties of different measurement setups can be excluded to be responsible for the suppression of the fluctuations for elevated temperatures.

Another indication for transport due to edge states can be found in the results obtained by non-local measurements on a ($1 \mu\text{m} \times 1 \mu\text{m}$) Hall bar at 1.8 K . For these

⁹ The temperature dependence of the QSH effect will be investigated in detail in Sec. 3.4.

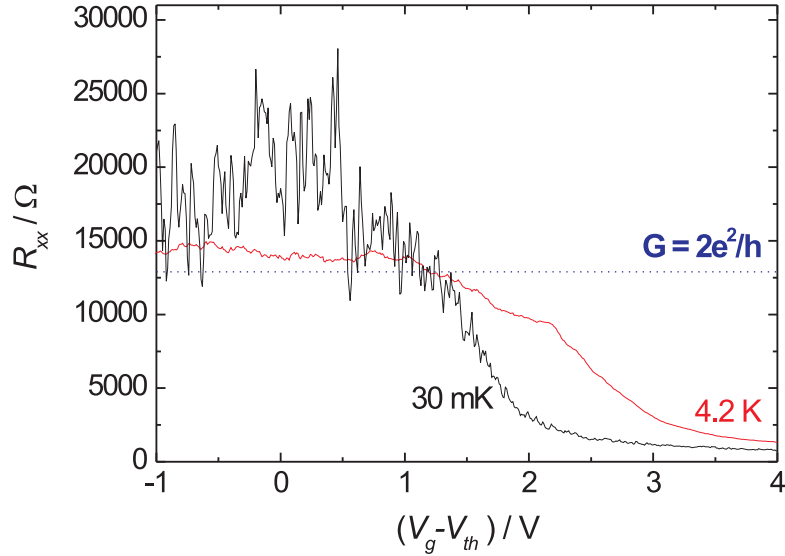


Figure 3.8: When the temperature is increased from 30 mK (black) to 4.2 K (red), the fluctuations in the insulating regime almost vanish.

measurements, e.g., contacts 2 and 6 of the Hall bar were used as current source and drain, respectively, while contacts 3 and 5 were used as voltage probes. For this and several other non-local contact configurations, a finite conductance was observed for the insulating regime (Fig. 3.9). For bulk conduction, no voltage difference is expected for the probes. Assuming strong scattering, the non-local voltage probes might get charged. However, the voltage difference would strongly depend on the potential landscape in the bulk, which is directly affected by a change of the Fermi level. Since this is not the case, the charging of the non-local voltage probes can be attributed to the edge states. These carry the potential of the current source and drain contact, respectively, to the neighbouring contacts. Hence, the non-local signal is constant for the entire insulating regime, which is in agreement with the experiments when the superimposed fluctuations are neglected. Thus, the results corroborate the above conclusion that the transport in the insulating regime is based on the existence of edge states.

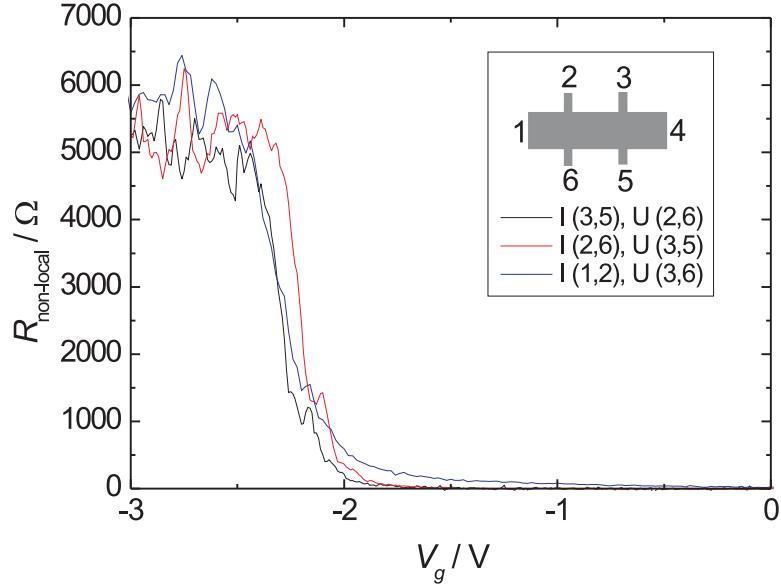


Figure 3.9: For different contact configuration, the non-local resistance was measured as a function of the gate voltage. The insulating regime occurs for $V_g \leq -2.2$ V. The inset provides contact configuration for the various traces.

The resistance value for the plateau can be qualitatively understood, when scattering and the influence of the additional contacts between the voltage probes is considered. Applying a simple Landauer-Büttiker formalism yields a non-local resistance $R_{26,35} = U_{35}/I_{26}$ of $2h/(3e^2)$. When backscattering is considered, a voltage drop along the edge states results in a reduced charging of the voltage probes. In addition, the voltage probes 3 and 5 are connected via contact 4, where the edge states, at least partially, equilibrate. For both reasons, the measured voltage difference will be smaller than the theoretical one. Similar considerations lead to the same qualitative behavior for $R_{36,12}$ and $R_{35,26}$.

In conclusion, the existence of the QSH effect was demonstrated for HgTe QW structures with an inverted band structure, whereas devices with a normal band

structure show trivial insulating behavior. In fact, our results provide the first experimental observation of the quantum spin Hall effect. Contrary to the theoretical prediction, the longitudinal resistance in a four-terminal configuration does not vanish for a QSH insulator. This is due to the counter-propagation of the QSH edge states at a single edge. The n -type contacts attached to the QSH regime enable an equilibration of the edge states, leading to a finite resistance $R = h/(2e^2)$ for a four-terminal configuration. A resistance close to this quantized value is observed for devices with a length of $1 \mu\text{m}$, where scattering can be neglected. When the samples are larger than the mean free path, the resistance is increased due to backscattering. Evidence for edge state transport in the QSH regime was provided in two different ways. First, the conductance is independent of the device width for a given length. Second, a strong non-local signal is observed for the insulating regime. Both findings rule out bulk transport to be responsible for the observed conductance of the QSH state.

3.3 QSH edge states in magnetic field

For $B = 0$, the helical edge states form a Kramers pair and are protected by time reversal symmetry. In an external magnetic field, however, time reversal symmetry is broken. In this case, elastic backscattering becomes possible and the conductance suppressed. To investigate the B -field dependence of the QSH insulator, measurements on Hall bars with $(L \times W) = (20.0 \mu\text{m} \times 13.3 \mu\text{m})$ were performed¹⁰. Fig. 3.10 (a) shows the magneto-conductance of a 73 \AA QW in the insulating regime. For $B = 0$, $G = 0.23 e^2/h$ is observed, which is a typical value for a device of the given dimensions (cf. Fig. 3.5). When a perpendicular magnetic field is applied, the conductance is destroyed, showing a very sharp, cusp-like peak in magnetic field with a full width half maximum (FWHM) value of 10 mT . For finite magnetic field $B > 50 \text{ mT}$, a residual conductance G_0 of $0.06 e^2/h$ is observed. This value is com-

¹⁰ Devices of this dimensions were chosen despite the enhanced scattering, since the standard size of $20.0 \mu\text{m} \times 13.3 \mu\text{m}$ was used for several devices.

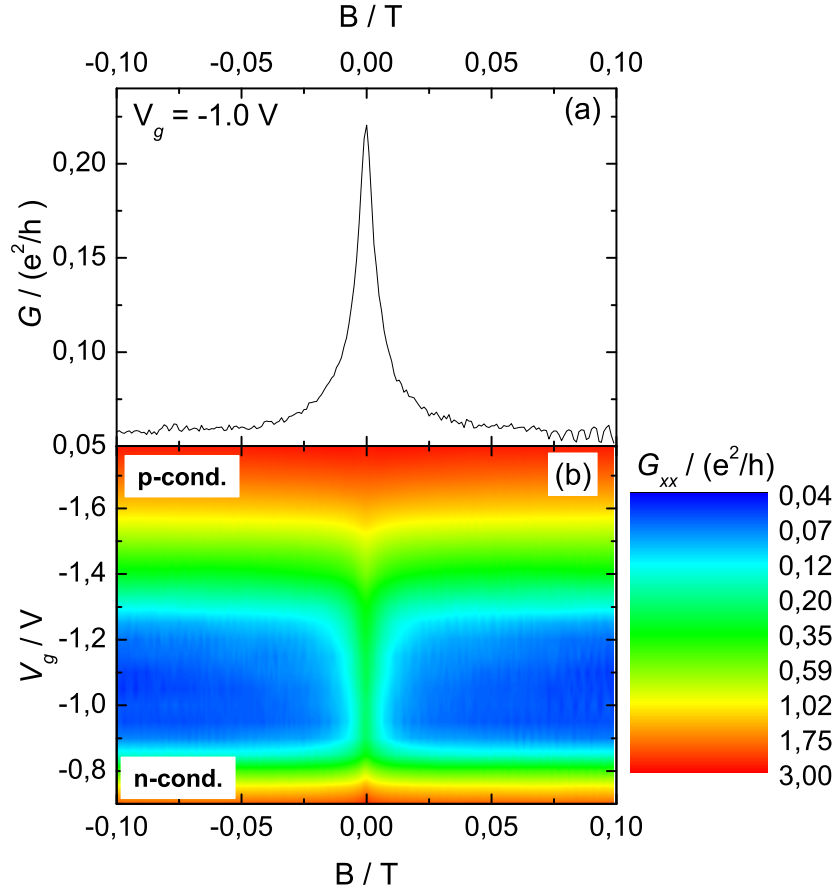


Figure 3.10: (a) The conductance due to the QSH state is suppressed, when a magnetic field is applied perpendicular to the 2DEG. (b) The conductance peak for $B = 0$ exists for the entire insulating regime.

parable to the conductance observed for a trivial insulator, i.e., $d_{QW} < d_{\text{crit}}$, which has been attributed to the noise floor of the measurement equipment (see Sec. 3.2). As can be seen in Fig. 3.10 (b), the behavior of the conductance as a function of magnetic field is independent of the exact value of V_g as long as the Fermi energy is in the gap, i.e., for $-0.9 \text{ V} \geq V_g \geq -1.25 \text{ V}$. The apparent widening of the peak close to the p -conducting regime is related to a slight increase of the background due to the onset of the bulk conductance.

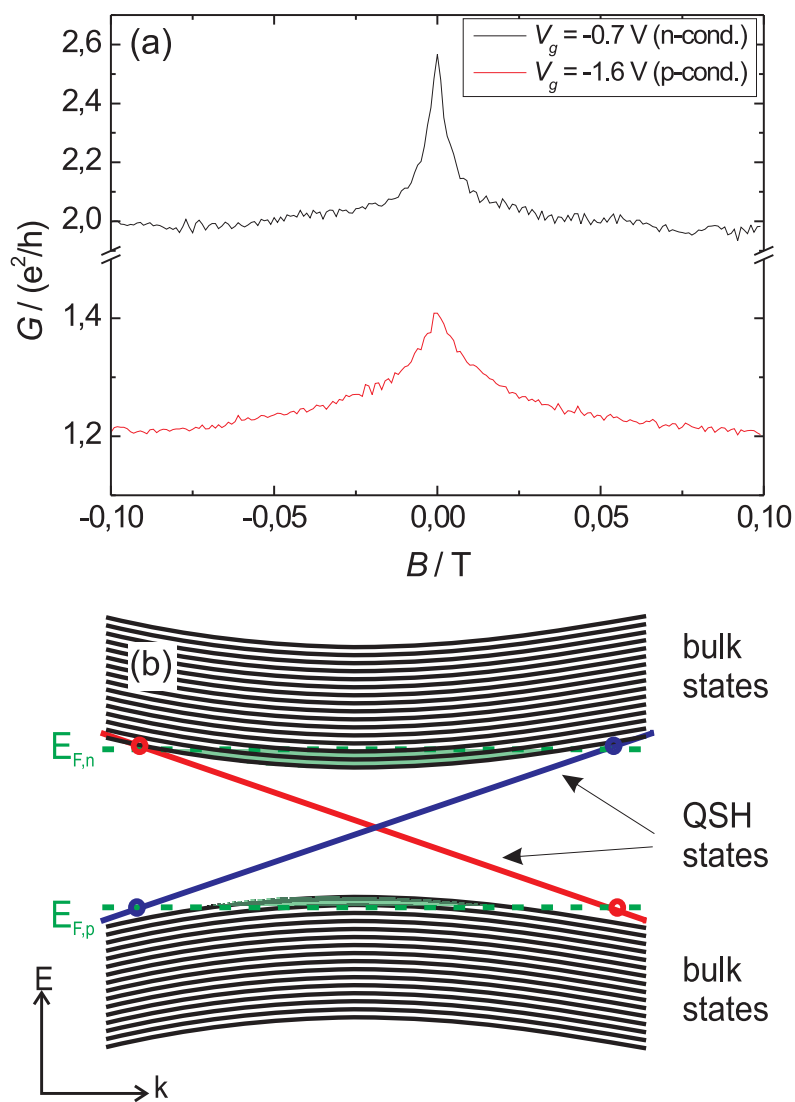


Figure 3.11: (a) The conductance as a function of B is shown for gate voltages close to the insulating regime. (b) The $E(k)$ dispersion for bulk and edge states is sketched schematically. The Fermi levels corresponding to the gate voltages used in (a) are indicated by dashed green lines.

The conductance peak around $B = 0$ exists for the n -doped and the p -doped regime as well. Fig. 3.11 (a) shows the magneto-conductance for the n - and p -regime at a gate voltage of -0.7 V and -1.6 V, respectively (cf. Fig. 3.10). Fig. 3.11 (b) provides a sketch of the $E(k)$ dispersion for bulk and QSH states (cf. Ref. 83). The qualitative agreement with the theoretically obtained dispersion [83] is sufficient to explain the observed behavior. For energies slightly above the conduction band minimum and below the valence band maximum, respectively, the QSH states still exist for finite k , even though the Fermi energy is not located in the gap. Thus, carriers in the bulk and edge channels contribute to transport simultaneously. While the conductance due to the QSH states is significantly suppressed for finite magnetic field, bulk transport is hardly affected.

Fig. 3.12 shows the conductance for devices with a QW width of 64 Å, 73 Å and 80 Å, respectively¹¹. For all devices, the conductance decreases sharply to a residual value for $B \approx 25$ mT. However, there is a strong variation of the residual conductance for finite magnetic field. For the 64 Å and the 80 Å device, $G_0 \approx 0.2 e^2/h$ is observed instead of a total suppression of the conductance. Based on these results, a coherent model for the B -field dependence can be developed.

First of all, the variation of the residual conductance is not caused by a shift of the noise level or of the zero-point in the measurement setup. For the 64 Å device, measurements were done in two different setups yielding identical results within the typical measurement accuracy.

Furthermore, a thermal activation of transport in the bulk states can be ruled out. On one hand, the thermal energy corresponding to a temperature of 100 mK¹² is only $E = k_B T = 8.6 \mu\text{eV}$, which is several orders of magnitude smaller than the bulk energy gap. On the other hand, a thermal excitation for the bulk states should be observable for a trivial insulator as well. QW structures with a width of 45 Å,

¹¹ $d_{QW} = 64$ Å and 73 Å have been determined by the LL crossing (see Fig. 3.4); $d_{QW} = 80$ Å is the nominal value.

¹² While the base temperature of the dilution refrigerator is below 30 mK, the effective electron temperature can be slightly larger due to, e.g., noise input.

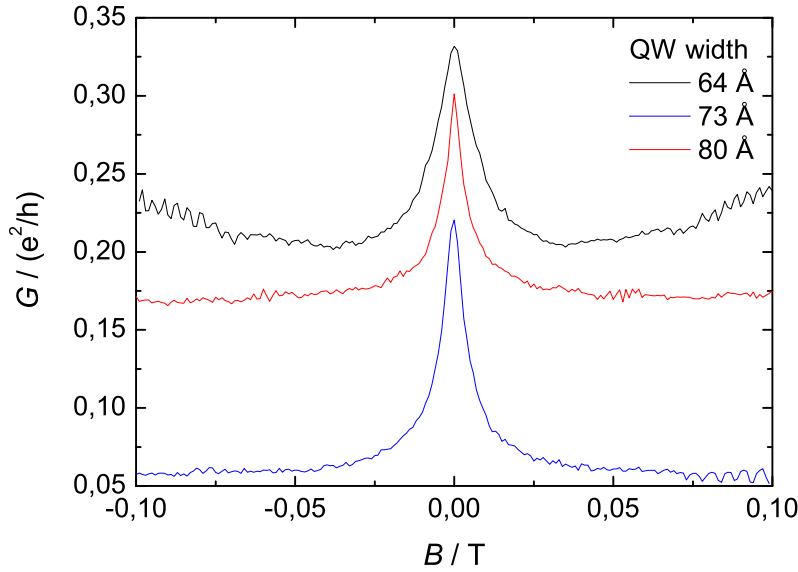


Figure 3.12: For several devices with different QW widths, the dependence of the QSH signal on a perpendicular magnetic field is shown.

73 Å and 80 Å exhibit a similar band gap (cf. Fig. 1.2), and the thermally activated conductance should be comparable for the three devices, which is obviously not the case (cf. Fig. 3.5).

For these reasons, it is evident that the residual conductance for finite magnetic field has to be related to the QSH state. As mentioned in Sec. 3.1, the states at a given edge form a Kramers pair and are consequently protected by time reversal symmetry, i.e., the edge states are robust against disorder and backscattering is not possible. But when a magnetic field is applied, time reversal symmetry is broken and the protection of the edge states is lifted. It is stated in Refs. 18 and 23 that a gap between the helical edge states opens up when time reversal symmetry is broken by a magnetic field. This description is misleading, because only the helical property of the edge states is destroyed by a magnetic field, whereas the underlying states still exist. Thus, transport through the device is still possible for finite magnetic field, albeit reduced due to the elastic scattering.

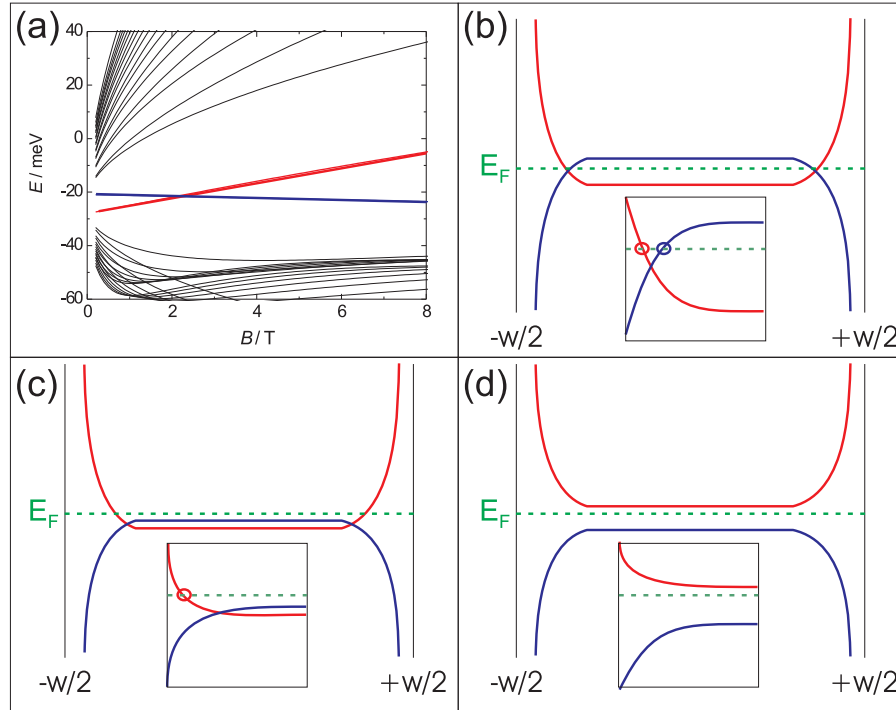


Figure 3.13: (a) The LL dispersion of a 65 Å QW was obtained by band structure calculations. In (b), (c) and (d) the dispersion of the lowest states is sketched schematically for a non-trivial insulator, a sample in the QH regime and a trivial insulator, respectively. The insets display the situation close to the sample edge and the possibly existing edge states.

The existence of the QSH edge states in magnetic field is directly connected to the re-entrant quantum Hall state presented in Sec. 2.2. It was shown that a transition to a conducting state can be observed for finite magnetic field even though the device is insulating for $B = 0$. Fig. 3.13 shows the LL dispersion of a sample with an inverted band structure (here a 65 Å QW). The QSH edge states originate from the lowest states of the valence and conduction band which are indicated in red and blue, respectively. For a small magnetic field [Fig. 3.13 (b)], the energy spectrum of these states resembles the QSH state for vanishing B -field [cf. Fig. 3.2 (b)]. However, elastic backscattering is possible due to the breaking of the time reversal symmetry.

When the magnetic field is increased, the bulk states are shifted accordingly to the Landau level dispersion. Hence, the bulk gap will close for $B = B_{\text{cross}}$ and subsequently increase again showing a reversed order of the bulk states. Depending on the exact position of the Fermi energy within the bulk gap, one of the states will cross E_F for a lower magnetic field than the other state. In Fig. 3.13 (c), the upper bulk state has already fallen below E_F , whereas the lower bulk state has not yet crossed the Fermi level. Consequently, only edge channels due to the latter state do exist. Since counter-propagating edge states are now located at opposite sides of the sample, no backscattering is possible, resulting in the observed n -type quantum Hall-like state with $R_{xx} = 0$ and $R_{xy} = h/e^2$ (cf. Sec. 2.2). When the Fermi energy is at a lower level within the bulk gap, the lower bulk state will cross E_F first, providing a p -conducting QH state (not shown here). Finally, when the magnetic field is increased further, also the second level will cross the Fermi energy and the sample will become a trivial insulator [Fig. 3.13 (d)]. The transition to the insulating regime was observed by a significant increase of the longitudinal resistance to $R_{xx} \gg h/e^2$ (see Fig. 2.9).

While the QSH states enable transport for finite magnetic field in general, scattering between these states has to be taken into account for an interpretation of the observed magneto-conductance (cf. Fig. 3.12). As shown in the previous section, the conductance for $B = 0$ is governed by scattering, if the sample length is larger than the inelastic mean free path. Thus, the deviation of the zero-field conductance $G(B = 0)$ from the expected value of $2e^2/h$ can be considered as a measure of the disorder within the device. For finite magnetic field, the samples are sensitive to elastic scattering in addition to the inelastic scattering, which is present independently of the B -field. The resulting enhancement of scattering will reduce the transmission. As $G(B = 0)$ is attributed to the disorder, the residual conductance in magnetic field is an indication for the combination of elastic and inelastic scattering processes. For $B = 0$, a small conductance of the QSH state implies a large disorder in the sample. This large disorder leads to an enhanced occurrence of elastic backscattering for finite B . Consequently, the conductance is

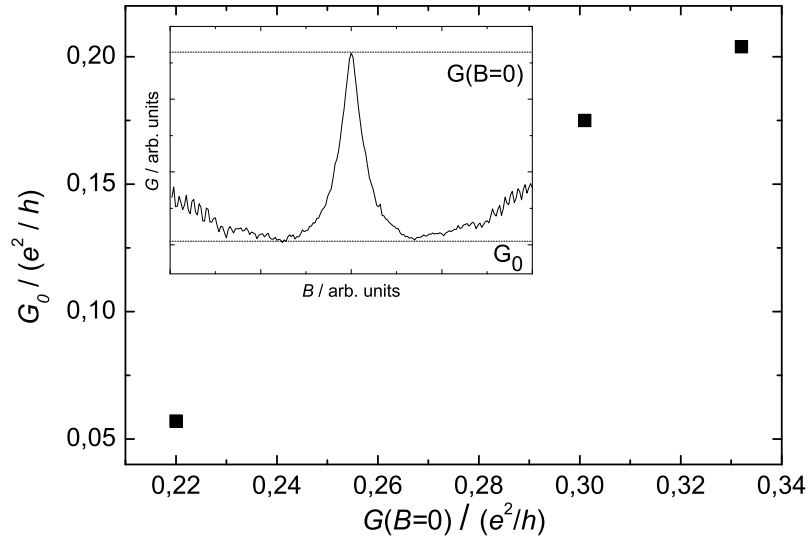


Figure 3.14: For three devices, the residual conductance G_0 for finite magnetic field is shown in dependence on $G(B = 0)$. In the inset, both values are identified using the data from the 64 Å QW.

decreased to a smaller residual value G_0 than for a sample with low disorder. This rather qualitative description is confirmed by the B -field dependent behavior of the devices presented above. As can be seen in Fig. 3.14, G_0 depends almost linearly on $G(B = 0)$. It can be inferred from the extrapolation of the values presented in Fig. 3.14 that the conductance for a finite magnetic field will be entirely destroyed, if the disorder is sufficiently large. On the other hand, a comparatively large residual conductance can be expected, when the disorder is low. A lower degree of disorder can be achieved by, e.g., reducing the sample dimensions. When the ($1 \mu\text{m} \times 1 \mu\text{m}$) device (cf. Fig. 3.7) is investigated in magnetic field, the qualitative behavior is the same as for the ($20 \mu\text{m} \times 13.3 \mu\text{m}$) Hall bars (Fig. 3.15): The conductance peak around $B = 0$ has a FWHM value of 10 mT. However, the residual conductance of around $0.7 e^2/h$ is much larger than for the bigger devices. Transmission through the device is conserved in a large part due to the comparatively weak disorder on

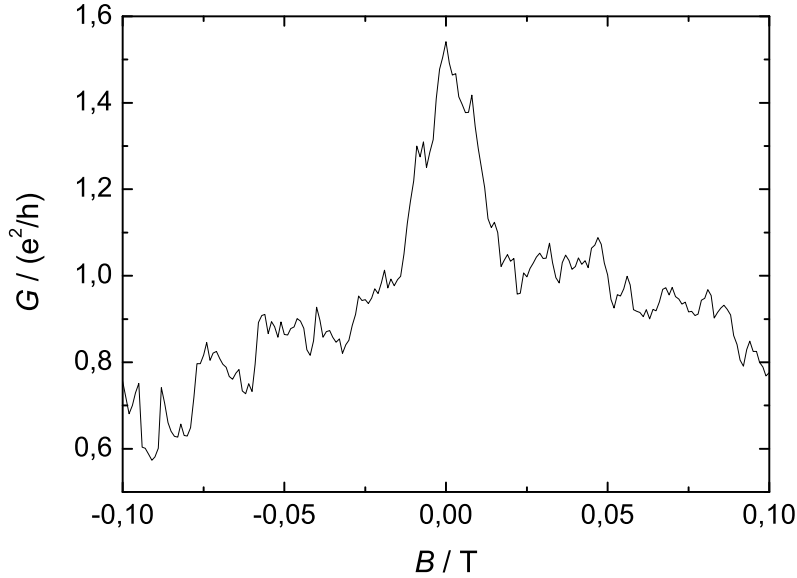


Figure 3.15: The conductance of a ($1 \mu\text{m} \times 1 \mu\text{m}$) device was measured as a function of magnetic field.

the length scale of $1 \mu\text{m}$, even though elastic backscattering is possible due to the magnetic field. Hence, the results for small devices confirm the above model.

The origin of the strong conductance fluctuations observed in magnetic field (Fig. 3.15) is not fully understood yet. One possible reason is interference due to the two parallel-propagating edge states at the opposite edges. For the larger devices, the phase coherence will be destroyed due to the increased inelastic scattering and the fluctuations vanish. Second, the actual path of the electron can also depend on the magnetic field, giving rise to a B -field dependent scattering configuration. For larger devices, the fluctuations average out.

It is evident from the above discussion that the conductance is decreased in magnetic field due to an enhanced probability of scattering. However, it is still unclear which mechanism is responsible for the destruction of the helicity of the edge states in de-

tail. Measurements were performed for an in-plane magnetic to address this issue. For the given sample mounting, the B -field was aligned in x -direction, i.e., perpendicular to the direction of the current flow. In Fig. 3.16, the magneto-conductance for an in-plane field is compared to the signal for a B -field perpendicular to the 2DEG. Both traces were obtained on the same device with a 64 Å QW. The difference in $G(B = 0)$ for the two measurements is attributed to a varying configuration

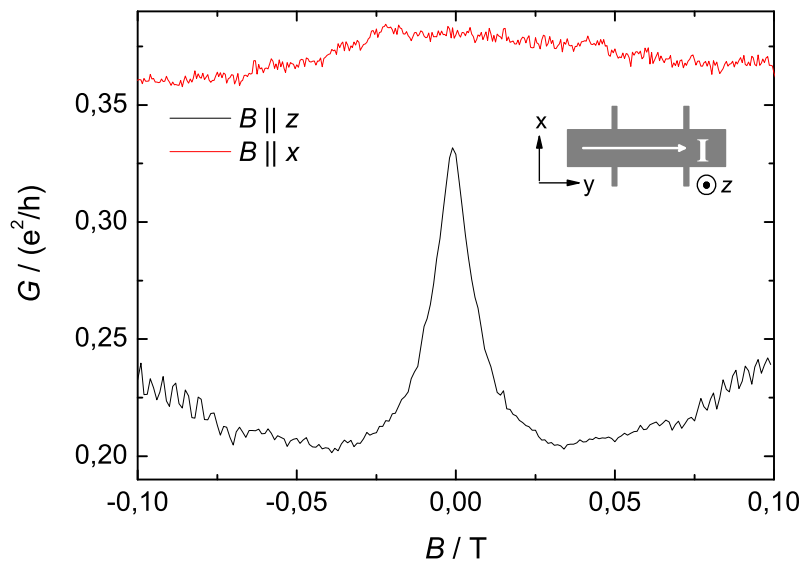


Figure 3.16: The conductance in the insulating regime is measured for a magnetic field in z -direction (black) and x -direction (red), respectively. The orientation of the field with respect to the device is illustrated in the inset.

of scatterers for both measurements¹³. In contrast to the behavior for perpendicular B -field, the conductance decreases only slightly for an in-plane field. For the investigation of this anisotropy of the conductance in magnetic field, measurements were performed using a vector magnet at 1.4 K. In such a system, the magnetic field

¹³ This is plausible, because the device had to be re-mounted due to the fixed orientation of B in the used setup. This procedure involves thermal cycling of the sample.

can be applied in any direction. This allows for a detailed study of the destruction of the helical states depending on the orientation of magnetic field. At 1.4 K, the conductance peak for a perpendicular field still exists¹⁴. Since the B -field anisotropy manifests itself in the shape of the conductance peak around $B = 0$, the residual conductance for finite B is neglected in the following and the conductance will be normalized with respect to the shape of the peak:

$$G_{\text{norm}} = \frac{G(B) - G_0}{G(B = 0) - G_0}, \quad (3.1)$$

where G_0 is the residual conductance for a perpendicular field and $G(B = 0)$ is the conductance for zero field.

A peak with a FWHM field of 28 mT is observed for a perpendicular field. The larger width compared to the peak shown in Fig. 3.16 is attributed to the enhanced temperature. When the B -field is tilted towards the 2DEG plane, the peak widens steadily. For an in-plane field, again only a slight change of the conductance is observed for the presented range (Fig. 3.17). The main contribution to the decrease of the conductance obviously stems from the perpendicular component of B . For the verification of a possible contribution by the in-plane component of the magnetic field, a simple model is applied. Assuming that the decrease of the conductance is solely due to the perpendicular component of the magnetic field, the conductance for an angle α , describing the orientation of the B -field with respect to the plane of the 2DEG, is given by

$$G_\alpha(B) = G_{90^\circ}(B_\alpha), \quad (3.2)$$

where G_α and G_{90° are the B -dependent conductance for an angle α and perpendicular field, respectively. The conversion of the magnetic field, $B_\alpha = B \cdot (\sin \alpha)^{-1}$, transforms the data obtained for $\alpha = 90^\circ$ into a trace for an angle α , assuming an effect only due to a perpendicular field. The resulting data is shown in Fig. 3.17 as squares. For angles down to $\alpha \approx 15^\circ$, the experimental data is in excellent agreement with the calculated values, whereas an increasing discrepancy appears for $\alpha \rightarrow 0$.

¹⁴ For a detailed discussion of the temperature dependence of the QSH effect, see the following section.

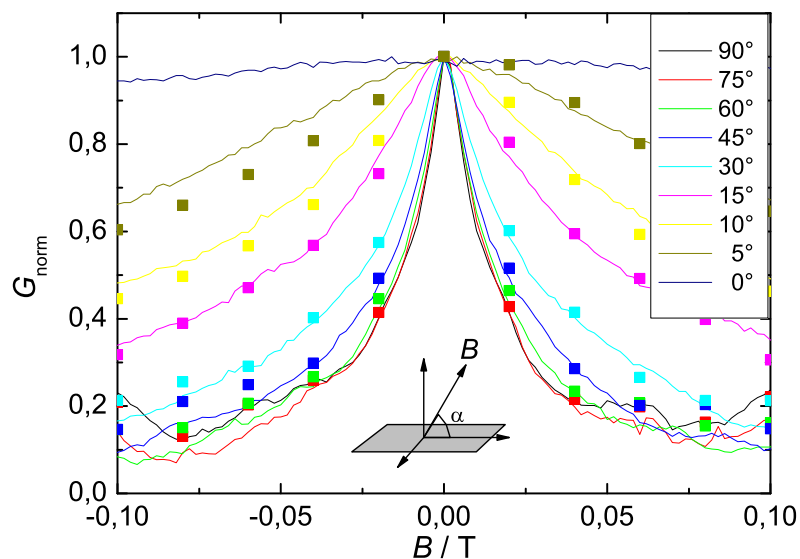


Figure 3.17: Traces of the normalized conductance is plotted for different angles α of the B -field (solid lines). The squares represent the data obtained by Eq. 3.2 for the different angles.

To rule out spurious effects due to a skew mounting of the sample, the magnetic field was rotated in the plane of the 2DEG. In Fig. 3.18 (a), the traces for a magnetic field in x - and y -direction, respectively, are presented as an example. In general, a distinct decrease of G_{norm} is observed for magnetic fields up to 300 mT independently of the exact orientation of B . In contrast to the significant decrease of G_{norm} in a perpendicular field (cf. Fig. 3.17), a decrease by only a few percent is observed for an in-plane field. Since a variation of the conductance is observed for any in-plane orientation of B , a possible tilting of the sample with respect to the plane of the B -field rotation can be neglected. When the magnetic field is rotated in the 2DEG plane, the conductance for finite B varies. As can be seen in Fig. 3.18 (b), the conductance at $B = 300$ mT shows a periodic behavior, which can be fitted by a sine curve. The oscillation period of 180° is an indication for an in-plane anisotropy of the B -dependence of the conductance.

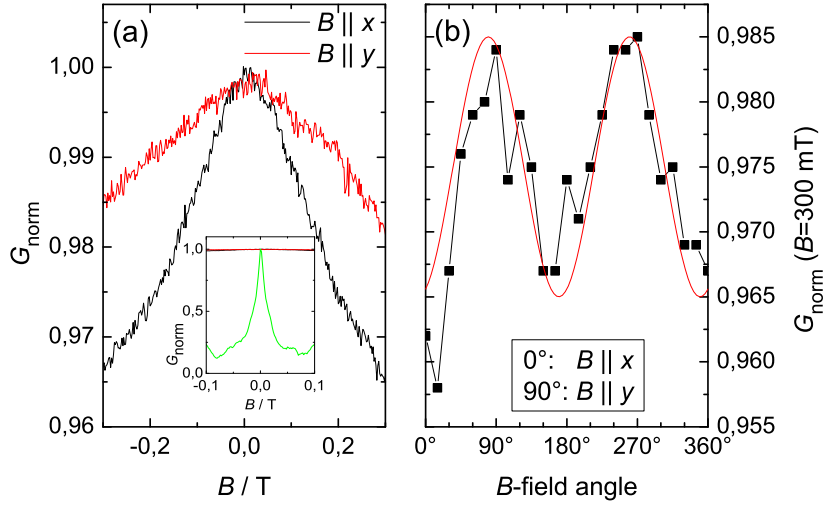


Figure 3.18: (a) The normalized conductance (cf. Eq. 3.1) for an in-plane field in x - and y -direction, respectively, is shown for B up to 300 mT. The inset shows the same traces in comparison to the measurement for $B \parallel z$ (green). (b) As a function of the rotation angle of the B -field, G_{norm} (connected black squares) can be fitted by a sine curve (red). 0° and 90° correspond to the x - and y -direction, respectively.

Based on the above results, the opening of the gap between the helical edge states can be explained. As mentioned above, the notion of an opening gap just refers to the fact that the helical character of the edge states is eliminated, while the states as such still exist but are no longer protected by time reversal symmetry against scattering. A sharp conductance peak as observed for a perpendicular field implies a large gap between the helical states. On the other hand, the conductance is preserved when no gap opens up in magnetic field. However, the latter example is unrealistic, because a Zeeman term is present for any field orientation. The corresponding energy is given by $E_Z = g\mu_B SB$, where S is the element of the Zeeman-coupling matrix. In fact, the size of E_Z depends on the direction of the magnetic field. The

observed behavior of G for an in-plane rotation of the B -field yields $E_{Z,x} > E_{Z,y}$, where $E_{Z,x}$ and $E_{Z,y}$ are the Zeeman energies for a B -field in x - and y -direction, respectively. An anisotropic Zeeman term has been reported for 1D [84] and 2D [85] GaAs hole gases. For the 1D system, the anisotropy was explained by the orientation of the magnetic field with respect to the total angular momentum J of the spin-orbit coupled holes. A much larger g-factor was observed for $B \parallel J$ than for $B \perp J$. Thus, the anisotropic nature of the conductance for an in-plane field (cf. Fig. 3.18) leads to the conclusion that the total angular momentum of the carriers in the edge states points rather in x -direction than in y -direction. However, the exact orientation of the angular momentum and the spin of the electrons in the helical edge states, respectively, can not be determined from the experimental data. For this, an analysis of the Zeeman term in a perpendicular field is required as well. However, the operator for a perpendicular field includes also an orbital term given by $\hat{z} \cdot \hat{r} \times \hat{j}|B|$. Here, \hat{r} and \hat{j} are the position and the electric current operator, respectively, and \hat{z} is the unit vector perpendicular to the 2DEG. One can estimate the magnitude of the two contributions to the gap between the helical edge states using $\langle \uparrow | \hat{z} \cdot \hat{r} \times \hat{j} | \downarrow \rangle \sim ev\xi$ and $\langle \uparrow | S | \downarrow \rangle \sim 1$. Here, v is the Fermi velocity and ξ the width of the edge states. Both quantities can be obtained from the parameters of the Dirac model as $v \approx A/\hbar$ and $\xi \approx \hbar v/|M|$. Taking realistic values for A and M [86], it can be shown that the gap for the helical edge states due to the orbital term in a perpendicular field is approximately two orders of magnitude larger than the Zeeman-related gap. From this estimation it is obvious that the orbital effect is the dominant mechanism for the destruction of the helical edge states, which gives rise to the observed sharp decrease of the conductance in a perpendicular field. However, the Zeeman term becomes important for small angles of the magnetic field due to the vanishing orbital term.

In conclusion, the helical property of edge states is destroyed when the time reversal symmetry is broken due to a magnetic field. A gap between the helical edge states opens up due to the Zeeman term, which is present for any field direction.

This contribution is anisotropic in magnetic field. For a B -field perpendicular to the 2DEG, the dominant mechanism for the opening of the gap is caused by an orbital effect. In this context, the notion of a gap only describes the destruction of the helical property, while the underlying states still exist in magnetic field. Thus, transport is still possible, but is decreased due to scattering. Since the strength of both the orbital and the Zeeman term depend on the orientation of the magnetic field, an anisotropy of the conductance is observed for finite B .

3.4 Temperature dependence of the QSH effect

In the previous sections, results obtained at temperatures up to 4.2 K were used for the analysis of the QSH effect. These experiments show that the QSH effect still exists at elevated temperatures. In this section, the temperature-dependence will be investigated in a more detailed way.

For small samples, e.g., with $L = 1\mu\text{m}$, scattering can be neglected and the temperature dependence of the undisturbed QSH states can be studied. Measurements at 30 mK and 4.2 K, respectively, were presented in Fig. 3.8. The main difference between the two traces are the conductance fluctuations, which exist only at low temperature. These fluctuations are attributed to interference effects at the interface between the QSH region and the n -doped contacts and not to the QSH states as such. When the fluctuations are neglected, the conductance stays almost constant, while the temperature is increased by two orders of magnitude. Thus, an increase of the temperature leaves the QSH states almost unaffected.

In contrast, a clear temperature dependence of the conductance can be observed for larger samples. Fig. 3.19 (a) shows the conductance for $B = 0$ for temperatures up to 1 K¹⁵. The measurements were done on a ($20.0\ \mu\text{m} \times 13.3\ \mu\text{m}$) Hall bar from a

¹⁵ These measurements were done without intermediate thermal cycling of the device. All other measurements for $T \geq 1$ K were done in different thermal cycles and, thus, only allow for a qualitative comparison due to the possibly different scattering configuration for each cool-down.

64 Å QW. Results from this device were already presented in the previous sections, e.g., in Figs. 3.12, 3.16 and 3.17. For all measurements, the same gate voltage close to the center of the QSH regime was applied, i.e., the Fermi level is located approximately in the center of the bulk gap. When the temperature is below 100 mK,

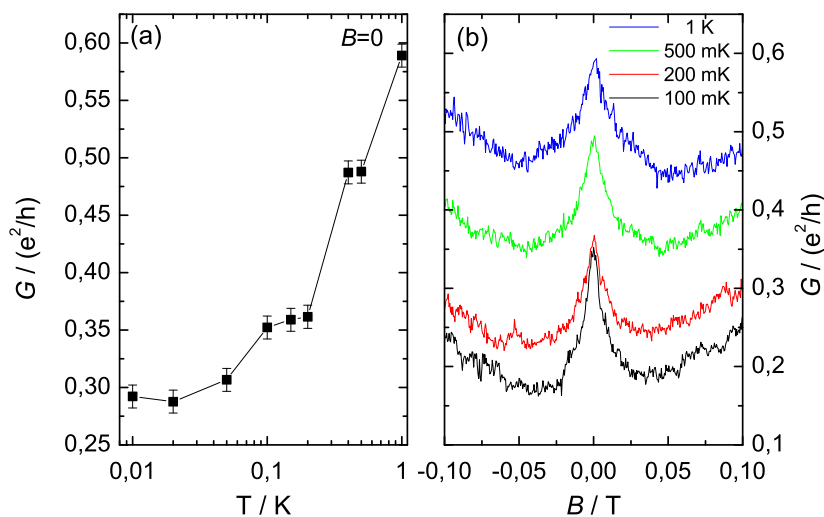


Figure 3.19: (a) The conductance for $B = 0$ is shown as a function of the temperature. The data points were extracted from B -field dependent measurements. The traces for temperatures of 100 mK, 200 mK, 500 mK and 1 K are presented in (b).

the conductance is almost constant at $0.3 e^2/h$. For higher temperatures, G rises significantly up to $G \approx 0.6 e^2/h$ for $T = 1$ K. It can be inferred from this behavior that the effective electron temperature is about 100 mK, while lower nominal values only describe the temperature of the sample lattice. Another possible explanation for the constant conductance at low temperatures will be given below. The difference between the temperature of the lattice and the electrons can be explained by the lack of phonons for such low temperatures. Thus, energy transfer from the electrons to the lattice is not possible and the effective electron temperature can be larger than the temperature of the lattice. The heating of the electrons is caused

by the input of noise in the measurement setup. A second possible reason is the excitation voltage U_{exc} of $10 \mu\text{V}$ used for the measurements, which corresponds to $T \approx e \cdot U_{\text{exc}} / k_B = 116 \text{ mK}$. Lowering the excitation voltage did not change the shape of the conductance peak, but decreases the signal-to-noise ratio. Hence, the effective electron temperature is limited by the electrical noise and the excitation voltage of $10 \mu\text{V}$ does not yield a further heating of the electron gas.

Fig. 3.19 (b) shows the B -dependent conductance for temperatures of 100 mK, 200 mK, 500 mK and 1 K, respectively. The increase of the conductance with temperature is independent of the magnetic field strength. One possible explanation is a thermal activation of carriers. Based on the results for short samples, the conductance of undisturbed QSH edge states is supposed to yield a constant contribution G_{QSH} for all temperatures. Hence, the total conductance can be described by

$$G_{\text{total}}(T) = G_{\text{QSH}} + G_{\text{th}}(T), \quad (3.3)$$

where G_{th} is the thermally activated conductance. Furthermore, it is assumed that $G_{\text{th}}(T < 100 \text{ mK}) \ll G_{\text{QSH}}$, which is reasonable due to $E_g \gg k_B T$. Including this estimation, the thermally activated conductance for a temperature T is given by

$$G_{\text{th}}(T) \approx G_{\text{total}}(T) - G_{\text{total}}(T = 10 \text{ mK}). \quad (3.4)$$

For a thermal excitation of carriers over an energy gap, e.g., from the bulk valence band to the conduction band, an increase of conductance according to

$$G_{\text{th}}(T) \sim \exp\left(-\frac{\Delta E}{k_B T}\right) \quad (3.5)$$

is expected. Here, ΔE is the energy gap. When the increase of G_{th} is fitted by Eq. 3.5, an energy gap of approximately $20 \mu\text{eV}$ is obtained. This value is two orders of magnitude smaller than the bulk gap for the 64 \AA QW (cf. Fig. 3.4), which makes thermal excitation of carriers in the bulk impossible [Fig. 3.20 (a)]. Since the Fermi level is intentionally tuned to the center of the energy gap, an excitation from the edge states to energetically remote states of the conduction band and valence band, respectively, is also not possible [Fig. 3.20 (b)]. Close to the crossing

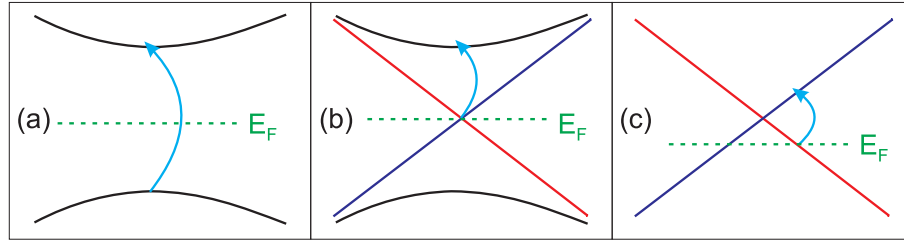


Figure 3.20: Thermal excitation of carriers may occur (a) in the bulk from the valence band to the conduction band, (b) close to the edge from the QSH states to the conduction band and (c) between the edge states for sufficiently large temperatures.

point of the QSH states [Fig. 3.20 (c)], the separation of the states for opposite spin polarization can be as low as $20 \mu\text{eV}$. However, the QSH states are not absolutely sharp in energy, but have a finite width of a few meV [83]. Consequently, there is actually no gap between the states for opposite spins close to the crossing point and a thermal excitation of carriers between two QSH states can be ruled out as well. In general, the contribution of thermally activated carriers to the transport can be neglected at such low temperatures.

The increase of the conductance has rather to be related to an enhanced transmission of the QSH edge states. This implies a decrease of scattering between counter-propagating edge channels. Since the increase of G with T is observable for $B = 0$, inelastic scattering and direct interaction of the edge states due to local conducting regions have to be considered. Inelastic scattering is expected to increase with temperature [87]. Therefore, it can not be responsible for the observed increase of conductance. The temperature-dependence of the conductance can be understood when an equilibration of counter-propagating edge states due to local n -type regions¹⁶ is considered. As it was shown in Sec. 3.2, the conduction band (CB)

¹⁶ While the explanation is limited to n -type regions for simplicity, a corresponding effect is expected for p -type regions as well.

minimum can be shifted below the Fermi energy, e.g., due to potential fluctuations, and n -doped regions will appear within the QSH regime. A possible configuration of a sample is shown in Fig. 3.21 (a). On each edge, one n -type region enables backscattering. Thus, the conductance for $B = 0$ deviates from the quantized value of $G = 2e^2/h$, which is obviously the case for all temperatures shown in Fig. 3.19. The influence of the potential fluctuations on the conduction band (CB) minimum is sketched in Fig. 3.21 (b) and (c). For large parts of the device, the Fermi level

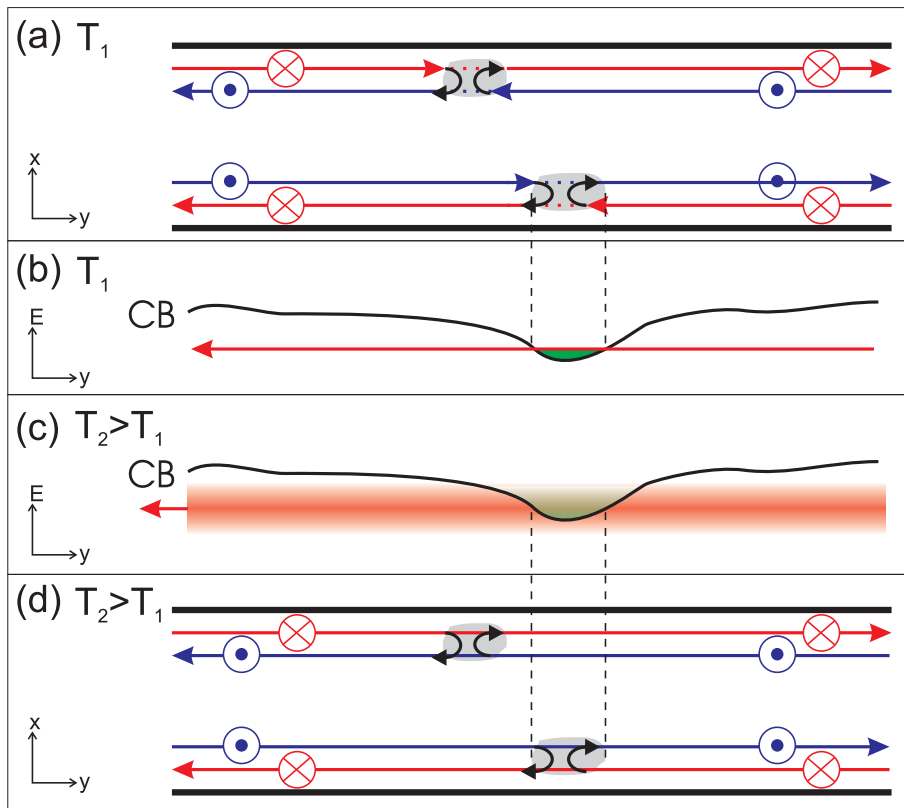


Figure 3.21: (a) n -type regions close to the sample edge give rise to backscattering of the edge states. (b) The energy of the edge state is indicated by a red line corresponding to (a). Since the energy distribution is defined sharply, all electrons in the edge state enter the n -region (green). (c) For $T_2 > T_1$, the energy distribution is widened even to regions within the gap. (d) n -regions and QSH edge states can locally co-exist for elevated temperatures.

is in the band gap, making only QSH states available. However, an n -type region appears, if the CB minimum is shifted below the Fermi energy. For finite temperatures, the energy levels broaden and states within a range of $k_B T$ around the Fermi energy can be occupied as well. It is obvious that the thermal broadening can be neglected for low temperatures and only energy states exactly at the Fermi level have to be considered for transport. The channels will enter each n -doped region which provides states at E_F [see Fig. 3.21 (b)] and counter-propagating edge states inevitably equilibrate. For increasing temperature, the thermal broadening becomes comparable to the size of the potential fluctuations [Fig. 3.21 (c)] and QSH states in the energy are available as well. This results in a co-existence of n -conduction and transport for the corresponding region of the device [Fig. 3.21 (d)]. Electrons in these QSH states will not enter the n -region. Consequently, they can not be backscattered, yielding an increase of conductance. For increasing temperature, more QSH states become available and backscattering is further reduced. This picture can also provide an explanation for the temperature-independent conductance for $T < 100$ mK. For such low temperatures, the thermal broadening of the levels is not sufficient to populate QSH edge states in the vicinity of the n -regions. Thus, all electrons equilibrate with electrons from the respective counter-propagating channel. For $T > 100$ mK, however, the conductance rises steadily with temperature due to the increasing availability of QSH states. The latter can be demonstrated on the basis of the $E(k)$ dispersion sketched in Fig. 3.22. When the Fermi level is above the CB minimum, n -conductance occurs. Although coexistent QSH states (cf. Fig. 3.11) contribute to the conductance as well to some extent, they will not be considered here, because the n -conductance of the bulk is the dominant transport mechanism. The broadening of the energy states can be neglected for a low temperature T_1 [Fig. 3.22 (a)]. When the temperature is increased to $T_2 > T_1$, the QSH states below the CB minimum become available due to the thermal broadening of the Fermi level [Fig. 3.22 (b)].

The obtained energy gap of some few $10 \mu\text{eV}$ for the thermal activation is reasonable for this mechanism as well. Even if the local conduction band minimum

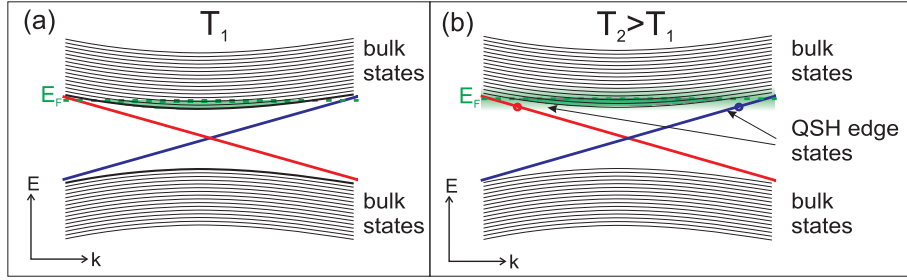


Figure 3.22: The $E(k)$ -dispersion of bulk states (black solid lines) and edge states (red and blue, respectively) is sketched schematically. (a) For low temperatures, the Fermi level (green dashed line) is limited to the conduction band. (b) For higher temperatures, QSH edge states can be occupied due to thermal excitation of the carriers.

is just slightly below the Fermi level an n -type region appears and gives rise to backscattering due to the existence of an n -type region. Then, small thermal excitation energies are sufficient to allow the electrons to occupy QSH states in the gap. This is obvious in Fig. 3.22 from the small separation in energy of the bulk states and the edge states, in particular for finite k .

As can be seen in Fig. 3.19 (b), the peak height, i.e., $G(B = 0, T) - G_0(T)$, is almost constant for increasing temperature. This is an indication that the temperature-dependence of the conductance is mainly attributed to the increased availability of QSH states as described above. In comparison, the temperature-dependence of the elastic scattering in finite magnetic field can be neglected.

In conclusion, the temperature dependence of the QSH effect was investigated. Here, one has to distinguish between two regimes. On the one hand, the QSH states as such are stable against an increase of temperature up to 4.2 K. This was shown by measurements on small devices ($L = 1 \mu\text{m}$), where scattering can be neglected. On the other hand, a clear temperature dependence of the conductance was observed, when scattering was present due to a larger size of the devices. In such samples,

the conductance rises with temperature. Since inelastic scattering would lead to a contrary effect, only local conducting regions within the QSH regime can be responsible for the observed behavior. At low temperatures, a local conducting region inevitably leads to an equilibration of counter-propagating edge states. The broadening of the Fermi energy for increased temperatures makes QSH states available, which are located at energies slightly below the local CB minimum. Thus, electrons in the can avoid the conducting regions and backscattering is reduced. It can be deduced from the temperature dependence of scattering that local conducting regions are the dominant mechanism for backscattering at $B = 0$, whereas inelastic scattering of the QSH edge states plays only a minor role.

3.5 Summary

The measurements presented in this chapter provide the first experimental observation of the Quantum Spin Hall effect. The existence of this novel topological phase was predicted for HgTe QW structures with an inverted band structure, i.e., $d_{QW} > 63 \text{ \AA}$. When the Fermi energy is located in the energy gap for the bulk, edge states can carry both a charge and a spin current without dissipation. These states exist due to the inverted band structure, which causes a crossing of the lowest states from conduction and valence band, respectively, close to the sample edge.

Despite the fact that the transport occurs solely due to edge states, in which backscattering is prohibited by time reversal symmetry, the longitudinal resistance of the QSH regime does not vanish in contrast to the initial theoretical prediction. The main reason are the n -doped contacts, where the electrons from counter-propagating edge states get equilibrated. Thus, backscattering can give rise to a finite resistance. Considering the influence of the contacts, a four-terminal conductance of $2e^2/h$ is expected. When the sample length is comparable to the mean free path, i.e., $L = 1 \mu\text{m}$, scattering can be neglected and the four-terminal resistance is close to the quantized value. For larger devices, the conductance is reduced due to scattering between the counter-propagating states, which can be attributed to inelastic processes and the

existence of local conducting islands within the QSH region. Edge state transport for the QSH regime was verified in two distinct ways. On the one hand, a variation of the sample width did not affect the resistance of the QSH state. On the other hand, a clear non-local signal was detected in the insulating regime.

When time reversal symmetry is broken by a magnetic field, elastic scattering becomes possible and the conductance of the edge states is reduced. The basic existence of the edge states in magnetic field is reflected in the re-entrant quantum Hall state described in Sec. 2.2. The dominant mechanism for the suppression of conductance is attributed to an orbital effect only present in a perpendicular field. In addition, a significantly smaller Zeeman term exists for all field directions. The combination of these two contributions is reflected in an anisotropy of the B -dependence of the conductance.

The pure QSH edge states do not show any temperature-dependence up to 4.2 K. However, scattering due to local conducting regions is reduced for increasing temperature, because the electrons can occupy edge states at energies below the CB minimum and above the VB maximum, respectively. This results in an increase of conductance with temperature in large samples.

Altogether, various aspects of the QSH effect were demonstrated in our experiments. However, the exact conductance quantization could not be shown yet and remains a goal of future investigations. For this purpose, the scattering of the edge states has to be minimized. This can happen by downsizing the devices to length scales well below $1 \mu\text{m}$. In addition, a maximum size of the energy gap, i.e., $d_{QW} = 85 \text{ \AA}$, may make the potential fluctuation negligible. Detailed measurements on samples free of disorder can also yield a better understanding of the B -field dependence of the QSH effect. The stability of the QSH states for increasing temperature may be utilized for possible applications. Neglecting the explicit temperature-dependence of transport in the QSH states, e.g., due to thermally activated interaction of counter-propagating channels, the QSH conductance can be expected to be observable up to high temperatures. Precisely, the QSH states for ideal samples without disorder

will be stable as long bulk states can not be occupied due to thermal activation. In principle, this can be avoided for $T < E_G/(2k_B)$, if the Fermi energy is exactly in the center of the energy gap. Thus, the QSH effect for an 85 Å QW with $E_g \approx 40$ meV should exist up to $T \approx 230$ K.

A second issue possibly addressed in future experiments covers the spin transport properties of the edge channels. Investigations in this field require spin-selective injection and detection of the carriers in the edge channels, which is an unsolved task so far for HgTe QW devices.

Chapter 4

Spin Hall Effects in doped HgTe QWs

Already in 1971, Dyakonov and Perel predicted a spin imbalance transverse to the current in a semiconductor. In their model, the spin accumulation at the sample edges occurs due to spin-dependent scattering [88]. However, their proposal aroused no further interest and remained almost unnoticed for several decades. Recently, possible applications in the field of spintronics renewed the interest in spin-related phenomena. In 1999, Hirsch proposed the existence of a spin Hall effect [11]. This effect is now known as the extrinsic spin Hall effect, since it is based on scattering similar to the proposal by Dyakonov and Perel. Sinova *et al.* showed that an intrinsic spin Hall effect purely based on the spin-orbit interaction also exists [13]. Due to the inverse spin Hall effect (SHE^{-1}), which can be seen as a complementary effect to the spin Hall effect, a spin current can yield a transverse charge imbalance [89,90].

The spin accumulation due to both extrinsic and intrinsic SHE has been detected for semiconductor materials by means of optical methods [24–26], while no observation by an electrical measurement was achieved so far. The existence of the SHE^{-1} in metals has been inferred from a transverse charge imbalance, when a spin current was injected from a ferromagnetic contact [27–29]. However, a detection in a semiconductor was not reported yet.

Hankiewicz *et al.* proposed an H-shaped device based on a 2DEG with spin-orbit interaction, which can provide evidence of both the SHE and the SHE⁻¹ [30]. In one leg of the device, a charge current is driven and the spin Hall effect is responsible for the generation of a transverse spin current. This, in turn, will yield a non-local charge signal in the other leg due to the inverse spin Hall effect. Thus, the existence of both effects can be shown simultaneously within a single device. Since the Rashba splitting in HgTe quantum wells is much larger than for other semiconductor materials and, additionally, can be tuned over a wide range, devices based on this peculiar material are a good candidate for the investigation of spin-orbit related effects in general and of intrinsic spin Hall effects in particular. In this chapter, results from purely electrical measurements on H-shaped devices are presented, providing evidence for the existence of both the spin Hall effect and the inverse spin Hall effect in HgTe QW structures.

This chapter also contains experimental results, which were obtained from similar samples prior to the work on this thesis and not understood at that time. However, an interpretation is possible now, when the QSH effect is taken into account. The spin-polarized transport in the QSH edge states can be used for an injection and a detection of a spin-imbalance, respectively. Thus, the SHE and the SHE⁻¹ can be demonstrated independently.

4.1 Theory of Spin Hall Effects

A lot of efforts were made to explain the spin Hall effect in the recent years due to the renewed interest in spin-related phenomena based on the potential applications in spintronic devices. It was shown that a variety of mechanisms can yield a spin accumulation at the sample edges¹. The mechanism proposed by Hirsch [11] is today known as the extrinsic spin Hall effect. The description as extrinsic refers to the fact that the asymmetric accumulation of spins relies on impurities within the sample. These impurities can result in a spin accumulation for various reasons. One contribution is a skew scattering, also known as Mott scattering [92], of the spin-carrying electrons. In this case, the extrinsic SO interaction gives rise to an unequal scattering cross section for the two spin states. This explanation is similar to the reasoning by Dyakonov and Perel [88,93]. Another possibility is based on so-called side jumps [94]. Here, the SO interaction produces a lateral displacement of the electron wave function during a scattering event. Both mechanisms are reflected in a spin-dependent preferential direction of scattering, which causes a spin accumulation at the sample edges. Without distinguishing between the mechanisms mentioned above, the extrinsic SHE can be explained analogous to the anomalous Hall effect (AHE). In general, every mechanism that leads to a Hall voltage, but is not solely caused by an external magnetic field, is called an anomalous Hall effect. On the one hand, magnetic impurities can create an additional internal magnetic field. However, this contribution to the Hall voltage vanishes with the external magnetic field unless the impurities are ferromagnetic. On the other hand, spin-dependent scattering can also yield an anomalous Hall voltage. This mechanism is not based on an external magnetic field, but on a net magnetization of the electron system, which is reflected in an unequal number of up- and down-spins. Thus, a spin-dependent asymmetric scattering results in a charge imbalance and the anomalous Hall voltage can be observed in a direction perpendicular to the current. The latter mechanism can induce a pure spin Hall effect, if a non-magnetic material is considered. Since the

¹ A comprehensive overview can be found in Ref. 91

scattering mechanisms, which establish the AHE, do not rely on the magnetization, electrons with spin up and spin down, respectively, will be preferentially scattered into opposite directions and a spin imbalance will appear: at one edge the majority of electrons will have spin up, while it will be spin down for the opposite edge. Unlike the AHE, no charge imbalance will appear, since spin-up states and spin-down states are equally occupied. Consequently, a pure spin Hall effect will be obtained.

But scattering is not necessarily required to obtain a spin Hall effect. Recently, the existence of an intrinsic SHE has been proposed for p -doped bulk semiconductors [12], a two-dimensional electron gas [13] and a two-dimensional hole gas [95], respectively. For the 2D systems, the SHE stems from a substantial Rashba splitting. The corresponding electric field in z -direction, i.e., perpendicular to the 2DEG, gives rise to a momentum-dependent effective magnetic field:

$$\vec{B}_{\text{eff}} \sim \vec{p} \times \vec{E}, \quad (4.1)$$

where \vec{p} is the electron momentum and \vec{E} the electric field. It is obvious that \vec{B}_{eff} is localized in the xy -plane, when only the Rashba field in z -direction is present. The spins of the electrons are aligned with B_{eff} , i.e., perpendicular to both the electric field and the momentum [Fig. 4.1 (a)]. When an external electric field is applied to drive a current, e.g., in x -direction, the electrons will be accelerated and the effective magnetic field will be changed. B_{eff} will acquire an additional z -component and the spins consequently will be tilted out of the 2DEG plane. The orientation of B_{eff} with respect to the z -axis is determined by the sign of the y -component p_y of the electron momentum, i.e., the direction of movement perpendicular to the current determines the spin orientation. The z -component of the spin direction is given by [13]

$$n_z = \frac{-e\hbar^2 p_y E_x}{2\alpha p^3}, \quad (4.2)$$

where α is the spin-orbit constant². It is obvious from the linear dependence of the n_z on the y -component of the electron movement that left-moving electrons will

² While the Rashba parameter is called λ in Ref. [13], the notation as α is used consistently throughout the thesis.

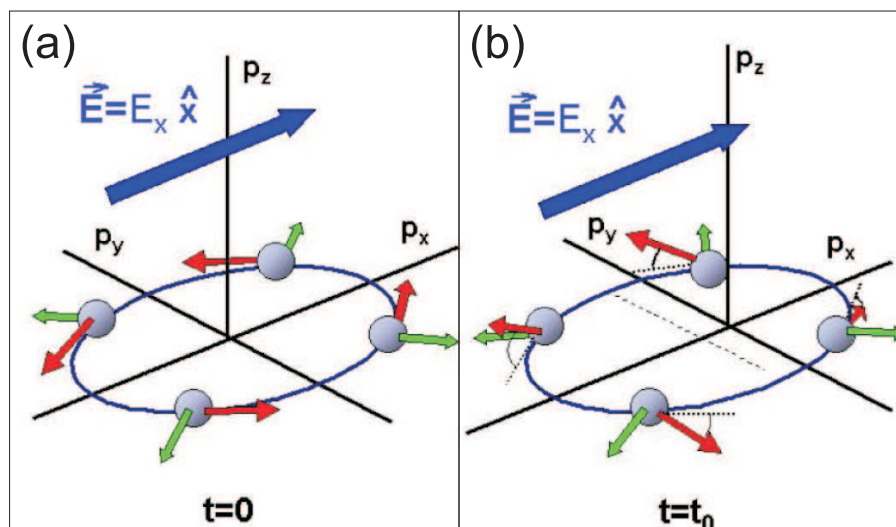


Figure 4.1: The electron spins (red arrows) align with the effective magnetic field, which is determined by the momentum (green arrows) and the total electric field. (a) For $t = 0$ the situation is equivalent to an absence of the electric field in x -direction. (b) For $t > 0$, the Fermi surface is shifted due to the electric field and the electron spins are tilted out of the xy -plane. (from Ref. 13)

be spin-up and all right-moving ones spin-down [cf. Fig. 4.1 (b)]. The resulting accumulation of spin-polarized electrons at the sample edge is the intrinsic spin Hall effect.

A direct observation of spin Hall effects by means of purely electrical measurements is not possible. Even though a spin imbalance is achieved at the sample edges, no charge imbalance is expected, since both spin states are equally occupied. For the experimental verification of the spin Hall effect, two basically different approaches have been chosen. On the one hand, the spin accumulation at the sample edges can be detected by means of optical methods. The first observation of the SHE was reported by Kato *et al.* who used the Kerr rotation to demonstrate opposite spin polarization for the two sample edges of n -doped GaAs and InGaAs, respectively [24]. It is generally believed [96] that the spin accumulation is based on the extrinsic

SHE in this case. Using the same method, the extrinsic SHE was also observed for a 2DEG in AlGaAs quantum wells [26]. Wunderlich *et al.* [25] detected an opposite spin polarization at the edges of a 2D hole layer using a light-emitting diode, which includes a spin-orbit coupled 2D hole system. Subsequent calculations [95] showed that the intrinsic SHE was observed.

A second possibility for the experimental observation of the SHE is based on the so-called inverse spin Hall effect (SHE⁻¹). In this case, a spin current gives rise to a transverse charge imbalance, which can be detected by electrical measurements. Hirsch proposed a device based on the extrinsic SHE⁻¹ for the detection of the spin Hall effect [11]. An intrinsic SHE⁻¹ can be caused by a spin force due to the spin-orbit coupling [89, 90]. Thus, the generation of a spin current by the SHE can be demonstrated indirectly by the detection of the voltage due to the inverse spin Hall effect. The first experimental observation of the SHE⁻¹ was obtained, when a spin current was injected from a ferromagnetic electrode (CoFe) into an Al Hall cross [28]. The voltage difference for the transverse probes in the Hall cross depends on the polarization of the injected spin current which is a clear indication of the SHE⁻¹. The inverse SHE was shown to exist up to room temperature in metals [27, 29]. Kimura *et al.* were also able to measure a voltage signal which was attributed to the "normal" SHE at room temperature [29]. In all these experiments the spin current was injected from a ferromagnetic metal contact. So far, an observation of the SHE⁻¹ has not been reported for semiconductor systems. In addition, the generation of a spin current by the SHE has not been shown yet as well.

Hankiewicz *et al.* proposed a device, in which the spin Hall effect and the inverse spin Hall effect can be detected simultaneously by a purely electrical measurement [30]. Fig. 4.2 shows the suggested H-shaped structure. One leg is used to drive a current (injector), while the contacts in the other leg (detector) are used as voltage probes. When pure charge transport is considered, no voltage difference between the remote probes is expected due to the non-local measurement configuration. However, the spin Hall effect will generate a finite voltage drop. Descriptively, V_{34} is built up in

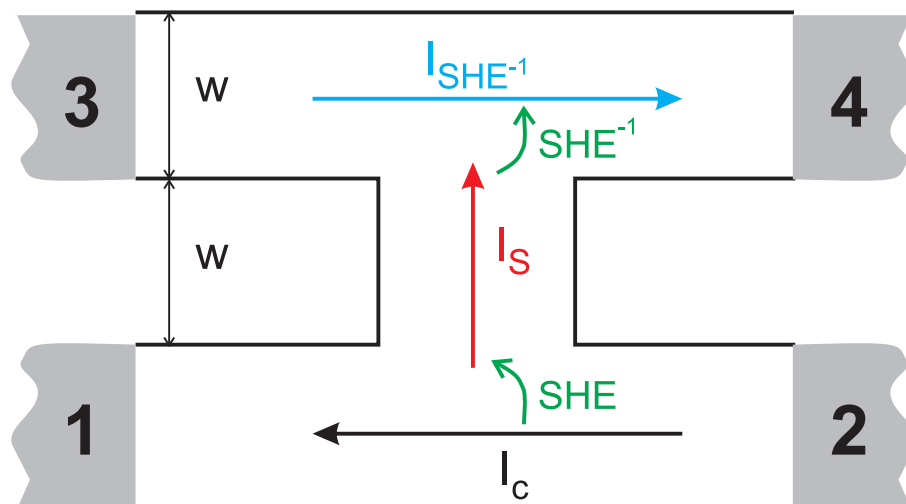


Figure 4.2: In the H-shaped structure proposed by Hankiewicz *et al.* [30], the current is injected from contact 1 to 2, and a voltage difference is detected between contacts 3 and 4.

the following way: When a charge current I_C is driven between contacts 1 and 2, the spin-orbit interaction gives rise to a transverse spin current due to the intrinsic spin Hall effect. The movement of the electrons perpendicular to the current direction is restricted by the sample edges in the leads and a spin accumulation occurs as experimentally demonstrated in Ref. 24. In the center part of the device, however, the spin current I_S can reach the other leg. This spin current generates a transverse charge current due to the inverse spin Hall effect and a voltage difference between contacts 3 and 4 can be detected. The amplitude of V_{34} depends on the strength of the SO interaction since both the SHE and the SHE^{-1} are tuned by Δ_R in the device.

An effective mass model using a tight binding approximation was applied to calculate V_{34} . Using realistic parameters, voltages of some few μV were obtained at large Rashba splitting for an injected current of 10 nA. It was shown that the voltage signal depends strongly on the size of the device. For example, V_{34} decreases approximately from $8\mu V$ to $2\mu V$, when the width w is increased from 15 nm to 20 nm, while all other parameters are constant. Nevertheless, the existence of both

intrinsic SHE and SHE^{-1} can be demonstrated in principle by the detection of a Rashba-dependent voltage drop V_{34} .

In conclusion, a variety of mechanisms can yield a spin imbalance perpendicular to a charge current. While the extrinsic spin Hall effect requires a spin-dependent scattering analogous to the anomalous Hall effect, the intrinsic SHE relies purely on the spin-orbit interaction in the system. The mechanisms establishing the spin Hall effect can also be reversed, i.e., a spin current generates a transverse charge current. The latter effect is called the inverse SHE. So far, both extrinsic and intrinsic SHE have been observed using optical methods and the SHE^{-1} was found for metals by means of electrical measurements. To demonstrate the existence of SHE and SHE^{-1} for semiconductors by purely electrical measurements, an H-shaped device was proposed. Here, the SHE causes a transverse spin current which results in a charge current in the detector leg.

4.2 Experimental investigation of the Spin Hall Effect

Even though the intrinsic spin Hall effect has been successfully demonstrated for semiconductors by optical means [25], there has been no experimental observation by electrical measurements in such systems so far. A second, so far unsolved task is providing an evidence of the inverse spin Hall effect in semiconductors. Both aims can be achieved using an H-shaped device as it was proposed by Hankiewicz *et al.* [30], where the existence of the spin Hall effect and the inverse spin Hall effect can be shown simultaneously. HgTe quantum well structures are an appropriate material for the fabrication of such H-devices. On the one hand, high mobility samples [63] with a substantial Rashba splitting [21,22] are available. Thus, the intrinsic SHE is supposed to be the dominant mechanism for the generation of spin currents. Additionally, the Rashba splitting can be tuned over a wide range. This results in a

modulation of the strength of the SHE and, consequently, in a significant variation of the non-local signal. On the other hand, recent developments in the lithography allow for the fabrication of nanostructures (cf. Sec. 1.3) which are required for the detection of the spin Hall effect. A width w of the legs not exceeding 20 nm was used for the proposal in Ref. 30. This size is approximately one order of magnitude smaller than the feasible dimensions for HgTe nanostructures. In the theoretical calculations, the non-local voltage shows an oscillatory behavior as a function of the sample size. In general, however, the signal tends to decrease for an increasing sample size [97]. Then again, the non-local voltage drop V_{34} will increase by at least one order of magnitude, when a Rashba term proportional to k^3 is considered instead of the splitting linear in k [97]. Altogether, the enhanced spin Hall effect for both n - and p -conductance might compensate the diminishment of the signal due to the larger size of the device. For the devices presented in this section, the legs have a nominal width of 200 nm, which is also the length of the connection between injector and detector. Due to inaccuracies in the lithographical process, e.g., caused by an unintentional overexposure of the PMMA, the actual width might be slightly larger³. All measurements were done in a ⁴He cryostat at a temperature of 1.8 K and 4.2 K, respectively, using standard AC lock-in techniques. In our experiments, the non-local resistance $R_{12,34} = V_{34}/I_{12}$ is considered. In this way, the results from different devices can be compared quantitatively. It is justified to analyze the resistance instead of the non-local voltage, because the model by Hankiewicz *et al.* works in linear response, i.e., the non-local voltage is proportional to the injected current [98]. This relation holds as long as the excitation energy of the electrons is much smaller than the Fermi energy, i.e., $eU_{\text{exc}} \ll E_F$.

³ Since taking a picture with a scanning electron microscope usually affects the samples, e.g., due to a charging of the 2DEG, the exact dimensions of the investigated devices were not determined. However, $w \leq 250$ nm was measured for one non-working device at an early stage of the experiments. This size can be seen as an upper limit, because the lithographical parameters were adjusted afterwards.

A device was fabricated from an 80 Å QW with an intrinsic electron density $n(V_g = 0) = 1.3 \cdot 10^{12} \text{ cm}^{-2}$ and a mobility of $3.38 \cdot 10^5 \text{ cm}^2(\text{Vs})^{-1}$. Only one of the QW barriers was doped to induce a large Rashba splitting due to the intrinsic asymmetry of the QW potential. Such a sample meets the demands for the existence of the intrinsic spin Hall effect given in Refs. 13 and 30. In a Hall bar fabricated from the same QW structure, the Rashba splitting was tuned continuously from zero for $V_g = -2.0 \text{ V}$ to approximately 12 meV for $V_g = +2.0 \text{ V}$. While a direct analysis of the Rashba splitting was not possible for the H-device, the dependence of the resistivity on the gate voltage is comparable for both devices. Thus, the variation of Δ_R should be similar as well, i.e., the QW potential is symmetric for $V_g \approx -2.0 \text{ V}$ and becomes increasingly asymmetric for larger gate voltages. In the H-shaped sample, almost no change of the non-local resistance was observed, even though the gate voltage was varied over a wide range (Fig. 4.3). Due to the large

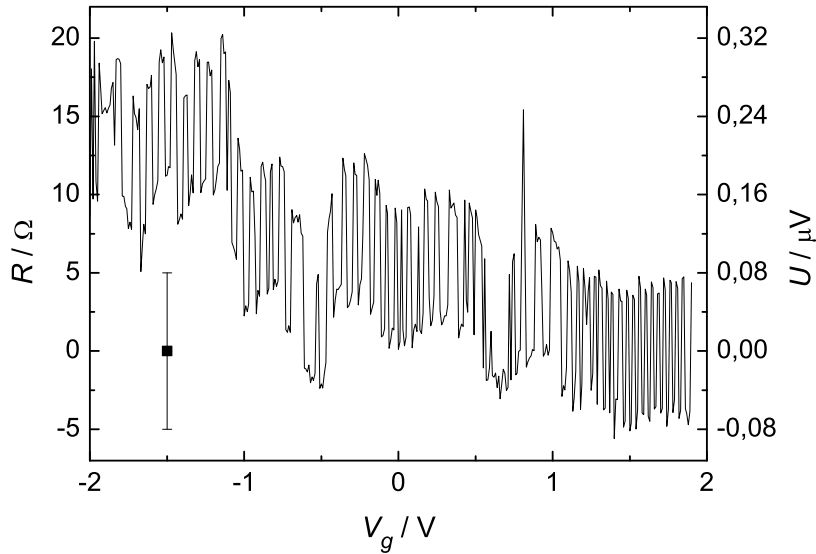


Figure 4.3: The non-local voltage and resistance of an H-shaped device with a large intrinsic density are plotted as a function of gate voltage. The error bar in the lower left corner indicates the noise level.

density, the current is mainly limited by the contact resistance and consequently can be seen as constant. When the noise is neglected, a slight variation of the voltage is obtained. However, this general behavior is not reproducible for repeated measurements. Hence, no clear indication of a charging of the voltage probes was observed.

As can be seen in Ref. 13, the transverse spin current depends crucially on the difference of the momenta for the two Rashba-split branches. While this quantity is proportional to the Rashba parameter α for a splitting linear in k [13], the k -difference can not be determined from Δ_R for HgTe QWs that easily. Here, $\Delta k = k_+ - k_-$ has to be derived from the band structure calculations, when k_{\pm} are the Fermi wave vectors of the Rashba split subbands. For the parameters used in Ref. 30, a significant increase of the non-local voltage was obtained for α larger than 40 meV·nm, corresponding to $\Delta k \approx 0.05 \text{ nm}^{-1}$. This is several times larger than for the investigated sample, where values up to $\Delta k \approx 0.02 \text{ nm}^{-1}$ were achieved. Because of the non-linear dependence of the Rashba splitting on the wave vector for HgTe QWs (cf. Sec. 1.2), a large energy splitting does not necessarily imply a large difference in k . However, the latter is a prerequisite for the experimental observation of the SHE signal.

In contrast to the conduction band, it is quite easy to obtain a large k -difference for the valence band (Fig. 4.4). Due to the almost flat dispersion, already a small Rashba splitting in energy can result in a much larger difference in k than for the conduction band. It has to be noted that a spin Hall effect is also expected, when only one of the subbands is occupied [13]. This can happen when the Rashba splitting is larger than the Fermi energy (cf. Fig. 4.4). In this case, the difference between the two k -values of the one occupied subband at the Fermi energy has to be considered instead of the Fermi wave vectors of the two Rashba-split branches. It was shown for an electron system with only one occupied subband that the spin conductance decreases linearly with the carrier density. Nevertheless, the enhanced Δk can yield a measurable SHE signal, if the density is not too low. Therefore, further measurements were done on

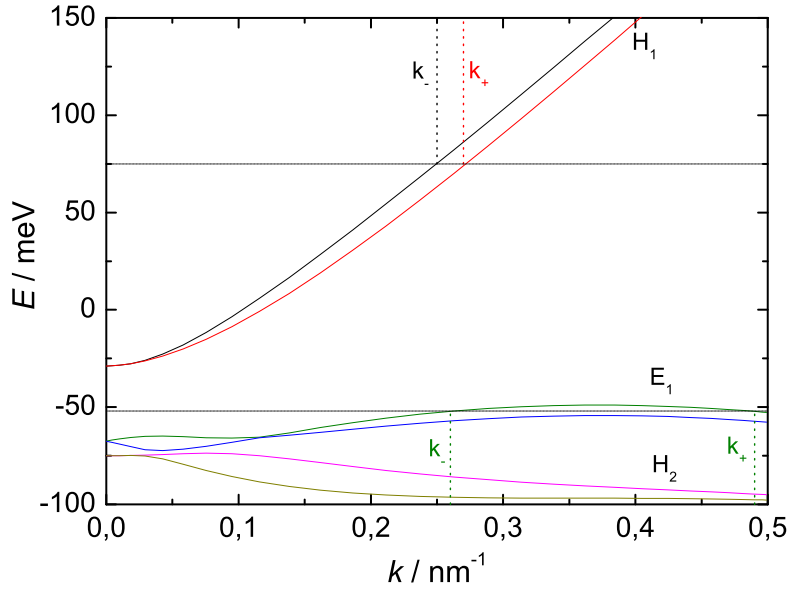


Figure 4.4: The $E(k)$ -dispersion is plotted for an asymmetric 80 Å QW. The dashed horizontal lines indicate two possible Fermi energies for n - and p -conductance, respectively. The dotted vertical lines show the corresponding difference in k .

samples with low intrinsic densities, i.e., $n(V_g = 0) \leq 2.0 \cdot 10^{11} \text{ cm}^{-2}$, which can be tuned to p -conductance by applying moderate gate voltages. Differing from the proposed device (cf. Fig. 4.2), contacts 5 and 6 were added [Fig. 4.5 (a)] to allow for measurements of the longitudinal resistance $R_{34,56} = V_{56}/I_{34}$. Fig. 4.5 (b) shows the current through the device and $R_{34,56}$ as a function of gate voltage. The minimum of the current for $V_g \approx -0.4 \text{ V}$ indicates the insulating regime, i.e., the sample is n -conducting for higher voltages and p -conducting for lower voltages⁴, whereas the measurement of $R_{34,56}$ does not reflect the transition from n - to p -conductance. This can be explained by the fact that the current is determined by the behavior of the

⁴ The voltage range for the insulating regime is comparable to the range that was observed for a macroscopic Hall bar which was used for the characterization of the wafer.

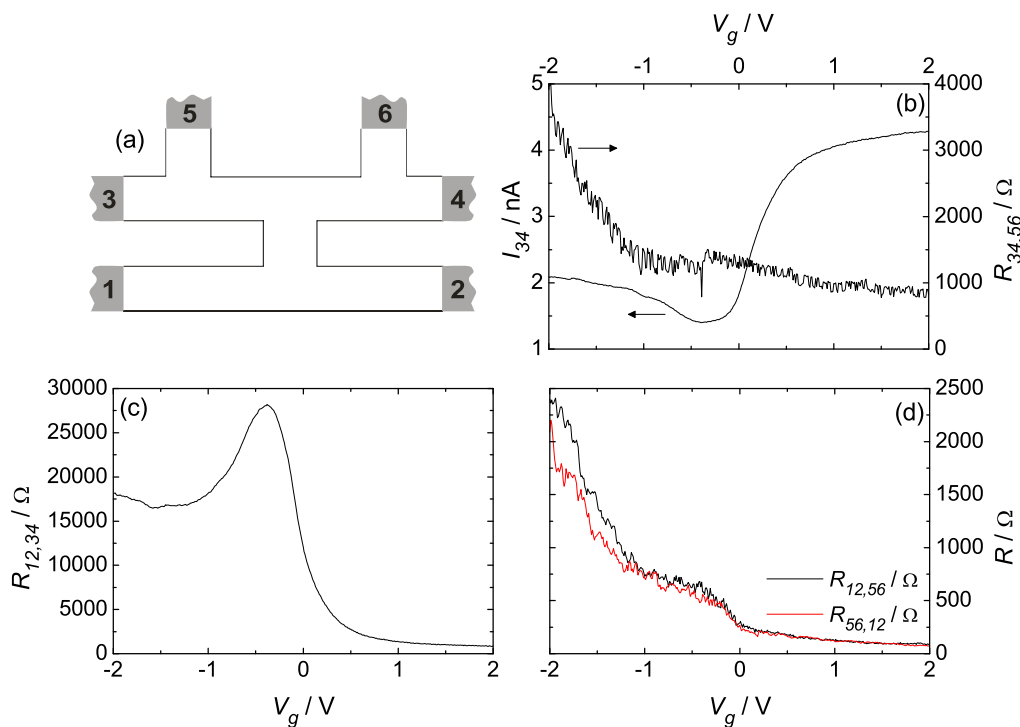


Figure 4.5: (a) A sketch of the device layout is presented. (b) The current and the longitudinal resistance are measured as a function of the gate voltage. (c),(d) The non-local resistance is shown for two different contact configurations [cf. (a)].

entire device, while the four-terminal resistance describes the local properties. A minimum in the current is observed, when most of the gated region is in the insulating regime, even though this might not be the case for the part of the sample between the voltage probes 5 and 6. When the contacts used for current injection and voltage detection are interchanged for a measurement of $R_{56,34}$, a qualitatively identical result is obtained, i.e., the general behavior of R is conserved, but the actual values are slightly different⁵. Hence, it can be deduced that the region between the contacts 5 and 6 is not tuned to p -conductance for the investigated range of V_g .

⁵ This is the case for all contact configurations $R_{ij,mn}$ discussed afterwards.

Such a behavior can be caused by potential fluctuations which enhance the electron density locally.

The non-local resistance $R_{12,34}$, which is shown in Fig. 4.5 (c), provides clear evidence that at least a part of the H-device can be tuned to p -type, passing the QSH state. When the sample is clearly n -type for $V_g \geq 0$, only a small variation of the signal is observed. In contrast, a large non-local voltage is observed for the insulating regime. This can be explained by the QSH edge states, which carry the potential of the current source and drain contact, respectively, to the voltage probes. Since the QSH edge states also exist for low densities in the n - and p -regime (cf. p. 59), the detector leg does not necessarily have to be in the insulating state to enable edge states transport. For this reason, the non-local signal is dominated by the contribution of the edge state transport in the vicinity of the insulating regime, i.e., for approximately $-2.0 \text{ V} \leq V_g \leq 0 \text{ V}$.

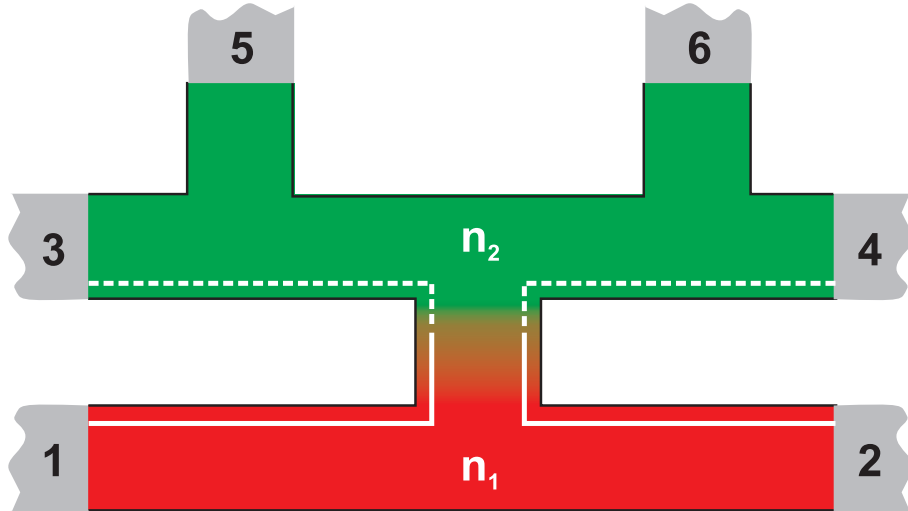


Figure 4.6: Within the device a density gradient occurs. The density n_1 in the red region is lower than n_2 in the green region. The solid white lines indicate the relevant QSH edge states for the insulating regime, while the dashed lines mark the co-existing QSH states at low densities.

When a density gradient within the sample is assumed, the results presented in Fig. 4.5 can be explained consistently. Fig. 4.6 illustrates a possible density distribution in the device. The lower part of the device has a low intrinsic density n_1 and can consequently be tuned to p -conductance. In contrast, the density n_2 in the upper part is significantly higher. Hence, the 2DEG in this part of the device cannot be entirely depleted for the used voltage range and only an increase of $R_{34,56}$ according to the decrease of the electron density is observed. In this contact configuration for a measurement of the longitudinal resistance, the coexistent QSH edge states have only a minor influence, because the bulk transport is dominant. In contrast, mainly the edge states will be responsible for the size of $R_{12,34}$, when the current is injected into the detector leg from the injector by QSH edge states.

The contribution of the QSH states to the total conductance decreases for increasing hole densities. Simultaneously, the non-local resistance due to the edge states is expected to decrease as well. However, an increase of $R_{12,34}$ is observed for $V_g < -1.5$ V. This is an indication of the non-local voltage induced by the spin Hall effect according to the proposal by Hankiewicz *et al.* [30]. For simplicity, the variation of the Rashba splitting of the valence band with gate voltage is neglected. This is justified, because only one of the Rashba-split subbands is occupied. Then, the size of the spin Hall signal is determined by the two different k -values of the occupied subband at the Fermi level. In this particular case, the difference in k increases with the hole density (cf. Fig. 4.4), resulting in a rising non-local voltage.

This interpretation is confirmed by the measurement of $R_{12,56}$ [Fig. 4.5 (d)]. The contacts for current injection and the voltage probes, respectively, are not connected directly by QSH states for this configuration. Possibly existing edge states will be scattered in contacts 3 and 4. Consequently, their contribution can be neglected in comparison to the bulk transport, when neither the injector nor the detector is in the QSH regime. Nevertheless, a non-local resistance can be detected, which is comparable to the longitudinal resistance $R_{34,56}$. This indicates current flow in the upper leg, giving rise to a finite voltage drop between contacts 5 and 6. When a charge current is injected in the lower leg, the spin Hall effect generates a transverse

spin current. The spin current, in turn, induces a charge current in the upper leg. For $V_g > 0$, almost no change of $R_{12,56}$ is observable due to the only small variation of the SO splitting. However, a sudden increase of the resistance occurs, if the injector is tuned to p -conductance for $V_g \approx -1.0$ V. This is attributed to the considerable difference in Δk for the conduction band and the valence band, respectively, resulting in a significant enhancement of the spin current. For the spin current, the influence of the transition from p - to n -conductance, which appears due to the density gradient between the injector and the detector, can be neglected. At the boundary between the p - and the n -region of the device, a narrow QSH regime exists. The polarization of the spin current for the n - and p -type regions is in z -direction, which matches the spin orientation in the QSH edge states. Thus, the spin current will be transmitted. Since the spin current is not accompanied by charge transport, the electrical resistance of the p - i - n transition does not affect the spin transport. In the n -type detector leg, the spin current creates a transverse charge current due to the inverse spin Hall effect. When the spin current is increased by shifting the Fermi energy further into the valence band, the resulting charge current in the detector rises as well. The strong increase of the non-local increase, when the injector leg is in the p -conducting regime, is a clear indication of the existence of both SHE and SHE⁻¹ in our devices. An elastic mean free path of at least 1 μm was observed for other HgTe samples [64]. Since the sample dimensions are smaller than this value, scattering is unlikely and the spin Hall effect is an intrinsic property due to the large SO splitting in this material.

When the contact pairs for current and voltage, respectively, are interchanged for a measurement of $R_{56,12}$, an almost identical trace for $R(V_g)$ is obtained. This observation implies that both SHE and SHE⁻¹ are reversible. When a certain spin current I_S induces a charge current I_C due to the inverse spin Hall effect, the same charge current will generate a spin current I_S due to the SHE. Furthermore, it is hardly conceivable that an extrinsic effect causes an almost identical charging of the non-local voltage probes when injector and detector are inverted. When current and voltage contacts are interchanged, the configuration of scatterers will be different for

the two frameworks and an extrinsic effect based on scattering is expected to yield significantly different results, which is obviously not the case. Rather, the intrinsic spin Hall effect has to be responsible for the observed charging.

The layout of the device was modified for the verification of the SHE on other samples. As can be seen in the inset of Fig. 4.7 (b), the voltage probes 5 and 6 are relocated to a wider part of one of the leads. This modification serves two purposes: First, the influence of these contacts on the non-local measurements, e.g., of $R_{12,34}$, is reduced due to the increased spatial separation. Second, the larger width of the leads compared to the narrow channels in the H-structure was intended to allow for measurements of the Shubnikov-de Haas oscillations, providing direct access to the size of the Rashba splitting. But no distinct oscillations were observed. Apparently, the width of 1 μm is not large enough to prevent backscattering due to potential fluctuations. The device was fabricated from an intrinsically symmetric quantum well. The rather large negative gate voltages, which are required to tune the sample to p -conductance, will simultaneously make the QW potential asymmetric. Thus, the necessary spin-orbit splitting will be obtained for the relevant gate voltage range. Both the current and the longitudinal resistance indicate that the insulating regime occurs for approximately $-3.0 \text{ V} \leq V_g \leq -2.5 \text{ V}$ [Fig. 4.7 (a)]. Again, a strong increase of the non-local resistance $R_{34,12}$ [Fig. 4.7 (b)] is observed for the p -regime, while the current in the injector increases only slightly. Hence, the significant change of the non-local voltage can not be caused by spurious effects like charge injection into detector, e.g., due to scattering. Rather, the charging of the detector has to be attributed to the inverse spin Hall effect.

In contrast, the resistance vanishes for $V_g > -2.5 \text{ V}$, i.e., for the n -conducting regime. On one hand, the SHE signal is much smaller for n -conductance than for p -conductance due to the smaller value for Δk . On the other hand, the sample is almost symmetric around $V_g = 0$ due to the intrinsically symmetric doping of the quantum well. The absence of a non-local signal due to QSH edge states for the insulating regime can be explained by the small width $w = 200 \text{ nm}$ of the device.

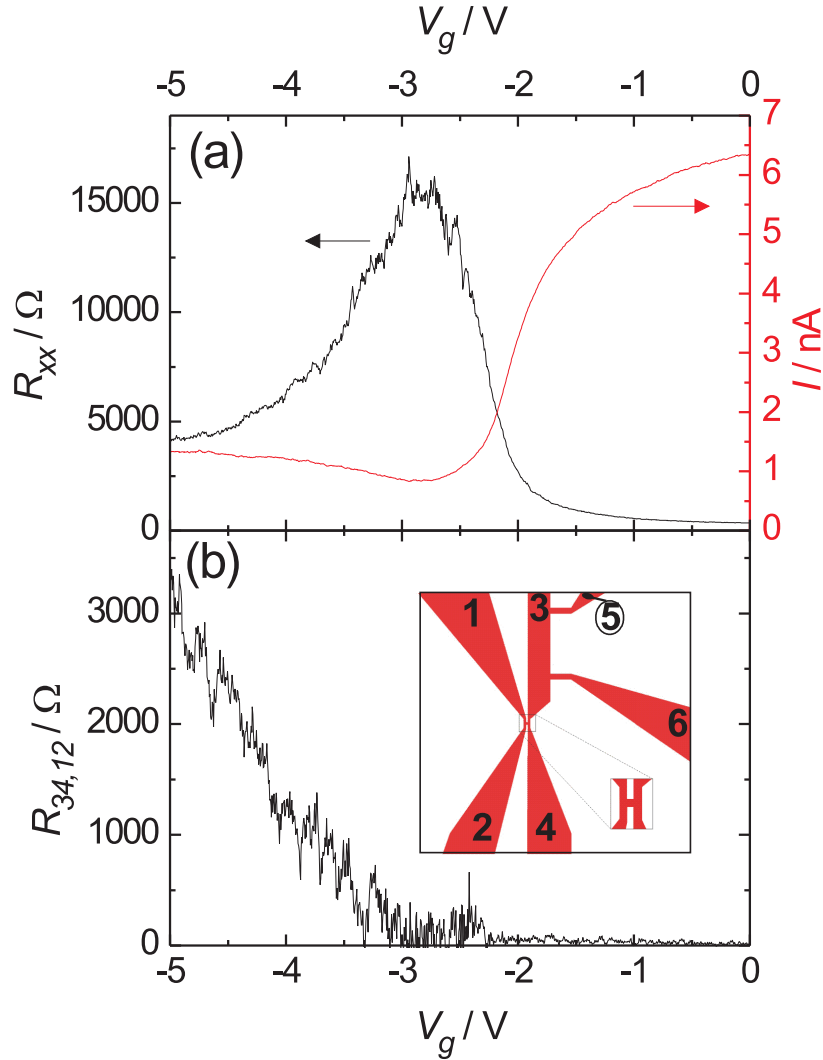


Figure 4.7: The longitudinal resistance R_{xx} , the current I [both shown in (a)] and the non-local resistance $R_{34,12}$ (b) were measured as a function of the gate voltage. The inset of (b) depicts the layout of the device.

When the width of the device is comparable to the extension of the edge states, these can spatially overlap and interaction of states from opposite edges is probable. Then, the contribution of the QSH states to the non-local signal is suppressed. In this case, the transport can no longer be attributed to undisturbed edge states, but rather has

to be considered as bulk transport. For example, small potential fluctuations or a unintended variation of the width due to imperfections of the lithographical process can determine, whether the QSH states actually overlap. If transport by the QSH states is eliminated, the signal due to the SHE can be clearly detected. In general, it depends on the details of the individual devices, if transport by QSH edge states is possible. In that sense, it can be stated that a device, which is good for the detection of the QSHE, is unsuitable for the detection of the SHE and viceversa.

The above interpretation is confirmed by measurements on an identical device fabricated from the same wafer. As shown in Fig. 4.8, the non-local resistance shows a distinct maximum in the insulating regime around $V_g = -1$ V, indicating transport by the QSH edge states. For the conducting regimes, the QSH states still dominate the signal so that the SHE signal can not be detected.

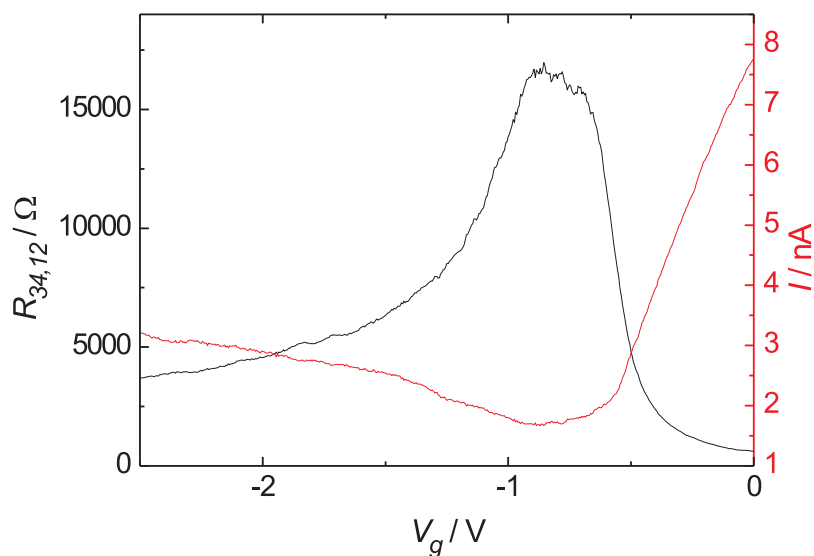


Figure 4.8: The current I and the non-local resistance $R_{34,12}$ are plotted as a function of the gate voltage V_g .

It can be summarized that clear indications for the existence of intrinsic spin Hall effects have been found in H-shaped structures based on HgTe quantum well struc-

tures. The devices are approximately one order of magnitude larger than the one proposed by Hankiewicz *et al.* [30]. The enlargement of the sample is expected to reduce the non-local signal due to the spin Hall effect. Furthermore, the difference in the wave vectors k for the Rashba-split branches of the conduction band is smaller than assumed in the proposal. Therefore, no signal due to the SHE could be observed in n -conducting samples. The situation changes drastically when the device is tuned to p -conductance by an external gate voltage. Due to the large Rashba splitting in HgTe structures, only one of the Rashba-split subbands of the valence band is occupied (cf. Fig. 4.4). In this case, the k -difference does not stem from the two spin-branches but is rather set by the two k -values for the occupied valence subband at the Fermi level, which exceeds Δk of the conduction band by far. Thus, a detectable non-local signal can be expected for the p -type regime despite of the increased sample size compared to the proposed device. As it was shown in the previous chapter, QSH edge states can provide a contribution to the total conductance beside the bulk transport in the vicinity of the insulating regime. Hence, the non-local SHE signal is superimposed by the QSHE signal which is much larger. However, when transport due to the QSH edge states is not possible, e.g., due to scattering or an overlap of states from opposite edges, a clear non-local voltage can be observed for the p -conducting regime. The charging of the voltage probes increases with Δk , when the Fermi energy is shifted further into the valence band. The observed results can be attributed to the intrinsic SHE and SHE^{-1} , respectively, for two reasons: On the one hand, the size of the device is smaller than the elastic mean free path, so that scattering can be almost excluded. On the other hand, the signal is not affected by interchanging the current contacts with the voltage probes, which would obviously be the case for an extrinsic effect based on scattering. Altogether, our experiments provide the first all-electrical measurement of the intrinsic spin Hall effect. Furthermore, the generation of a spin current by the SHE which, in turn, creates a charge current due to the SHE^{-1} in the same material has not been reported previously as well.

4.3 Interplay of SHE and QSHE

A first attempt to observe the spin Hall effect was already made in 2003. Since the QSHE was still an unknown phenomenon, the experimental observations were not understood and the experiments were suspended. However, considering the QSHE shed new light on the results. The design of the devices differs significantly from the one presented above. First, the width of the legs is $5 \mu\text{m}$. Second, the injector and detector leg are covered by separate gate electrodes (Fig. 4.9). Thus, both parts of the device can be controlled individually. The device was fabricated from a

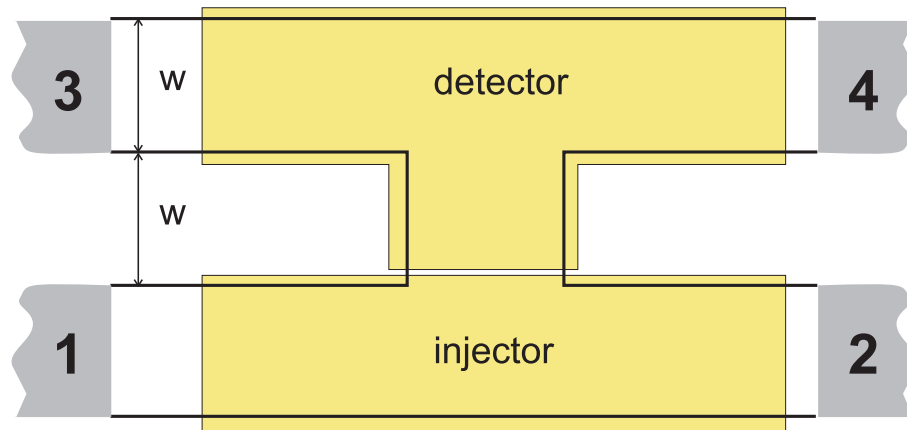


Figure 4.9: In this device, the injector leg and the detector leg are covered by individual gate electrodes. The width w is $5 \mu\text{m}$.

symmetric 120 \AA QW with an intrinsic density of $3.1 \cdot 10^{11} \text{ cm}^{-2}$ and a mobility of $2.79 \cdot 10^5 \text{ cm}^2(\text{Vs})^{-1}$. Due to the low intrinsic carrier density, the device can be tuned from n - to p -conductance, passing the QSH regime. The width $w = 5 \mu\text{m}$ of the legs prevents scattering between the QSH states at opposite edges can be excluded and the transmission of both spin and charge current through the insulating region will only be reduced by inelastic scattering and interaction due to local conducting regions. The measurements discussed below were performed at 4.2 K .

The transition from n - to p -conductance is observed in the sample current, when a negative voltage is applied to the gate covering the injector (Fig. 4.10). The

rather high residual current of approximately 20 nA for the insulating regime, i.e., for $-3.0 \text{ V} < V_{g,inj} < -2.5 \text{ V}$, can be attributed to the large excitation voltage $U_{exc} \approx 10 \text{ mV}$. The voltage applied to the detector gate is kept constant at $V_{g,det} = 0$. When the injector is n -conducting for $V_{g,inj} > -2 \text{ V}$, no non-local signal

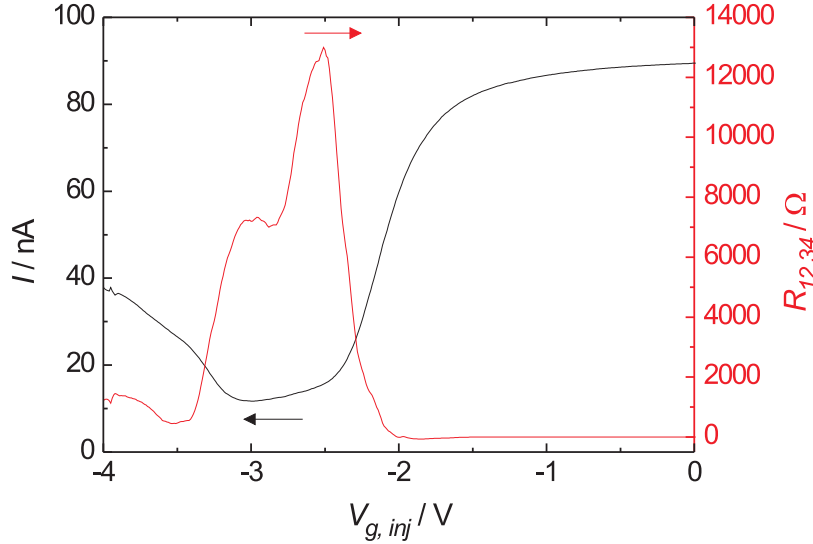


Figure 4.10: Sample current I (black) and non-local resistance $R_{12,34}$ (red) are measured as a function of the voltage $V_{g,inj}$ applied to the electrode covering the injector leg, while the detector gate is kept constant at $V_{g,det} = 0$.

is observed. A strong increase of $R_{12,34}$ occurs, when the injector gets close to the insulating regime, yielding a maximum at $R \approx 13 \text{ k}\Omega$. When the injector is finally tuned to p -conductance, the non-local resistance at first decreases almost to zero for $V_{g,inj} \approx -3.5 \text{ V}$, but rises again subsequently.

As it was shown already in the previous section, the difference in the wave vectors k for the two Rashba-split conduction subbands is not large enough to yield a detectable spin Hall signal, if the entire device is n -type. However, the situation changes drastically for a injector in the QSH regime (bottom part of Fig. 4.11). When a current is driven through the QSH states by an electric field, parallel prop-

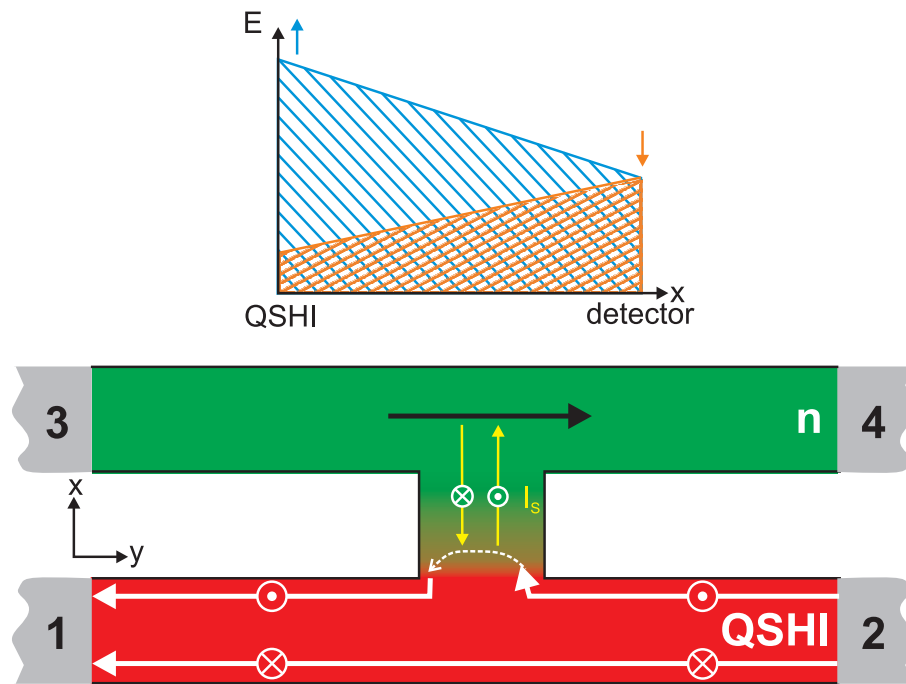


Figure 4.11: (top) Close to the QSH region, the majority of the electrons is spin-up, whereas both spin states are equally occupied in the detector. (bottom) When the injector is in the QSH regime, transport occurs due to spin-polarized edge channels (white arrows), generating a transverse spin current (yellow). In the detector, the induced transverse charge current (black) results in a voltage drop.

agating states at opposite edges have an opposite spin polarization. Since the QSH channels follow the geometrical edge of the sample, the spin-up polarized carriers will enter the connection to the detector leg. In contrast, the spin-down edge state remains localized at the opposite edge. In the n -type region, the spin-up electrons follow the potential gradient towards the current drain (contact 1) and re-enter the edge state at the opposite side. Thus, no charge current is effectively injected into the connection towards the detector. However, the spin-polarization of the carriers causes an unequal occupation of the two spin states at the boundary between the QSH region and the n -type detector (top part of Fig. 4.10). While the density of

spin-up electrons is enhanced at the boundary between QSH region and detector, the spin-down density is lower than in the detector. No spin imbalance is present in the detector leg, providing a gradient of the spin-dependent chemical potential for the two spin states. Consequently, a pure spin current will flow from the injector to the detector. Due to the inverse spin Hall effect, a transverse charge current will be generated, yielding the observed large non-local voltage. In this regime, the spin current is not generated by the spin Hall effect for a doped semiconductor and the SHE^{-1} can be detected independently of the SHE.

When the injector finally is p -type, the large k -difference gives rise to a spin Hall effect. In this case, the carriers have a preferential orientation with respect to the z -direction, but are not fully polarized. Thus, the spin polarization is much smaller than for the QSH edge states and the resulting spin current is also reduced compared to the QSH injector, yielding only a comparatively small non-local signal. When the Fermi energy is shifted further into the valence band, the transverse spin current due to the SHE will increase with Δk , and a rising non-local signal can be observed.

In general, tuning the properties of the injector leg can provide a spin current which, in turn, will create a transverse charge imbalance in the detector due to the inverse spin Hall effect. Having a QSH injector, the SHE^{-1} can be detected independently of the spin Hall effect by means of a purely electrical measurement.

In a second configuration, the detector is tuned by the respective gate electrode. Using this approach, the spin accumulation due to the spin Hall effect can be detected. Here, no voltage is applied to the injector gate and the injector leg remains n -conducting. When the detector is n -type as well, only a small, but finite non-local resistance is observed (Fig. 4.12). On the one hand, this can be a real spin Hall signal for the n -type device. On the other hand, however, it can not be ruled out that the signal stems from a spurious effect caused by, e.g., unintentional charge injection into the detector due to scattering or a misadjustment of the zero point of the measurement setup. In any case, the non-local resistance increases significantly

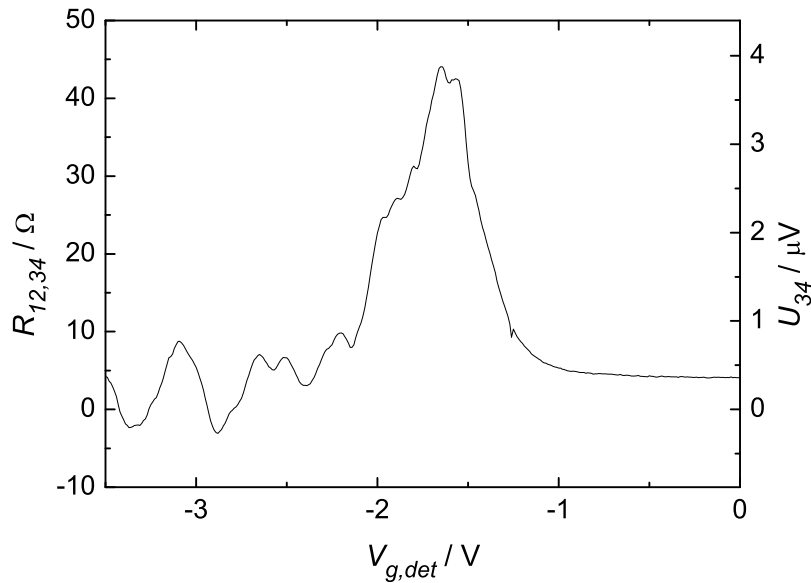


Figure 4.12: The non-local resistance is plotted as a function of the voltage $V_{g,det}$, which is applied to the gate electrode covering the detector.

when the detector is tuned to the QSH regime. The shift of the insulating regime compared to the injector gate can be attributed to the hysteresis-like effect described in Sec. 1.3, which occurs for rather high voltages. In the injector, a spin imbalance will appear at the edges due to the intrinsic spin Hall effect (top part of Fig. 4.13). Due to the low k -difference between the Rashba-split branches of the conduction band, the spin imbalance will be small but finite. When the spin-dependent chemical potential is considered, a difference eU_{SH} in the Fermi energies for the two spin states is obtained at the sample edges. This potential difference can be probed by the QSH edge states. Since the states in the QSH edge channels are spin-polarized, only carriers with a corresponding polarization can be injected. The observed charging of the non-local voltage contacts can be explained using the sketch of the device shown in Fig. 4.13. The QSH edge state connecting contact 4 with the injector only transmits spin-down electrons, whereas the channel to contact 3 carries spin-up electrons.

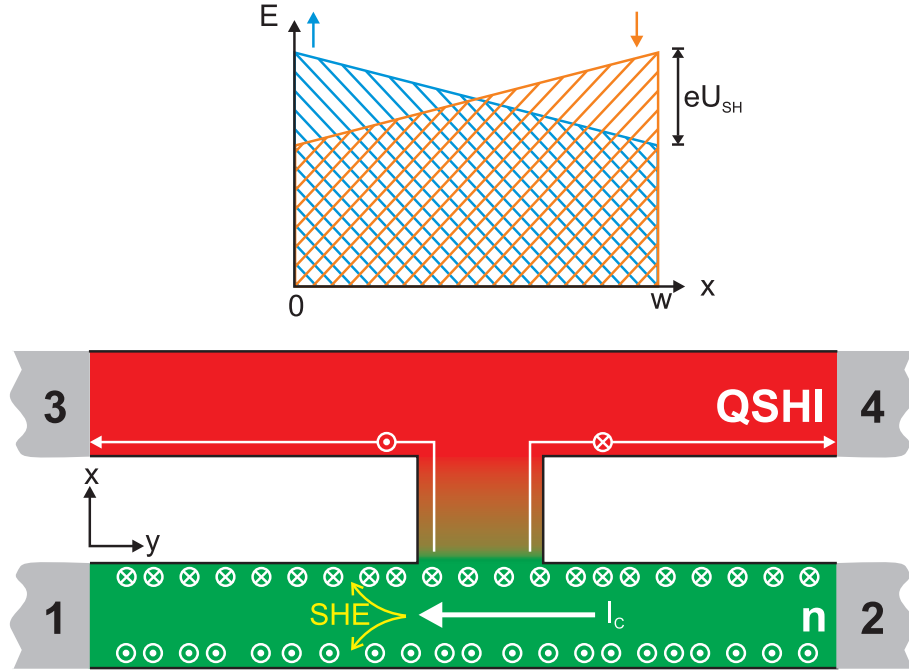


Figure 4.13: The spin Hall effect is reflected in a spin-dependent chemical potential (top). For a detector in the QSH regime, the edge channels from the injector to the non-local voltage probes are spin-polarized (bottom).

When scattering of the edge channels is neglected, the observed voltage difference U_{34} corresponds to U_{SH} . But inelastic scattering is probable, because the length of the edge channels is approximately $20 \mu\text{m}$. The existence of scattering is revealed by the variation of the signal for the QSH regime. When the Fermi energy is close to the conduction band minimum and the valence band maximum for $V_{g,det} \approx -1.4 \text{ V}$ and $V_{g,det} \approx -2.0 \text{ V}$, respectively, the probability of local conducting regions in the QSH insulator is increased and backscattering is enhanced. Thus, only a small non-local signal can be observed. However, backscattering is reduced when E_F is in the center of the energy gap. Altogether, the voltage observed at the center of the insulating regime ($V_{g,det} \approx -1.6 \text{ V}$) is a distinct indication of the spin imbalance at the boundary between injector and detector, while the actual difference between the chemical potential for spin-up and spin-down electrons, respectively, most probably

is larger than the observed value of $4 \mu\text{V}$. Nevertheless, the existence of the spin Hall effect in the injector leg was successfully demonstrated.

The oscillations in the non-local signal for a p -type detector, which is obtained for $V_{g,det} < -2.5 \text{ V}$ (cf. Fig. 4.12), is reproducible for repeated measurements. The observed sign change for the non-local signal based on the SHE^{-1} implies a reversal of the spin current. In principle, it can also occur due to a reversal of the asymmetry of the QW potential. However, this can happen only once when the quantum well is tuned through the point of symmetry, but not repeatedly for a monotonic change of the gate voltage. A spin current is described by the polarization of the spins and the movement of the spin-carrying particles, so that a reversal of either parameter results in a sign change for the spin current. In our devices, the spin current is not accompanied by a charge current. Thus, a variation of the polarization has to be the reason for the observed behavior. A periodic modulation of the spin orientation can be caused by the spin precession due to the Rashba field. This effect was utilized for the proposal of a spin field effect transistor (FET) by Datta and Das [17]. In their device, source and drain contact, respectively, are fabricated from a ferromagnetic material. The intermediate region is a semiconductor with tunable spin-orbit interaction of the Rashba type. Due to the magnetization of the injector, the current is spin-polarized when it is injected to the semiconductor. There, the effective magnetic field B_{eff} due to the SO interaction is oriented perpendicular to the spin-polarization of the injected electrons. The spins will precess with a frequency depending on the strength of the Rashba field. When the electrons reach the detector with a spin parallel to the magnetization of the ferromagnet, they will be transmitted, while they are reflected for an anti-parallel orientation. Thus, the conductance can be tuned by the Rashba field as it was shown theoretically using realistic sample parameters [99].

In contrast to the so-called Datta-Das transistor, no modulation of the transmission between current source and drain is obtained in our device. However, the non-local signal is affected by the same underlying mechanism, i.e., the detected signal depends on the spin precession due to a Rashba field. The spin Hall effect

in the injector leg is utilized for the generation of the spin current. At the boundary between the n -type injector and the p -type detector, a thin QSH region exists. Due to the short length of the edge states, scattering can be excluded and the spin current is transmitted dissipationless. Since the spin imbalance generated by the SHE is not accompanied by a charge current, a pure spin current is injected into the p -type region. While the spin polarization due to the SHE is in z -direction, the effective magnetic field due to the Rashba effect is in the QW plane. Hence, the spins will precess in the p -region, modulating the z -component of their orientation. In the detector, the inverse spin Hall effect will transform the spin current into a transverse charge current. The direction of the charge current, however, is determined by the z -component of the spins. The charging of the voltage probes can be tuned by the detector gate voltage via the Rashba-dependent spin precession. The polarization

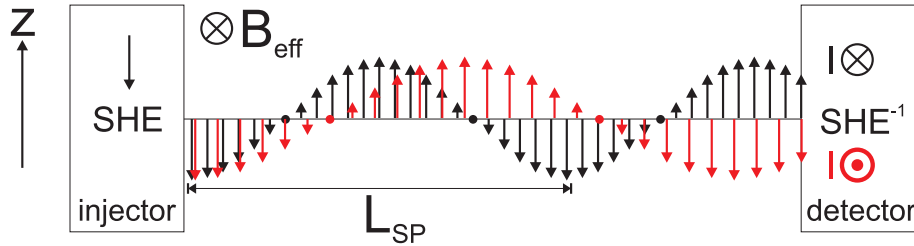


Figure 4.14: When a spin current with polarization in z -direction is injected into a Rashba medium, the z -component of the spins will be modulated due to the spin precession described by the spin precession length L_{SP} .

of the spin current will be reversed after a distance $l = L_{SP}/2$ due to the precession, where L_{SP} is the spin precession length. Using a simple approach including a Rashba splitting $\Delta_R = \alpha k$, $L_{SP} = \hbar^2 \pi / (2m^* \alpha) = 2\pi / \Delta k$ is obtained [17]. Even though such a simple model does not describe our material system quantitatively, it is obvious that the spin precession length can be tuned via the spin-orbit interaction and the difference in k , respectively. Based on realistic values for Δk in the valence band (cf. Fig. 4.4), a spin precession length of approximately 50 nm is obtained. For other two-dimensional systems, values of several 100 nm have been reported

for L_{SP} [17, 99]. For both reasons, a spin precession length of the order of 100 nm is a reasonable estimate for our devices. Consequently, already a small variation of the spin-orbit interaction reverse the spin current entering the detector, because the separation of injector and detector is several times larger than L_{SP} . However, the spin current will decrease due to spin relaxation processes, if the length of the device exceeds the spin diffusion length. Based on the experimental results it can be estimated that the spin diffusion length is at least of the order of some few μm , since the polarization of the spin current would be entirely destroyed otherwise and a non-local signal could not be observed at all.

In conclusion, individual control of the injector and the detector, respectively, by separate top gate electrodes allows for the detection of the spin Hall effect and the inverse spin Hall effect independent of each other. When the injector leg is in the QSH regime, the spin-polarization of the edge states gives rise to a gradient in the spin-dependent chemical potential between injector and detector. A pure spin current will flow which generates a transverse charge current due to the inverse spin Hall effect, resulting in the observed charging of the non-local voltage probes. Our experiments provide, to our knowledge, the first evidence of the SHE^{-1} in a semiconductor system. Furthermore, the spin current was generated in the same material and not injected from a ferromagnetic contact, as it was done for the observation of the SHE^{-1} in other experiments [27–29].

The spin accumulation at the edges of the device due to the spin Hall effect is reflected in a difference in the spin-dependent chemical potential. When the spin-polarized QSH edge states are utilized, this potential difference can be detected in a purely electrical measurement. For a detector in the QSH regime, the polarized edge states carry the chemical potential of the spin-up and spin-down electrons, respectively, to the non-local voltage probes. Even though backscattering between the counter-propagating QSH states at the same edge decreases the voltage signal, the spin accumulation can be demonstrated qualitatively. After detecting the spin accumulation due to the SHE by various optical methods [24–26], the spin imbalance

is demonstrated here for the first time by a purely electrical measurement.

When the injector is n -type and the detector p -type, the non-local voltage oscillates around zero as a function of the gate voltage. This can be explained by the precession of the spins due to the Rashba field. While this precession is utilized for the control of transmission in the so-called Datta-Das spin-FET, it causes a periodic modulation of the spin current in our experiments, resulting in the observed oscillation of the non-local signal. In principle, a similar behavior can be expected, when both injector and detector are p -type. But since the SHE only causes a preferential spin orientation, the signal will be reduced. In the sample configuration used for the experiments, the QSH states connecting injector and detector serve as a spin aligner so that the injected spin current is fully z -polarized. The spin precession length L_{SP} and spin diffusion length L_{SD} can be estimated from the experimental results to be of the order of $1 \mu\text{m}$. However, only for $L_{SP} < L_{SD}$ several oscillations of the non-local voltage can be detected.

As mentioned above, the experiments on the presented device were suspended at an early stage and only a limited amount of data was available. Nevertheless, it was demonstrated that such devices make exciting experiments possible. On the one hand, the spin polarization of the sample edge due to either the spin Hall effect or the QSH effect can be probed. On the other hand, the propagation of pure spin currents can be studied by purely electrical measurements. The above experiments provide strong indication that the observed results are indeed related to spin transport in the sample. However, further measurements are required to definitely rule out spurious effects, e.g., due to QSH states existing in the low-density regime. Additional experiments on similar devices can also provide a deeper insight into spin transport in semiconductor devices, because SHE, SHE^{-1} and the spin-polarization of the QSH edge states can be addressed independently.

4.4 Summary

In this chapter, results from H-shaped devices based on HgTe QWs were presented. The layout of the samples corresponded to the proposal by Hankiewicz *et al.* [30]. However, the size of our devices was at least one order of magnitude larger than in the theoretical proposal. The main reason are limitations in the lithographical process, in which devices can be fabricated reproducibly only for widths down to approximately 200 nm. This size consequently was chosen for the width of the leads in our devices.

In general, a non-local voltage is expected due to a combination of spin Hall effect and inverse spin Hall effect. When the spin-orbit interaction in the sample is large enough, a charge current in the injector leg of the H-device will generate a transverse spin current due to the spin Hall effect. The spin current, in turn, induces a transverse charge imbalance, which can be detected as a voltage difference between the two contacts in the detector leg. When the sample dimensions are small compared to the typical mean free path and the spin-orbit splitting is large, the intrinsic effect will be dominant compared to the extrinsic effect based on scattering.

In fact, a large difference in k is required for the existence of the SHE rather than a large Rashba splitting in energy. Thus, no clear signal attributed to the SHE was detectable for an n -type device, where Δk of the conduction band is too small. In addition, the possible non-local signal is reduced due to the rather large size of our devices. The former obstacle can be overcome, if the sample is tuned to p -conductance. Due to the flat dispersion of the valence band and the substantial SO interaction, only one of the Rashba-split subbands is occupied. In this case, the two different k -values for the same subband at the Fermi level have to be considered for the SHE. Their difference is much larger than Δk in the conduction band, so that a distinct SHE signal is detected. It has to be noted that the SHE signal can be concealed by a non-local signal due to the QSH edge states, which still exist at low n - and p -densities, respectively. When Δk is enhanced by shifting the Fermi level further into the valence band, the non-local voltage increases accordingly. Our

experiments provide clear evidence for the existence of spin Hall effect and the inverse spin Hall effect in our devices. It is the first time that the SHE has been demonstrated for a semiconductor system by means of purely electrical measurements. The experimental findings can be attributed to the intrinsic SHE, because high mobilities in the studied devices make scattering unlikely on the length scale of the device, which is comparable to the mean free path.

While the QSH states may complicate the detection of the SHE in some experiments, they can also be utilized for an independent detection of spin Hall effect and inverse spin Hall effect in suitable devices. For this purpose, injector leg and detector leg are controlled by separate gate electrodes. The enhanced width $w = 5 \mu\text{m}$ of the leads clearly separates the states located at opposite edges. When the injector leg is in the QSH regime, the spin imbalance at the interface between the QSH region and the n -type detector drives a pure spin current towards the detector leg. There, the inverse spin Hall effect generates a transverse charge current. The observation of the resulting non-local voltage drop demonstrates the existence of the SHE^{-1} in HgTe quantum wells. When it comes to the detection of the spin Hall effect, QSH states in the detector can be utilized. For an n -conducting injector, the SHE yields a spin imbalance at the edges of the leg. Since the QSH states in the detector are spin-polarized, they will carry the chemical potential of the respective spin state to the non-local voltage probe and the observed voltage reflects the difference in the spin-dependent chemical potential. Only a qualitative analysis of the spin imbalance created by the spin Hall effect is possible, because the QSH states are likely to scatter due to their length of approximately $20 \mu\text{m}$. In general, both SHE and SHE^{-1} have been observed for the first time in a semiconductor by purely electrical measurements. Furthermore, the spin-polarization of the QSH edge states can also be inferred from the above results.

Peculiar non-local transport properties appear, when the SO interaction in the p -conducting detector is varied, while the injector is n -type. The observed oscillations of the non-local signal around zero can be explained by the precession of the spins due to the effective Rashba field. Since the injected spin current due to

the spin Hall effect is polarized in z -direction, the spins will precess around the in-plane Rashba field in the detector. The spin precession length is determined by the strength of the Rashba field and can consequently be tuned via the gate voltage. Depending on the sign of the z -component of the spin orientation in the detector, the direction and amplitude of the charge current due to the inverse spin Hall effect is varied, yielding the observed oscillatory behavior of the non-local resistance.

A task for future experiments is a more quantitative investigation of the SHE and SHE⁻¹. For this purpose, it is reasonable to study the two effects independently of each other, employing the spin-polarized QSH edge states. It is crucial in this context that scattering of the QSH states is minimized. On the one hand, this calls for a wide separation of opposite sample edges to prevent a spatial overlap of the states. On the other hand, the edge states have to be shorter than the inelastic mean free path to avoid scattering between the counter-propagating states at a single edge. The fabrication of such devices is feasible with established lithographical techniques, so that the above issues can be addressed.

Another device, which relies on the above findings, is similar to the Datta-Das spin-FET. First if all, spin precession due to the Rashba field was successfully demonstrated in our devices. Furthermore, the spin-polarized QSH states might provide a good alternative to the ferromagnetic contacts included in the initial proposal, which were an obstacle for a realization of such a device so far. Thus, it seems possible to fabricate a spin-FET purely based on HgTe quantum well structures.

Chapter 5

Transport in ring structures

In search of possible spin-based electronic applications, various approaches were proposed. Two of the main issues in this context are the injection of a spin-polarized current into a device and the manipulation of the spin state. It was shown that the injection of a significantly spin-polarized current from a metal into a semiconductor is not possible [3]. Thus, many devices where the Rashba effect is utilized to manipulate the polarization of the electron spin, e.g., the Datta-Das spin field effect transistor [17], are difficult to realize. This obstacle can be overcome if, for example, devices are fabricated from a single appropriate semiconductor material.

Following this approach, Nitta *et al.* [16] suggested a ring-shaped structure based on an InGaAs-2DEG, i.e., a system with large spin-orbit interaction. In this device, the interference of electrons passing different arms of the ring controls the transmission. The most probably best-known interference effect in ring structures, the Aharonov-Bohm effect [100], requires an external magnetic field, which is unfavourable for most electronic applications. However, interference effects can also be obtained when the Aharonov-Casher phase [15] is considered. This effect is analogous to the Aharonov-Bohm effect if the role of the magnetic and electric field is interchanged. For the Aharonov-Casher effect, the magnetic moment of the moving particle, e.g., the electron spin, is coupled to an electric field, which may be caused by spin-orbit interaction. Additionally, a SO Berry phase can also occur in

such systems. Thus, a controlled variation of the Rashba spin-orbit interaction can modulate of the transmission through the device.

Due to the large tunability of the Rashba splitting, HgTe-based QW structures are an excellent candidate for the realization of spin-interference devices as described above. Earlier experiments on ring structures already gave an indication of spin-orbit related phase effects [34]. These observations initiated more detailed studies, which are presented in this chapter. The experimental results for our devices provide the first direct observation of the dynamical part of the Aharonov-Casher phase.

Further experiments on HgTe ring structures have been used to investigate phase effects especially in high magnetic fields. In this case, the AB phase is the dominant contribution to the electron wave function and the SO-related phase effects can be neglected. Since the period of the AB oscillations is determined by the magnetic flux enclosed by the electron orbit, such experiments can provide information about the electron paths in the ring structure. It will be shown that the effective radius of the orbit decreases for increasing magnetic fields, which is attributed to the appearance of edge states in the quantum Hall regime.

5.1 General description of phase effects

If the characteristic dimensions of a device are significantly larger than the phase coherence length, only the particle-like properties are relevant and phase effects can be neglected in the experiment. But the wave properties gain in importance for samples with smaller dimensions. The particle-wave dualism is reflected in the quantum mechanical description of a particle by a wave function

$$\Psi = A \cdot \exp(i\varphi). \quad (5.1)$$

The amplitude A is usually used for normalization purposes, and the phase φ describes the propagation of the wave in time and space.

For a single wave function, no experimental access to the phase is possible, because the expectation value of an observable quantity X is obtained by

$$\langle X \rangle_{\Psi} = \langle \Psi | X | \Psi \rangle = \int \Psi^* X \Psi. \quad (5.2)$$

Due to the use of the complex conjugates Ψ and Ψ^* , the phase term cancels out. Phase-related effects can be observed if a superposition of at least two different partial waves Ψ_i occurs. In this case, the expectation value of X is given by

$$\begin{aligned} \langle X \rangle_{\Psi_1 + \Psi_2} &= \int (\Psi_1 + \Psi_2)^* X (\Psi_1 + \Psi_2) \\ &= \langle X \rangle_{\Psi_1} + \langle X \rangle_{\Psi_2} + \int \Psi_1^* X \Psi_2 + \int \Psi_2^* X \Psi_1. \end{aligned} \quad (5.3)$$

As shown above, the first two terms are independent of the phase of the individual partial waves. However, the phase factors of the two partial waves do not cancel out for the latter terms. Thus, interference effects between the two partial waves become observable and can provide information about the phase difference.

The most probably best-known realization of the phase acquired by a particle wave function is the so-called Aharonov-Bohm (AB) effect. The effect was named after Y. Aharonov and D. Bohm, who showed that a charged particle like an electron can acquire a phase if it is coupled to a magnetic vector potential [100]¹. In their

¹ The effect was already described in 1949 by Ehrenberg and Siday [101], but their description remained unnoticed.

thought experiment, they considered a split electron beam, which passes a cylindrical solenoid on opposite sides. A magnetic field is confined within the solenoid, whereas it vanishes on the outside and consequently can not affect the electron orbit. However, the corresponding vector potential A is present and leads to a modulation of the phase of the electron wave function:

$$d\varphi = \frac{e}{\hbar} \vec{A} d\vec{s}, \quad (5.4)$$

where $d\vec{s}$ is an infinitesimal part of the electron orbit. Finally, the two split branches of the initial beam are combined again, leading to interference between electrons of the two beams. The phase difference for the two split beams is

$$\begin{aligned} \Delta\varphi &= \frac{e}{\hbar} \int_{s_1} \vec{A} d\vec{s} - \frac{e}{\hbar} \int_{s_2} \vec{A} d\vec{s} \\ &= \frac{e}{\hbar} \oint \vec{A} d\vec{s} \\ &= \frac{e}{\hbar} \int \vec{B} d\vec{S}, \end{aligned} \quad (5.5)$$

where $d\vec{S}$ is a surface element of the area enclosed by the electron orbit. The last transformation is based on the definition of the magnetic vector potential, $\vec{A} = \vec{\nabla} \times \vec{B}$. Thus, the phase does not depend on the magnetic field on the electron orbit, but on the magnetic flux enclosed by it. This means that the electron itself has not necessarily to be exposed to a magnetic field along its course to acquire an Aharonov-Bohm phase. The phase difference between two paths passing the suggested solenoid is given by

$$\Delta\varphi = \frac{e}{\hbar} \Phi = \frac{2\pi\Phi}{\Phi_0}, \quad (5.6)$$

where Φ is the magnetic flux enclosed by the two interfering paths and $\Phi_0 = h/e$ is the magnetic flux quantum. A full oscillation period, i.e., a phase change of 2π , emerges if the enclosed flux is varied by one flux quantum h/e .

First experimental evidence for the AB effect was provided by R. G. Chambers in 1960 [102]. He modified an electron microscope in such way that it could be used as an interferometer. For one of the reported experiments, no magnetic field was

present at the path of the electrons, but a magnetic flux was enclosed by the two partial beams. In this configuration, a shift of the interference pattern was observed, confirming the theoretical prediction.

A similar phase effect was predicted in 1984 by Y. Aharonov and A. Casher [15]. They described the new effect as the electromagnetic dual to the AB effect. While the AB phase results from the movement of a charged particle in a magnetic vector potential, the relevant properties of the particle and the potential are interchanged for the so-called Aharonov-Casher (AC) effect. In resemblance to the AB effect, a vector potential $\vec{A} \sim \vec{E} \times \vec{\mu}$ was introduced, which couples a magnetic moment $\vec{\mu}$ to an electric field \vec{E} . Thus, an AB-like phase will be acquired by a particle with a magnetic moment which moves around an electric field. The first observation of the AC effect was obtained for neutrons [103], followed by experiments using Ca and Rb atoms, respectively [104, 105].

In a seminal paper [14], Berry provided a general description of geometric phase effects, which is based on an adiabatic variation of the environment of the system. The notion of an adiabatic process indicates that the evolution of the parameters included in the Hamiltonian is slow enough to keep the system in an eigenstate at any time. When the system returns to its original state after a cyclic evolution, the phase shift of the wave function depends on the evolution of the Hamiltonian in phase space. Both the AB phase and the AC phase represent a special case of the general Berry phase. The former one was explicitly given as an example by Berry in his paper. A few years after the initial prediction by Berry, Aharonov and Anandan showed that a geometric phase can be acquired by any cyclic evolution, i.e., an evolution in which the system returns to its original state, even though adiabaticity is not given [106]. In fact, the Aharonov-Anandan phase tends to the Berry phase for increasing adiabaticity and finally reaches it in the adiabatic limit. The first experimental observation of the geometric Berry phase beside the AB effect was achieved for photons in wound optical fibre [107].

Through the past decades, several phase effects like the AB effect, the AC effect and, more general, the Berry phase, have been theoretically predicted. All these effects have been verified by interference experiments with particles meeting the particular requirements for the individual effects, e.g., electrons for the AB effect. While the respective first demonstration of the phase effects was not achieved in a solid state system, all above effects are supposed to be observable in suitable semiconductor devices as well.

5.2 Phase effects in semiconductor ring structures

The above general description of the individual phase effects can be adapted to the special case of a ring structure with spin-orbit coupling subjected to a homogeneous external magnetic field. Such experiments will be discussed in the following chapter.

As shown in Eq. 5.6, the phase due to the Aharonov-Bohm effect is determined by the magnetic flux enclosed by the electron orbit. For a homogeneous magnetic field B perpendicular to a ring structure with radius r , the phase difference between the two partial waves passing through the different arms of the ring is given by

$$\Delta\varphi = \frac{e}{\hbar} \Phi = \frac{e}{\hbar} r^2 \pi \cdot B. \quad (5.7)$$

From this it follows that the periodicity of the AB oscillations in magnetic field is solely determined by the ring radius:

$$\Delta B = \frac{h}{r^2 \pi e}. \quad (5.8)$$

The first realization of the AB effect on semiconductor ring structures was achieved by Timp *et al.* who studied devices fabricated from GaAs/AlGaAs heterostructures [108].

The influence of the spin-orbit interaction on the electron phase was introduced theoretically by Meir *et al.* [109]. They assumed the presence of spin-orbit scattering for a mesoscopic system in an AB geometry, where two distinct paths enclose a

finite magnetic flux. The SO contribution to the phase can be described by an additional effective magnetic flux. This transformation can be used for any property of the system, which does not explicitly depend on the electron spin. Mathur and Stone extended this idea by considering a uniform SO interaction, e.g., due to the inversion asymmetry of a two-dimensional semiconductor system [110]. They confirmed the results of Meir and coworkers, now using a uniform electric field perpendicular to the plane of motion instead of random SO scattering. It was furthermore predicted that several oscillation periods due to the AC effect may be observed in samples with typical dimensions for a feasible tuning of SO interaction. The first explicit prediction for a ring structure was provided by Oreg and Entin-Wohlman [111]. Considering SO scattering, it was shown that the transmission T through a one-dimensional ring depends periodically on the magnetic flux and the SO interaction:

$$T = f\left(\cos(2\pi\Phi/\Phi_0 \pm \lambda/2)\right), \quad (5.9)$$

where λ is a dimensionless parameter proportional to the effective magnetic flux describing the strength of the SO scattering [109]. It can be deduced from this relation that both the magnetic field and the SO interaction affect the transmission of a ring structure. A more elaborate description of the effect of SO interaction on the electron phase was given by Qian and Su [112]. If the orientation of the electron spin deviates from the z -axis by an angle χ , the SO-related phase is proportional to $\pm\alpha \sin \chi$, where α is the spin-orbit parameter². A deviation of the spin from the direction of the external magnetic field is caused by an effective in-plane magnetic field due to the SO interaction (Fig. 5.1). The two signs for the electron phase refer to a parallel and anti-parallel orientation of the spin with respect to the total magnetic field, respectively.

The above description of SO-based phase effects is not complete, since it only includes the so-called dynamical phase, i.e., a phase acquired due to the movement

² In Ref. 112, the SO parameter is given by κ , which is proportional to α . However, the notation as α is used in line with other parts of the thesis.

along a certain path. The geometric Berry phase, however, has not been considered yet. Its contribution to the electron phase is obtained for the variation of an experimental parameter like the orientation of the magnetic field along the path. The direction of the magnetic field is modulated by the spin-orbit interaction, which can be represented by an effective in-plane magnetic field B_{eff} . The resulting total magnetic field is given by

$$\vec{B}_{\text{tot}} = \vec{B}_{\text{ext}} + \vec{B}_{\text{eff}}. \quad (5.10)$$

Because the effective Rashba field is always directed perpendicular to the direction of motion, the total field will rotate when the electron moves around the ring³, yielding the so-called spin-orbit Berry phase [113]

$$\varphi_{\text{geom}} = \pm\pi(1 - \cos\theta), \quad (5.11)$$

where θ is the angle between the external and the total magnetic field:

$$\theta = \tan^{-1} \frac{B_{\text{eff}}}{B_{\text{ext}}}. \quad (5.12)$$

For a non-adiabatic system, a geometric Aharonov-Anandan phase similar to the Berry phase can be observed [112]. In this case, the angle θ of Eq. 5.11 has to be substituted by χ , which is the tilt angle of the electron spin with respect to the external magnetic field. In the fully non-adiabatic regime, the electron spin is not affected by the SO field and consequently will be aligned with the external field yielding $\chi = 0$, while $\chi = \theta$ for the adiabatic case, i.e., the SO Berry phase is the adiabatic limit of the Aharonov-Anandan phase.

In real samples, the adiabatic limit is reached if the spin follows the varying magnetic field at any time. This condition is equivalent to $\omega_s t \gg 1$, where $\omega_s = g\mu_B B/2\hbar$ is the Larmor frequency describing the spin precession around the magnetic field and t is the time scale on which the direction of the magnetic field varies significantly. In a ballistic 1D device with length L , this is the time needed for one cycle around the ring structure, i.e., $t \approx L/v_F$. A similar condition was obtained for a ballistic

³ A similar experiment considering a spatially varying magnetic field was already proposed by Berry in the initial prediction of the geometric phase [14].

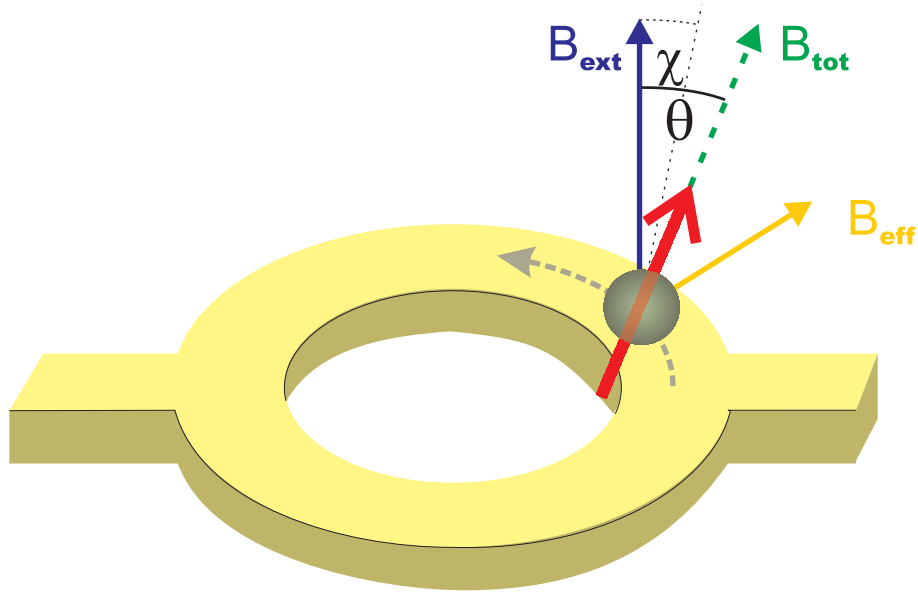


Figure 5.1: When electrons pass a ring structure in the presence of both an external magnetic field B_{ext} and an effective field B_{eff} due to the SO interaction, the spin (red) is aligned with the total magnetic field B_{tot} . For non-adiabatic transport, the angle χ of the spin orientation deviates from θ .

2D device [114]. For a diffusive sample, the relevant time scale for the adiabatic criterion has been discussed controversially. One approach uses the elastic scattering time, demanding a rather large magnetic field to reach the adiabatic limit [115–117]. Contrary to this prediction, it was stated by Loss and coworkers that the time of diffusive transport around the ring is the relevant time scale for adiabaticity [118–120]. In this case, already small magnetic fields are sufficient for the adiabatic limit. Up to now, no generally applicable criterion for adiabaticity was presented, which can solve the important issue.

When all phase contributions mentioned above are included, the phase difference between two partial waves passing different arms of a ring with radius r is described by [16]:

$$\Delta\varphi_{\psi_{\uparrow}^+ - \psi_{\uparrow}^-} = -2\pi\frac{\Phi}{\Phi_0} - \pi(1 - \cos\theta), \quad (5.13)$$

$$\Delta\varphi_{\psi_{\downarrow}^+ - \psi_{\downarrow}^-} = -2\pi\frac{\Phi}{\Phi_0} + \pi(1 - \cos\theta), \quad (5.14)$$

$$\Delta\varphi_{\psi_{\uparrow}^+ - \psi_{\downarrow}^-} = -2\pi\frac{\Phi}{\Phi_0} - 2\pi r\frac{m^*\alpha}{\hbar^2} \sin\theta, \quad (5.15)$$

$$\Delta\varphi_{\psi_{\downarrow}^+ - \psi_{\uparrow}^-} = -2\pi\frac{\Phi}{\Phi_0} + 2\pi r\frac{m^*\alpha}{\hbar^2} \sin\theta. \quad (5.16)$$

Here, \uparrow (\downarrow) refers to an (anti-)parallel alignment of the electron spin with the magnetic field and the superscript $+(-)$ denotes a (counter-)clockwise evolution, respectively. In all above equations, the first term on the right hand side can be identified as the AB phase $\Delta\varphi_{AB}$ due to the enclosed magnetic flux Φ . For Eqs. 5.13 and 5.14, the second term is the geometric SO Berry phase $\Delta\varphi_{\text{geom}}$, i.e., the system is assumed to be in the adiabatic limit. The second term of Eqs. 5.15 and 5.16 is the dynamical part of the AC phase $\Delta\varphi_{AC}$ due to the SO interaction described by the Rashba parameter α . A variation of the SO interaction will affect both the Rashba parameter α and the angle θ . The AC phase will increase continuously with α . In contrast, the SO Berry phase is limited to $\Delta\varphi_{\text{geom}} \leq \pi$, because it depends solely on θ , which can be tuned from 0 for $B_{\text{ext}} \gg B_{\text{eff}}$ to $\pi/2$ for $B_{\text{ext}} \ll B_{\text{eff}}$.

Several groups have claimed evidence for an experimental observation of the SO Berry phase in semiconductor ring structure [31–33]. All of them inferred the existence of the Berry phase from a complex structure of the Fourier transform of the AB oscillations, i.e., a splitting of the AB peak and side peaks, respectively. However, these interpretations have been questioned [121–123]. The main objections relate either to technical aspects of the Fourier transform, which make artificial side peaks possible, or to an inadequate theoretical modeling.

It can be summarized that an unambiguous experimental verification in semiconductor structures has only been accomplished for the AB effect. Both the Aharonov-Casher effect and the SO Berry phase were predicted not only to occur in systems with substantial spin-orbit interaction but also to be observable in ring structures fabricated from suitable materials. However, a direct demonstration is still outstanding.

5.3 Observation of the Aharonov-Casher effect

The aim of the experiments presented below is to provide direct evidence for phase effects due to spin-orbit interaction. For this purpose, ring structures were fabricated from HgTe/HgCdTe quantum well structures with a well width of 120 Å (cf. Fig. 1.6). This QW width was chosen, because highest mobilities had been achieved for this width until then. The structures were symmetrically modulation doped. In such samples, the spin-orbit interaction is supposed to vanish due to the intrinsic symmetry of the QW potential. Ring-shaped devices with a average radius $r = 1 \mu\text{m}$ were fabricated from these samples by e-beam lithography and wet chemical etching. The width of the leads in each arm was 300 nm. After the fabrication of the devices, a top gate was deposited to be able to tune the Rashba splitting in a wide range.

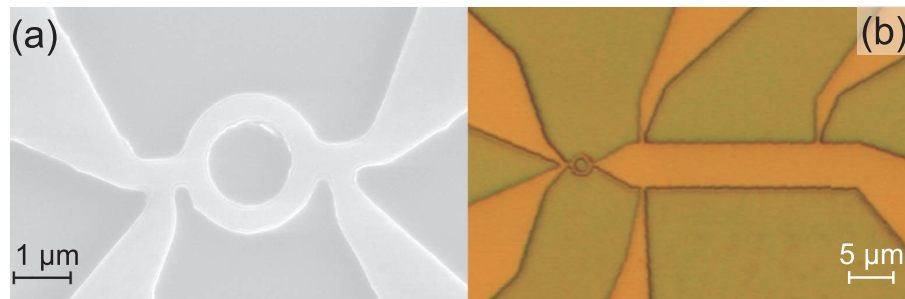


Figure 5.2: (a) A scanning electron microscope picture shows a typical ring structure with a radius $r = 1 \mu\text{m}$ and a width of the leads of 300 nm. (b) For a later generation of samples, a ring of the same size was attached to a Hall bar; the top gate electrode is not applied yet (picture taken by optical microscope).

A first set of experiments was performed on single rings [Fig. 5.2 (a)]⁴. While a dependence of the interference pattern on the gate voltage was observed, no quantitative analysis of the SO interaction was possible. To meet this purpose, the devices were extended by a Hall bar, which was attached to the ring structure [Fig. 5.2 (b)]. There, much more distinct Shubnikov-de Haas oscillations can be detected and the

⁴ Some of the results are presented in Ref. 34

Rashba splitting can be deduced by means of Fourier transformation. Several such devices were investigated and showed comparable results with respect to the effects discussed below. For clarity, the detailed analysis below will be restricted to data obtained from one sample.

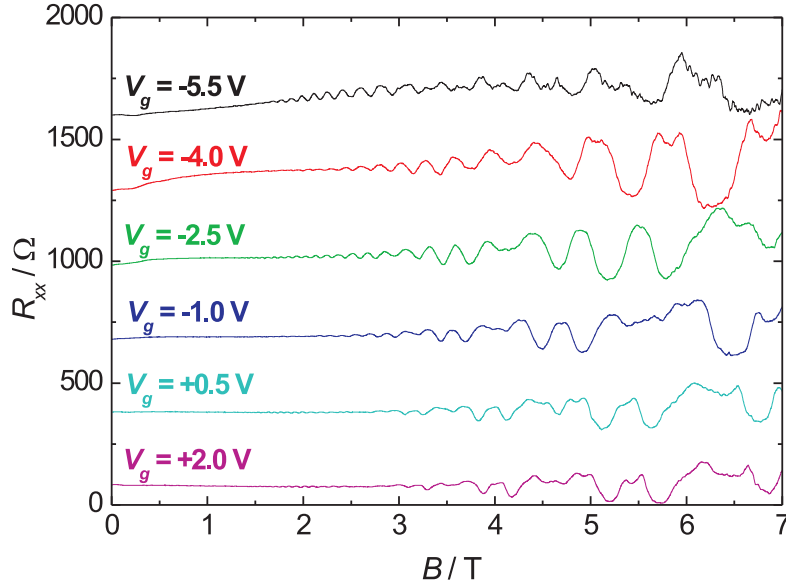


Figure 5.3: When the gate voltage is varied, the pattern of the SdH oscillations in the longitudinal resistance R_{xx} is modulated. (The traces are offset for clarity.)

From Shubnikov-de Haas oscillations in the longitudinal resistance, which was measured for various gate voltages (Fig. 5.3), the occupation of the Rashba-split subbands is inferred by an analysis of the Fourier spectrum. Over a wide range, the total carrier density depends linearly on the gate voltage with

$$n(V_g) = n(V_g = 0) + 0.182 \cdot 10^{12} \frac{\text{cm}^{-2}}{\text{V}} \cdot V_g, \quad (5.17)$$

where $n(V_g = 0) = 2.29 \cdot 10^{12} \text{ cm}^{-2}$ is the intrinsic carrier density (inset of Fig. 5.4). A $8 \times 8 \mathbf{k} \cdot \mathbf{p}$ band structure calculation was used to fit the SdH oscillations in order to determine Rashba splitting as a function of gate voltage. The voltage corresponding

to $\Delta_R = 0$ was estimated by interpolation as $V_g(\Delta_R = 0) = (-2.57 \pm 0.02)$ V. The deviation of the point of symmetry from $V_g = 0$ is inconsistent with a symmetrically doped sample, but can be explained either by an unintentional asymmetry of the doping or by the insulator on top of the structure, which can affect the potential in the barriers as well due to the introduction of interface states. In addition, defects induced by the e-beam lithography can result in additional doping. It turned out that Δ_R scales linearly with the gate voltage for the range -6.5 V $\leq V_g \leq 0$ V:

$$\frac{\partial \Delta_R}{\partial V_g} = 3.15 \frac{\text{meV}}{\text{V}}. \quad (5.18)$$

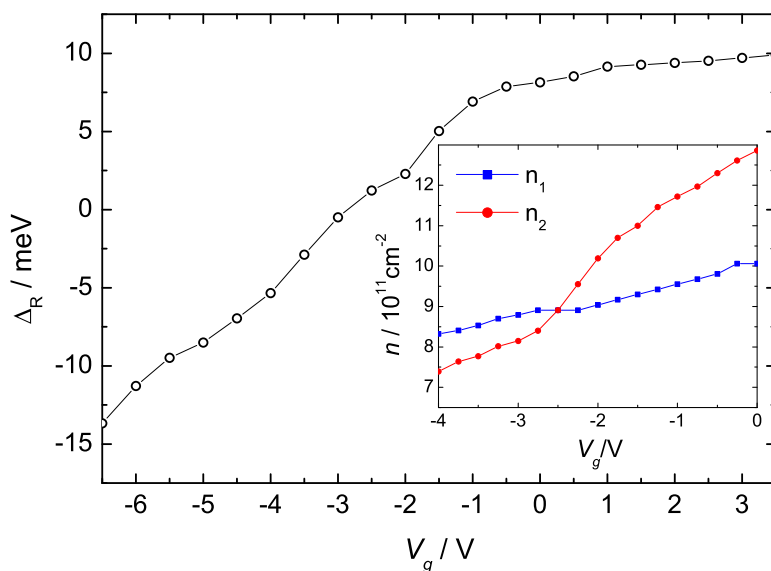


Figure 5.4: The Rashba splitting Δ_R can be tuned through zero by the gate voltage. The empty circles represent the results of the theoretical fits to the experimental data for the respective gate voltages. The inset shows the population of the Rashba split subbands in the vicinity of the point of symmetry.

As can be seen in Fig. 5.4, the Rashba splitting can be tuned from -15 meV to +10 meV. While negative energies are not reasonable in general, this notation is

used here to identify the two distinct regimes with finite Rashba splitting on either side of the point of symmetry. The sign change can be understood as an indication of the reversal of the electric field causing the Rashba effect (cf. Sec. 1.2). The precise control of the Rashba splitting via the applied gate voltage is necessary for a quantitative study of the phase effects induced by spin-orbit interaction.

In the vicinity of the symmetry point, i.e., for $V_g \approx -2.57$ V, pure Aharonov-Bohm oscillations are expected, because the influence of the SO interaction on the electron phase can be neglected. The oscillation pattern for $V_g = -2.57$ V is shown in Fig. 5.5. The periodicity of the oscillations of 1.3 mT is in good agreement with

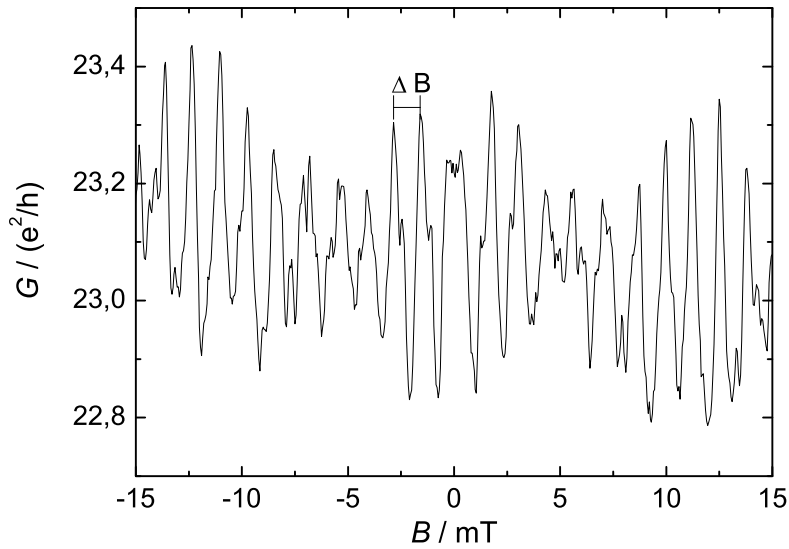


Figure 5.5: The Aharonov-Bohm oscillations are plotted for $V_g = -2.57$ V, i.e., $\Delta_R \approx 0$.

the ring radius of $1 \mu\text{m}$ (cf. Eq. 5.8). The background conductance of approximately $23 e^2/h$ indicates that several modes are transmitted through the ring. This can be attributed to the width of the leads of 300 nm , which is several times larger than the Fermi wavelength $\lambda_F \approx 20 \text{ nm}$.

Even though the SO interaction is supposed to be negligible, a distinct beating pattern is observed. In Ref. 33, a similar behavior has been considered as evidence of the existence of the SO Berry phase. However, a modulation of the oscillation amplitude can also originate from the finite width of the ring structures. In a two-dimensional system, several modes are transmitted and, consequently, contribute to the total conductance. Depending on the strength of the B -field, the transmission of the individual modes varies, e.g., due to different scattering probabilities. This will result in a modulation of the amplitude of the conductance oscillations and in the occurrence of seemingly irregular behavior, e.g., at $B = \pm 7.5$ mT.

If the gate voltage is varied at $B = 0$, oscillations of the conductance are observed (Fig. 5.6). The amplitude of the oscillations is comparable to the one for the AB oscillations in finite magnetic field. Beside SO-related phase effects, a different

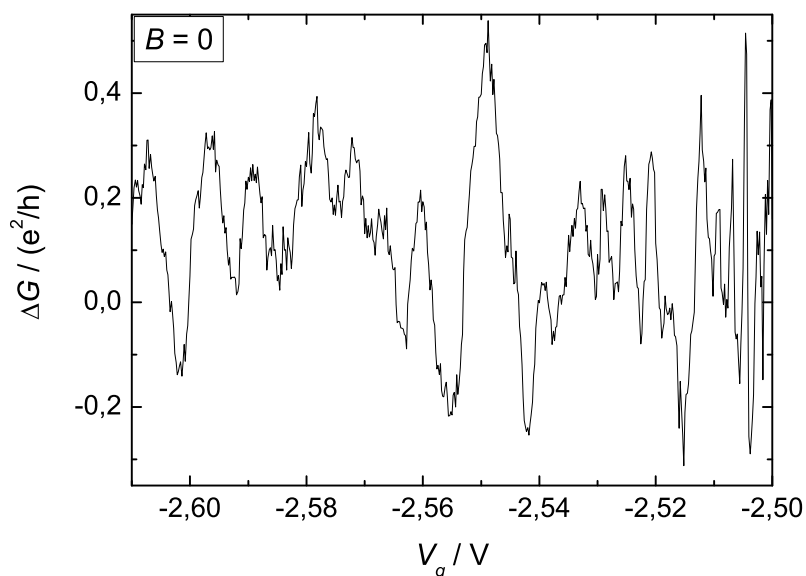


Figure 5.6: Oscillations of the conductance are observed as a function of gate voltage for $B = 0$. The background conductance has been subtracted in this figure.

length of the two arms can cause such oscillations. In the case of an asymmetric ring structure, a phase difference depending on the wave vector k_i and the length l_i of the individual arms will appear:

$$\varphi_{\text{asymm}} = k_1 l_1 - k_2 l_2, \quad (5.19)$$

where $i = 1, 2$ denotes the different arms. It can be assumed that the wave vector in both arms is identical, i.e., $k_1 = k_2 = k$ and $\varphi_{\text{asymm}} = k \cdot \Delta l$. A variation of k by a modulation of the density n will yield a phase shift

$$\Delta\varphi_{\text{asymm}} = \frac{\partial\varphi}{\partial n} \Delta n = \frac{\partial\varphi}{\partial k} \frac{\partial k}{\partial n} \Delta n = \Delta l \sqrt{\frac{\pi}{2n}} \Delta n. \quad (5.20)$$

For a simple estimation of $\Delta\varphi_{\text{asymm}}$, the length difference between the two electron paths is assumed to be 300 nm, which is the width of the leads. Taking a carrier density of $n = 2 \cdot 10^{12} \text{ cm}^{-2}$ and the dependence $n(V_g)$ as given in Eq. 5.17, a change of the gate voltage by approximately 1 V is required to achieve a phase shift of 2π . Hence, the effect of an asymmetry of the ring structure can be neglected for the voltage range depicted in Fig. 5.6.

It is more likely that the oscillations are caused by the variation of the SO interaction via the gate voltage and, consequently, clearly indicate the presence of SO-related phase effects. It was shown in Ref. 16 that the conductance modulation in a one-dimensional ring due to the SO interaction is given by

$$G = \frac{e^2}{h} \left[1 + \cos \left(2\pi r \frac{\alpha m^*}{\hbar^2} \right) \right]. \quad (5.21)$$

However, no periodic behavior is observed in our samples due to the non-parabolic energy dispersion of the HgTe QWs. As can be seen in Fig. 1.5, the Rashba splitting is not proportional to k and can not be described by a constant parameter α as used in the above model. Thus, a linear dependence of Δ_R on V_g does not necessarily come along with a linear variation of α , and consequently non-periodic conductance oscillations can appear as a function of gate voltage.

A more comprehensive picture of phase effects in the investigated ring structures

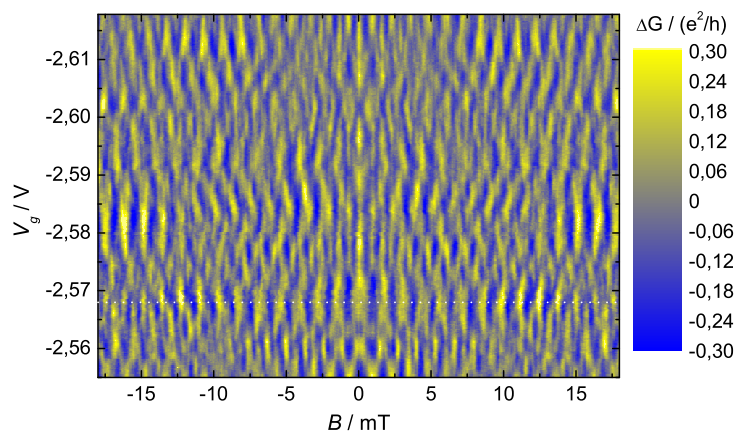


Figure 5.7: When both external magnetic field and gate voltage are varied, a complex interference pattern is obtained; yellow and blue regions indicate large and low conductance, respectively.

is obtained, when both magnetic field and gate voltage are varied. The resulting interference pattern is plotted in Fig. 5.7, which shows a complex dependence of the oscillations on the experimental parameters. Close to the gate voltage corresponding to a symmetric QW potential, i.e., $\Delta_R(V_g) = 0$, no effect of the gate voltage on the AB oscillations is expected. From this consideration, the point of symmetry can be located precisely at $V_g = -2.568$ V, which is in excellent agreement with the interpolation of the data obtained from the SdH oscillations (cf. Fig. 5.4). As stated above, the phase shift due to the SO Berry phase is limited to $\pm\pi$, whereas the dynamic part of the AC phase continuously increases with the SO strength. Thus, the observed variation of the interference pattern can be attributed to the latter contribution. The dynamic AC phase depends on the orientation of the electron spin with respect to the total magnetic field (Eqs. 5.15 and 5.16) and therefore leads to a splitting of the AB-type oscillations, when the SO interaction is tuned by the gate voltage. Hence, the observed interference pattern is in qualitative agreement with the behavior expected from Eqs. 5.13 - 5.16.

The interference pattern as a function of both external magnetic field and SO interaction was modeled theoretically in order to verify that the experimental results are indeed a consequence of the AC phase. The numerical calculations were performed by E. Hankiewicz and J. Sinova⁵. Their calculations are based on the Landauer-Büttiker formalism [124]. The Hamiltonian for a 2D ring structure with SO interaction in a perpendicular magnetic field is given by

$$\hat{\mathbf{H}} = \frac{(\vec{p} - e\vec{A})^2}{2m^*} + \frac{\alpha}{\hbar}[\vec{\sigma} \times (\vec{p} - e\vec{A})]_z + \frac{1}{2}g\mu_B\sigma_z B + \hat{\mathbf{H}}_{\text{conf}} + \hat{\mathbf{H}}_{\text{dis}}, \quad (5.22)$$

where the terms on the right hand side are the kinetic energy, the Rashba SO interaction, the Zeeman term, the confinement energy and the disorder, respectively. The conductance of 1D ring structures can be determined analytically [16, 125–127]. Since the finite width of our devices allows for multichannel transport, a rather simple 1D model is not sufficient. For the modeling of our devices, a concentric tight-binding approximation is used to include multichannel effects (Fig. 5.8).

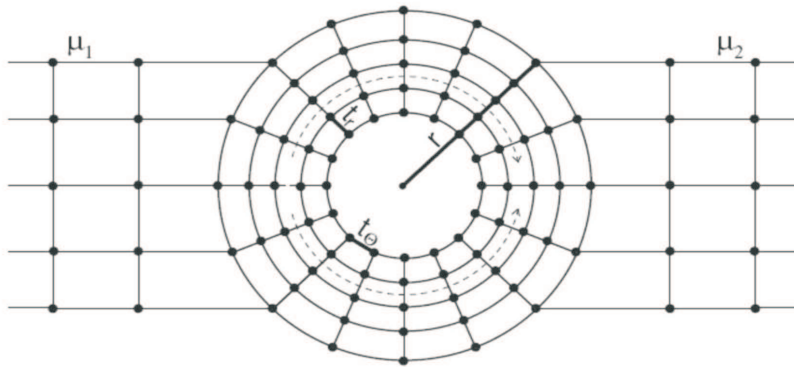


Figure 5.8: The 2D ring structure is modeled using a concentric tight-binding approximation.

For transport due to a single channel, a chessboard-like pattern in conductance is observed as a function of magnetic field and Rashba splitting [Fig. 5.9 (a)]. The conductance varies between $2 e^2/h$ for full transmission, i.e., constructive interference

⁵ At that time, both were member of the Physics Department at Texas A&M University, Austin.

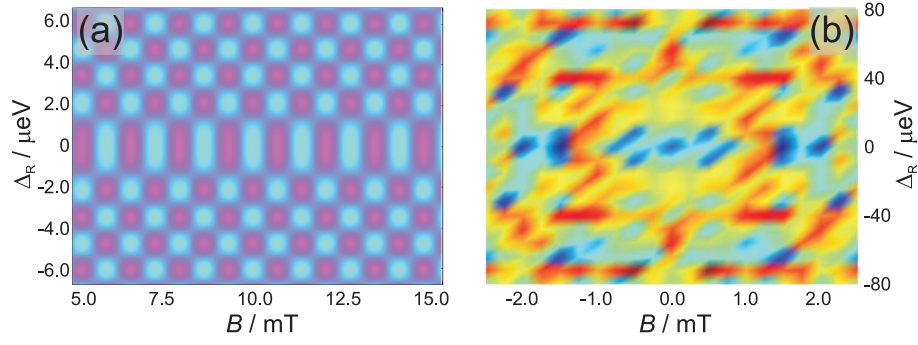


Figure 5.9: (a) For a single channel, a chessboard-like interference pattern is obtained. (b) When the number of coherently conducting channels is increased (here: six modes), the pattern becomes irregular. Pink and red (cyan and blue) indicate high (low) conductance in (a) and (b), respectively.

of the two paths, and zero, i.e., no transmission due to destructive interference.

From comparison to the experimental results and considerations given above, it is obvious that more than one channel is involved in transport through the device. For the calculation presented in Fig. 5.9 (b), a ring with ten modes was assumed, where six modes conduct coherently, i.e., six channels contribute to the interference pattern, while the remaining four only give rise to a constant background. Since several channels are present, scattering can occur between the individual modes and suppress the interference. No distinct oscillations are obtained but a rather complex pattern. The interference pattern is expected to become more irregular when the number of coherent modes is further increased.

The distinct interference pattern, which has been observed in our experiments, strongly indicates that only one channel transmits coherently. However, several additional modes must be present in the ring, resulting in the observed background in conductance of $G \approx 23 e^2/h$. The incoherent transport by these channels may be caused by impurities and imperfections in the ring structure, e.g., due to the lithographical process.

For the theoretical modeling, a ring with six channels was assumed, where only one mode conducts coherently. Even though the conductance of approx. $23 e^2/h$ indicates that more than six modes are involved in transport, the model provides reasonable results. While scattering between coherent and non-coherent channels will affect the interference pattern, the exact number of non-coherent channels is not crucial for the modeling, since coherence will be destroyed by any process of inter-mode scattering. Therefore, a variation of the number of incoherent modes will mainly affect the background conductance.

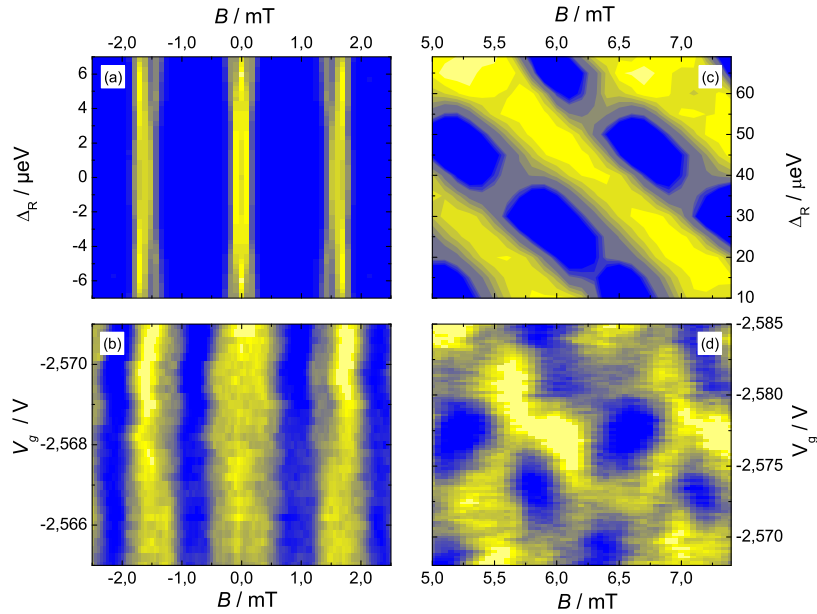


Figure 5.10: The conductance as a function of magnetic field and Rashba splitting was calculated (a) for $\Delta_R \approx 0$ and (c) for finite SO interaction. In both cases, the theoretical results are in good agreement with the experimental observation in the corresponding gate voltage range shown in (b) and (d), respectively.

For a very low Rashba splitting, the contribution of the SO interaction to the electron phase can be neglected and oscillations solely due to the AB effect are observed. This situation is reflected in the calculations for $|\Delta_R| \leq 5 \mu\text{eV}$ [Fig. 5.10 (a)].

The prediction agrees well with the experimental results around the point of symmetry $V_g = -2.568$ V [Fig. 5.10 (b)]. The variation of the Rashba splitting in the theoretical data complies well with the voltage range shown in the experimental figure if the dependence $\Delta_R(V_g)$ determined from the analysis of the SdH-oscillations is taken into account (cf. Eq. 5.18).

Fig. 5.10 (c) shows the theoretical calculation for finite Rashba splitting. The AB oscillations are shifted diagonally, because the AC phase increases with the Rashba parameter α . It can be seen in Eqs. 5.15 and 5.16 that the sign of the AC contribution to the phase depends on the orientation of the electron spins in the two arms of the ring. Thus, the undisturbed AB oscillations, as they are obtained for vanishing SO interaction, split and shift towards lower and higher magnetic fields, respectively, when the Rashba splitting is increased. As for the calculations with $\Delta_R \approx 0$, the theoretical model matches the experimental observation [Fig. 5.10 (d)]. The depicted voltage range corresponds directly to the variation of the Rashba splitting used for the calculations without any additional adjustable parameter.

In this section, the transmission of ring structures fabricated from HgTe-based QWs has been investigated as a function of magnetic field and gate voltage. Aharonov-Bohm-like oscillations are observed in an external magnetic field. They can be used to analyze phase effects due to the spin-orbit interaction in the samples. A tuning of the Rashba splitting yields a distinct modulation of the interference pattern. Since a spurious effect due to an unintentional asymmetry of the ring structure can be ruled out, the modulation of the AB-like oscillations can be attributed to phase contributions induced by the SO interaction. While the variation of the SO Berry phase is limited, the dynamical part of the AC phase increases continuously with the Rashba strength and, consequently, gives rise to the observed interference pattern. This interpretation is confirmed by comparison of the experimental data to theoretical calculations. Thus, the experimental results provide the first direct observation of the dynamical AC phase in semiconductor structures.

5.4 Measurements in high magnetic field

While the measurements in the previous section were limited to small magnetic fields $B \ll 1$ T, the analysis of the Aharonov-Bohm-type oscillations will be extended to much larger fields in this section. The experiments were performed on similar HgTe-based ring structures with an average radius $r = 1 \mu\text{m}$ and a width $w = 300$ nm of the leads. In case of large fields, phase effects can be interpreted in an easier way, because the effective SO-field B_{eff} can be neglected in comparison to the much larger external field B_{ext} . The angle θ , which enters both the AC phase and the SO Berry phase (cf. Eqs. 5.13 - 5.16), tends towards zero and the phase contributions depending on θ vanish. Thus, occurring oscillations are purely due to the AB effect.

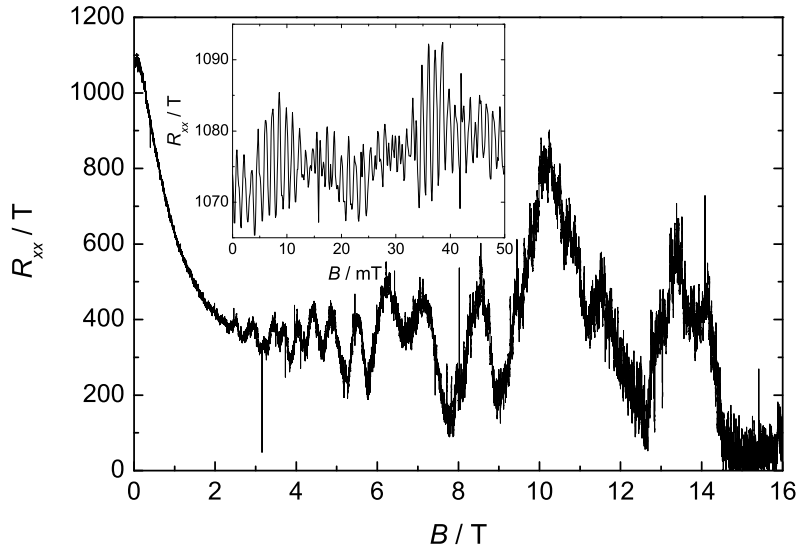


Figure 5.11: The longitudinal resistance R_{xx} is measured across the ring structure. The inset shows the AB oscillations for small magnetic fields.

Fig. 5.11 shows the magneto-resistance of the ring structure. Clear SdH oscillations are observable for $B > 2$ T and a carrier density of $2.3 \cdot 10^{12} \text{ cm}^{-2}$ can be deduced from the Fourier transform. The position of the SdH peaks is in excellent

agreement with the data obtained from the attached Hall bar. Unlike for measurements at the Hall bar, R_{xx} stays finite in the minima of the SdH oscillations even for large magnetic fields, which indicates scattering between the counter-propagating edge states. This can be explained by the lower spatial separation of the edge states due to the reduced width of the leads in the ring compared to the Hall bar [cf. Fig. 5.2 (b)]. Superimposed on the SdH signal, periodic oscillations can be observed for all magnetic fields due to the AB effect. For B around zero, the oscillation frequency of $f_{AB} \approx 770 \text{ T}^{-1}$, which corresponds to a period of 1.3 mT, agrees with the ring radius of $1 \mu\text{m}$ (see inset of Fig. 5.11). When the magnetic field is increased, the frequency of the AB oscillations decreases (Fig. 5.12). The data points for the individual B -field values were obtained from the respective Fourier transform of the AB oscillations in the range $B \pm 0.5 \text{ T}$. The plotted traces were obtained for gate voltages from -2.5 V to $+3.0 \text{ V}$. In this voltage range, the Rashba splitting is tuned from approximately zero to 10 meV (cf. Fig. 5.4). Despite the large variation of the

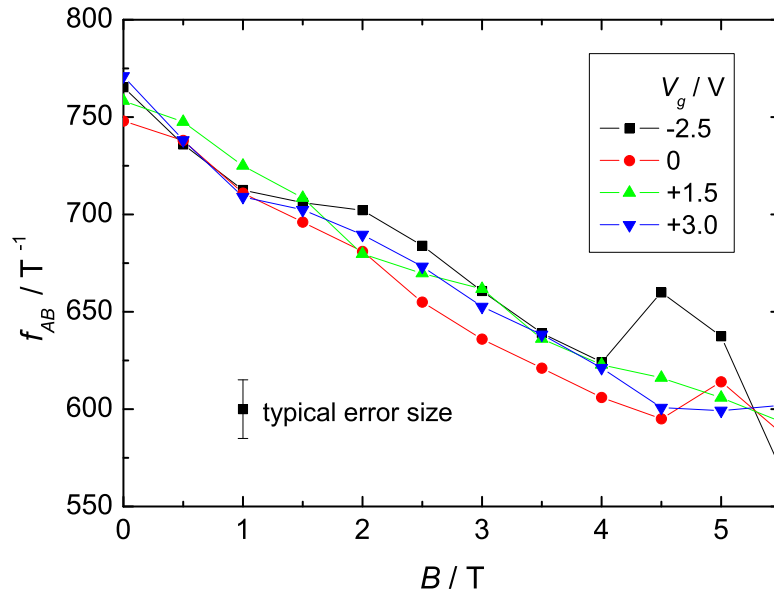


Figure 5.12: The frequency of the AB oscillations is plotted as a function of the magnetic field for various gate voltages.

SO interaction, all traces coincide within the given accuracy. This indicates that a effect due to SO interaction, albeit possibly present, is negligible. The frequency of the AB oscillations is given by

$$f_{AB} = (\Delta B)^{-1} = \frac{r^2 \pi e}{h}. \quad (5.23)$$

Accordingly, a decrease of the frequency may be attributed to a local attenuation of the external magnetic field. This might originate from an effective magnetic field, which is oriented anti-parallel to the external field. However, the effective magnetic field, which is obtained from the experimental variation of the oscillation frequency, rises quadratically with the external field up to $B_{\text{eff}} \approx 0.8$ T for $B_{\text{ext}} = 6$ T. Such large fields are unrealistic and can be ruled out as an origin of the decreasing AB frequency.

A decrease of the area enclosed by the electron orbit, which is generally possible for leads with a finite width w , can also explain the observed behavior. Then, the electron paths can be shifted within the lithographical boundaries of the device. If a homogeneous behavior for the entire sample is assumed, the electron orbit can be described by an effective radius r_{eff} . In our devices with an average radius $r = 1$ μm and a width $w = 300$ nm, the effective radius of the electron orbit is limited to $(r - w/2) = 0.85$ $\mu\text{m} \leq r_{\text{eff}} \leq (r + w/2) = 1.15$ μm .

From the data presented in Fig. 5.11, the AB oscillations were extracted by subtracting the SdH background from the total signal. The resulting oscillatory signal was used to determine the AB frequency. The deduced effective radius (Eq. 5.23) decreases with increasing magnetic field (Fig. 5.13). For large fields $B > 8$ T, the effective radius saturates close to 0.85 μm , which corresponds to the value of the inner radius of the ring structure. Thus, the data is consistent with a shift of the electron path for finite magnetic field.

An explanation for the decreasing effective radius can be inferred from the magneto-transport measurements presented in Fig. 5.11. For low magnetic fields $B < 2$ T, no SdH oscillations are observable. This indicates that the electron paths

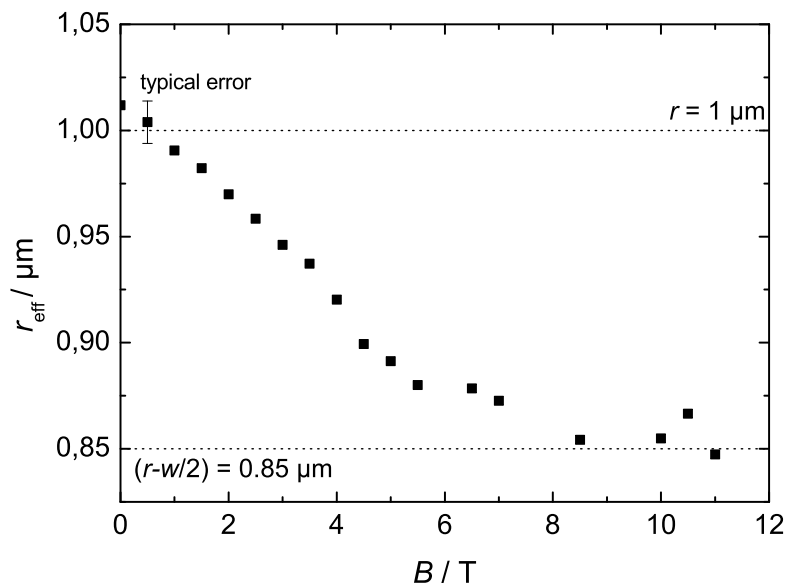


Figure 5.13: The effective radius of the electron orbit decreases with increasing magnetic field.

are spread over the entire width of the sample. For larger fields, SdH oscillations dominate the signal. This indicates that transport occurs mainly through edge channels.

Independent of the exact number of edge channels, the counter-propagating edge states do not interact in an ideal sample (Fig. 5.14). The states at the outer edge (dotted lines) connect the leads attached to the ring and are consequently responsible for the transport through the device. In fact, because of the oppositely directed propagation of these states, transport occurs only through one of the arms, which makes interference impossible. In contrast, the states at the inner edge (dashed line) form closed loops, allowing for full circular movement around the ring. Since these states do not interact with the states at the outer edge, they are not involved in transport. Thus, no AB oscillations are expected when transport occurs by undisturbed edge states.

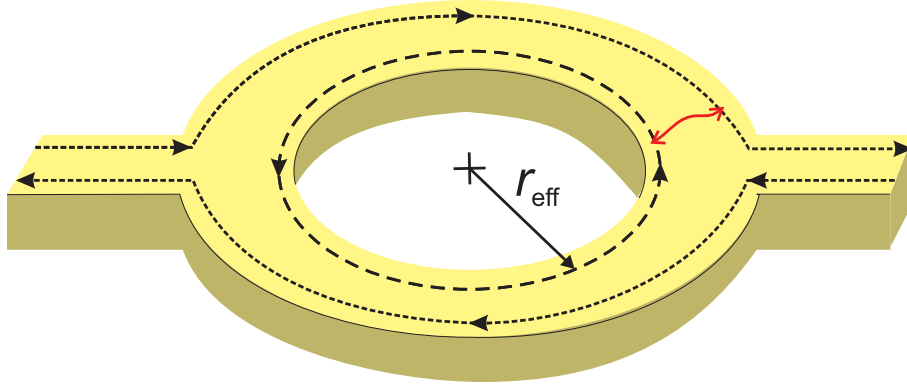


Figure 5.14: The edge state transport through a ring structure is schematically illustrated. The red line indicates a possible event of scattering between states at the inner and outer edge, respectively.

However, the non-vanishing longitudinal resistance indicates scattering between counter-propagating edge states, as stated above. Since an interaction of the inner and outer edge is possible, the states at the inner edge can be seen as a ring structure coupled to the transmitting states at the outer edge. The phase acquired by electrons circling the closed loop at the inner edge manifests itself in the transmission through the ring by the observed AB oscillations for high fields.

When the magnetic field is increased, the average position of the occupied edge states at the inner edge will be shifted towards the center of the ring. Hence, the effective radius will decrease, as observed in the experiments. Finally, all states will be located as close to the inner edge as allowed by the edge potential, resulting in a saturation of the effective radius at $r_{\text{eff}} \approx r - w/2 = 0.85 \mu\text{m}$.

Camino *et al.* studied transport through a two-dimensional island with $r = 1.3 \mu\text{m}$ in high magnetic fields [128]. In the narrow leads, which were used as contacts to the island, scattering between the counter-propagating edge states was possible. Thus, a closed loop is formed by the channels at the outer edge of the device and interference is possible. In their experiments, distinct AB oscillations corresponding to the enclosed magnetic flux were observed. The sample layout is comparable to

our devices if the inner edge states are neglected. However, there is no indication of oscillations due to interference of outer edge states in our experiments. While scattering between states located at the inner and the outer edge, respectively, can occur within the entire ring structure, the counter-propagating states at the opposite outer edges can only interact directly in the narrow leads attached to the ring [cf. Fig. 5.2 (b)]. Thus, the interference effect due to the inner loop is expected to be much larger than the one to the outer edge states and the Fourier transform peak corresponding to the latter orbit can be obscured by the larger peak due to the inner loop and the second harmonic of this peak, which also exists.

AB-type oscillations in high magnetic field were studied in this section. It was shown that the oscillation period increases with magnetic field, which can be attributed to a decreasing effective radius of the electron orbit. This can be explained by the edge states appearing in high magnetic field. Then, the edge states at the inner edge of the ring structure form a closed loop with B -dependent radius, being sensitive to the enclosed flux. Due to the narrow width of the leads, states at the inner and outer edge, respectively, can interact. Hence, the AB effect for the electrons circling at the inner edge is observable in the transmission through the ring, which is mainly obtained by the states at the outer edge.

The scattering between the inner and outer edge indicates potential fluctuations within the arms of the ring. These potential fluctuations can also suppress the coherence of transport for $B = 0$. This supports the assumption made in the previous section that only a few coherent modes exist, whereas many channels transmit incoherently.

5.5 Summary

Quantum mechanically, the phase of a particle wave function can be affected by many external parameters. Interference experiments have been used to demonstrate the phase difference between the individual partial waves. Such experiments were

performed on ring structures fabricated from HgTe QW samples to study phase effects present in this material. Like for various other semiconductor materials, Aharonov-Bohm-like oscillations were found in a magnetic field, which was applied perpendicular to the ring plane. These oscillations were used as a tool to identify other phase effects. In the presence of spin-orbit interaction, two additional contributions to the electron phase appear. The first one is the Aharonov-Casher phase, which is the electromagnetic dual to the AB phase. For the AC effect, the magnetic moment of a particle, e.g., the electron spin, couples to a vector potential of an electric field, e.g., due to the Rashba effect. Furthermore, the SO interaction gives rise to an effective magnetic field in the ring plane, which modulates the external magnetic field. The smooth variation of the orientation of the total magnetic field yields the geometric SO Berry phase. However, this phase effect is dominated by the AC phase and not directly observable.

In the absence of the external magnetic field, pure AC oscillations can be observed. Due to the non-linear dependence of the Rashba splitting on the wave vector k , no periodic behavior is obtained as a function of gate voltage. When the spin-orbit interaction is varied via the gate voltage for finite magnetic field, the maxima of the AB oscillations are split and shifted. The complex interference pattern can be attributed to the increasing contribution by the AC phase, which has opposite sign for parallel and anti-parallel orientation of the spin with respect to the magnetic field. This interpretation is confirmed by theoretical calculations, where a ring structure with one coherent mode and five additional non-coherent modes was assumed. While only the coherent mode contributes to the oscillatory signal, scattering between all modes is possible, affecting both the total conductance and the amplitude of the oscillations. In this model, an excellent agreement with the experimental observation is achieved. Thus, the presented results provide the first direct observation of the dynamical part of the AC phase. It should be mentioned that an influence of the SO interaction on the AB oscillations was observed recently for other materials with substantial SO interaction by several groups as well [129–131]. The most distinct features are reported in Ref. 130, where several periods of the

AC effect were demonstrated for an array of rings. In these experiments, a regular oscillation pattern was obtained as a function of gate voltage.

A surprising result was obtained for measurements in high magnetic fields, where AB oscillations were observed up to 16 T. When B increases, the frequency of the oscillations decreases. This is attributed to a decrease of the effective radius of the electron orbit. When the transport is dominated by edge states for large magnetic fields, only edge states passing one of the arms effectively will contribute to transport. A closed electron orbit exists due to the states at the inner edge of the ring. Thus, electrons in this loop enclose a magnetic flux and acquire an AB phase. If this orbit is coupled to the outer edge states due to the spatial overlap of the counter-propagating edge states, AB oscillations are observed as a superposition on the SdH oscillations in the longitudinal resistance. For increasing B , the inner edge states are shifted towards the center of the ring, which results in a decreasing effective radius. For $B > 8$ T, the inner edge states are finally located at the lithographical edge of the device. In this case, the effective electron radius corresponds to the inner radius of the device and does no longer depend on the strength of the external field.

Summary and Outlook

Within the scope of this thesis, spin related transport phenomena have been investigated in HgTe/Hg_{0.3}Cd_{0.7}Te quantum well structures. This material exhibits peculiar band structure properties, which result in a strong spin-orbit interaction of the Rashba type. An inverted band structure, i.e., a reversed ordering of the energy states in comparison to common semiconductors, is obtained for quantum well layers above a critical thickness. Furthermore, the band structure properties can be controlled in the experiments by moderate gate voltages. Most prominently, the type of carriers in HgTe quantum wells can be changed from *n* to *p* due to the narrow energy gap.

This unique transition is, in combination with the inverted band structure, the basis for the demonstration of a new state of matter, the Quantum Spin Hall state. This novel state is characterized by the existence of two one-dimensional spin-polarized edge states, while the Fermi level in the bulk is in the energy gap. In the QSH state, these two states counter-propagate at each edge, but elastic scattering is suppressed by time reversal symmetry. This results in a quantized conductance for both spin and charge transport. A charge conductance close to the expected quantized value of $2e^2/h$ has been observed for samples with characteristic dimensions below the inelastic mean free path. For larger samples, potential fluctuations have to be considered as a source of backscattering, which reduces the conductance. Backscattering can be caused by inelastic scattering of the QSH edge states and local conducting regions, where the counter-propagating edge states equilibrate. While temperature-dependent measurements have indicated that the latter mechanism is presumably

dominant, a detailed analysis of the scattering mechanisms can be seen as a future task. Studies of the length dependence of the QSH states may provide new insight.

Strong indication for the edge state transport was found in two distinct ways: First, the conductance of the QSH state is independent of the sample width. Second, a clear non-local signal emerges for the insulating regime. While both results imply edge state transport, the presented transport experiments can not provide absolute evidence of this concept. Thus, it is important to employ a method, which is suitable for a direct demonstration. In this context, a spatial mapping of the current flow in the QSH state might be a reasonable approach, e.g., by scanning gate measurements.

The protection of the QSH edge states by time reversal symmetry was verified by experiments in magnetic field. If the time reversal symmetry is broken by a B -field, elastic scattering becomes possible and conductance is significantly suppressed. The dominant mechanism is an orbital effect in a perpendicular field, while a smaller Zeeman-like effect is present for any field direction. For large perpendicular fields, a re-entrant quantum Hall state appears. This unique transport property is directly related to the non-trivial insulating state, which is the basis of the QSH effect.

In our experiments, the existence of the QSH state was successfully demonstrated for the first time and the presented results provide clear evidence for the charge transport properties of the QSH state. However, the spin properties are more difficult to address. This might be achieved in transport measurements by incorporating spin-sensitive barriers or, in different experimental approaches, by using optical methods or nano-SQUID techniques. Another option for transport experiments takes advantage of the spin Hall effect, which was also studied within this thesis.

Predominantly, the investigation of the spin Hall effect was motivated by the possibility to create and to detect pure spin currents and spin accumulation by means of a purely electrical experiment on an H-shaped nanostructures with large SO interaction. It has turned out that the SO splitting of the conduction band with respect to

the wave vector is too small for an observation of the SHE in the presented devices. But in contrast, a distinct signal attributed to the SHE has been detected for a p -type sample, where the k -difference is significantly larger. These results provide the first purely electrical demonstration of the SHE and SHE^{-1} in a semiconductor system.

A possibly more direct way to study the spin Hall effects, and spin transport in general, opens up when the spin properties of the QSH edge states are taken into account: If the two legs of an H-shaped device are controlled separately, one of them can be tuned to the QSH regime, while the other one is either n - or p -conducting. In such configuration, the spin-polarized QSH edge channels can be used either as spin-selective voltage probes or for the injection a pure spin current, depending on the actual choice of the current path through the device. If a spin-polarization of the QSH states is assumed in accordance to the theoretical prediction, the experimental results indicate the existence of both intrinsic SHE and SHE^{-1} independently of each other. However, further studies are required to rule out spurious effects and confirm the above interpretation.

When the QSH states injected a spin-polarized current into a conducting region, the precession of the spin due to the effective Rashba field has been observed. Both the spin-polarized injection and the manipulation of the spin orientation might be used for the realization of a spin-FET. Conveniently, no ferromagnetic contacts are required in such a sample, which is an obstacle of the realization of the initial proposal by Datta and Das.

Another approach to overcome the usage of ferromagnetic contacts for a spin-based FET relies on the interference in a ring structure. The transmission of the spin interference device proposed by Nitta *et al.* is governed by the Aharonov-Casher phase and the Berry phase, both due to the SO interaction. While the former is caused by the electric Rashba field, the latter appears due to the modulation of the magnetic field by the effective magnetic field. In the presented experiments, devices similar to the proposed ones were studied. The complex interference pattern of AB-like

oscillations as a function of external magnetic field and gate voltage clearly demonstrates the existence of phase effects induced by spin-orbit interaction. The observed dependence of the interference pattern on the Rashba splitting is attributed to the Aharonov-Casher phase, whereas effects due to the Berry phase remain unresolved. This interpretation is confirmed by theoretical calculations, where multi-channel transport through the device has been assumed in agreement with the experimental results. Thus, our experiments provide the first direct observation of the AC effect in semiconductor structures. If such samples are supposed to be used as a spin-interference FET like initially proposed, transmission has to be totally suppressed for destructive interference. However, this is only possible, if only a single mode exists in the ring, which is difficult to realize in HgTe samples.

In conclusion, HgTe quantum well structures have proven to be an excellent template for studying spin-related transport phenomena: The QSHE relies on the peculiar band structure of the material and the existence of both the SHE and the AC effect is a consequence of the substantial spin-orbit interaction. While convincing results have been obtained for the various effects, several questions can not be fully answered yet. Some of them may be addressed by more extensive studies on the devices discussed above. Other issues, however, ask, e.g., for further advances in sample fabrication or new approaches by different measurements techniques. Thus, future experiments may provide new, compelling insights for both the effects discussed in this thesis and, more generally, other spin-orbit related transport properties. Furthermore, the above effects may find application in various spintronic devices.

Zusammenfassung und Ausblick

Im Rahmen dieser Arbeit wurden spin-bezogene Transportphänomene an HgTe/Hg_{0.3}Cd_{0.7}Te-Quantentrogstrukturen untersucht. Dieses Materialsystem weist besondere Eigenschaften in der Bandstruktur auf, die zu einer starken Spin-Bahn-Wechselwirkung führen. Eine invertierte Bandstruktur, d.h. eine umgekehrte Anordnung der Energiezustände im Quantentrog im Vergleich zu herkömmlichen Halbleitermaterialien, ergibt sich, wenn die Dicke der Quantentrogsschicht einen kritischen Wert überschreitet. Außerdem können die Bandstruktureigenschaften im Experiment durch moderate Gatespannungen gezielt beeinflusst werden. Eine bedeutende Rolle spielt dabei, dass die Art der Ladungsträger im Quantentrog von n nach p verändert werden kann.

Dieser einzigartige Übergang bildet - in Zusammenspiel mit dem Auftreten der invertierten Bandstruktur - die Grundlage für den Nachweis eines neuartigen Zustands, des Quanten-Spin-Hall-(QSH-)Effekts. Dieser Zustand zeichnet sich dadurch aus, dass zwei eindimensionale spinpolarisierte Randkanäle existieren, während das Fermi-Niveau im Probeninneren in der Energielücke liegt. Im QSH-Zustand breiten sich die Ladungsträger in diesen beiden Randkanälen in entgegengesetzte Richtungen aus. Elastische Streuprozesse zwischen diesen Kanälen sind allerdings aufgrund der Zeitumkehrinvarianz verboten. Dies führt zu einer quantisierten Leitfähigkeit sowohl im Ladungs- als auch im Spintransport. Für den Ladungstransport wurde eine Leitfähigkeit nahe des erwarteten quantisierten Wertes von $2e^2/h$ gemessen, falls die charakteristischen Probenlängen nicht über die mittlere inelastische freie Weglänge hinausging. Für größere Proben müssen allerdings Potentialfluktuationen

nen berücksichtigt werden. Diese können Rückstreuung hervorrufen und verringern daher die Leitfähigkeit. Die Rückstreuung kann dabei durch inelastische Streuprozesse zwischen den gegenläufigen QSH-Kanälen verursacht werden oder durch das Auftreten von lokalen, leitenden Bereichen, in denen sich das Potential der QSH-Kanäle angleicht. Temperaturabhängige Messungen legen nahe, dass der letztere der genannten Streumechanismen dominiert. Eine detaillierte Untersuchung der Streumechanismen, die in diesem Punkt endgültige Klarheit verschaffen kann, steht allerdings noch aus. Dabei könnte die Ermittlung der Längenabhängigkeit der QSH-Zustände neue Erkenntnisse liefern.

Deutliche Anzeichen dafür, dass der Transport in der Tat in Randkanälen erfolgt, wurden in zwei voneinander unabhängigen Experimenten gefunden: Zum einen hängt die Leitfähigkeit nicht von der Breite der Proben ab. Zum anderen wird ein deutliches nicht-lokales Signal sichtbar, wenn die Probe in das QSH-Regime gebracht wird. Obwohl beide Ergebnisse deutliche Anzeichen für Transport mittels Randkanälen liefern, kann kein endgültiger Beweis erbracht werden. Es ist daher wichtig, geeignete Methoden für einen direkten Nachweis zu finden und anzuwenden. Eine sinnvolle Herangehensweise wäre in diesem Zusammenhang eine räumlich aufgelöste Abbildung des Stromflusses in der Probe, wie es z.B. bei *Scanning Gate*-Messungen möglich ist.

Die Erhaltung des Transports in den QSH-Kanälen aufgrund der Zeitumkehrinvarianz wurde durch Messungen im Magnetfeld bestätigt. Wenn die Zeitumkehrsymmetrie durch das Anlegen eines externen B -Feldes gebrochen wird, treten elastische Streuprozesse auf und die Leitfähigkeit verringert sich deutlich. Der dominierende Mechanismus ist dabei ein orbitaler Effekt, der durch ein senkrechtes Magnetfeld verursacht wird. Darüber hinaus existiert ein Zeeman-artiger Effekt für jede Ausrichtung des Feldes. Für starke Felder senkrecht zur Ebene der zweidimensionalen Elektronengases zeigt sich ein wieder-eintretender Quanten-Hall-Zustand. Dieses einzigartige Transportphänomen ist direkt mit dem nicht-trivialen isolierenden Zustand verknüpft, der die Grundlage des QSH-Effektes bildet.

In unseren Experimenten wurde zum ersten Mal die Existenz des QSH-Zustandes nachgewiesen. Dabei ermöglichen die Ergebnisse klare Aussagen über den Ladungstransport in den Randkanälen. Erkenntnisse über den Spintransport sind allerdings wesentlich schwieriger zu erzielen. In Transportmessungen könnten spinsensitive Barrieren neue Aufschlüsse liefern; bei einer anderen experimentellen Herangehensweise könnten auch optische Methoden oder Nano-SQUID-Techniken eingesetzt werden. Eine weitere Möglichkeit im Rahmen von Transportexperimenten nutzt den Spin-Hall-Effekt aus, der ebenfalls in dieser Arbeit untersucht wurde.

In erster Linie waren die Messungen zum Spin-Hall-Effekt (SHE) durch die Aussicht motiviert, reine Spinströme und eine Spinanreicherung in einem rein elektrischen Experiment an H-förmigen Nanostrukturen mit starker Spin-Bahn-Wechselwirkung hervorzurufen und nachzuweisen. Es zeigte sich, dass die Spin-Bahn-Aufspaltung des Leitungsbandes hinsichtlich des Wellenvektors zu schwach ist, um den SHE in den untersuchten Proben zu beobachten. In p -leitenden Strukturen mit wesentlich größerer k -Aufspaltung konnte hingegen ein deutliches Signal detektiert werden, das auf den SHE zurückzuführen ist. Diese Ergebnisse stellen den ersten, rein elektrischen Nachweis des SHE und des SHE^{-1} in einem Halbleitermaterial dar.

Ein möglicherweise direkterer Zugang zur Untersuchung der Spin-Hall-Effekte, und auch des Spintransports im Allgemeinen, ergibt sich, wenn die Spineigenschaften der QSH-Randkanäle berücksichtigt werden: Wenn die Transporteigenschaften der beiden Arme einer H-förmigen Struktur unabhängig voneinander kontrolliert werden, kann einer der beiden Arme in das QSH-Regime versetzt werden, während der andere n - oder p -leitend ist. In einer solchen Probenkonfiguration können die QSH-Randkanäle - abhängig vom exakten Verlauf des Stromes durch die Probe - entweder als spinselektive Spannungskontakte oder zur Injektion eines reinen Spinstroms verwendet werden. Wenn eine Spinpolarisation der Randkanäle entsprechend der theoretischen Modelle angenommen wird, weisen die experimentellen Ergebnisse sowohl den SHE als auch den SHE^{-1} unabhängig voneinander nach. Es sind allerdings noch weitere Messungen auf diesem Gebiet nötig, um anderweitige Ursachen

für die beobachteten Effekte ausschließen zu können und die obige Interpretation zu bestätigen.

Bei der Injektion eines spinpolarisierten Stroms aus den QSH-Kanälen in ein p -leitendes Gebiet konnte die Spinpräzession aufgrund des Rashbaeffektes beobachtet werden. Sowohl die spinpolarisierte Injektion als auch die gezielte Steuerung der Spinausrichtung können für die Verwirklichung eines Spin-Feldeffekttransistors (FET) verwendet werden. Günstigerweise kann dann auf ferromagnetische Metallkontakte verzichtet werden, die bisher eine Umsetzung des ursprünglich von Datta und Das vorgeschlagenen Modells verhindert haben.

Ein weiterer Ansatz, der die Verwendung von ferromagnetischen Kontakten in einem auf dem Spin basierenden FET überflüssig macht, beruht auf der Interferenz in Ringstrukturen. Die Transmission in einem Spin-Interferenz-Bauteil, wie es von Nitta *et al.* vorgeschlagen wurde, wird über die Aharonov-Casher-(AC)-Phase und die Berry-Phase gesteuert, die beide aufgrund der Spin-Bahn-Wechselwirkung auftreten. Während erstere durch das elektrische Rashba-Feld verursacht wird, tritt letztere aufgrund einer Modulation der Magnetfeldausrichtung durch das effektive Feld der Spin-Bahn-Wechselwirkung auf. Der Aufbau der hier untersuchten Proben ähnelt dem ursprünglich vorgeschlagenen Design. Das komplexe Interferenzmuster der AB-ähnlichen Oszillationen, das sich in Abhängigkeit vom externen Magnetfeld und der Gatespannung ergibt, weist eindeutig Phaseneffekte nach, die durch die Spin-Bahn-Wechselwirkung hervorgerufen werden. Die beobachtete Abhängigkeit des Interferenzmusters von der Rashba-Aufspaltung wird der Aharonov-Casher-Phase zugeordnet, wohingegen Effekte aufgrund der Berry-Phase nicht aufgelöst werden können. Diese Interpretation wird durch theoretischer Berechnungen bestätigt, bei denen - in Übereinstimmung mit den experimentellen Ergebnissen - Transport mittels mehrerer Moden angenommen worden ist. Somit liefern unsere Experimente den ersten direkten Nachweis des AC-Effektes in Halbleiter-Strukturen. Wenn solche Strukturen eine Anwendung als Spin-Interferenz-FET finden sollen, wie es ursprünglich vorgeschlagen wurde, muss im Falle destruktiver Interferenz die Trans-

mission vollständig unterdrückt werden. Dies ist allerdings nur möglich, wenn nur eine einzige Mode im Ring vorliegt, was in HgTe-Proben schwer zu erreichen ist.

Abschließend lässt sich festhalten, dass HgTe-Quantentrogstrukturen sich als herausragendes System erwiesen haben, um spin-bezogene Transportphänomene zu untersuchen: Der QSHE beruht auf den besonderen Eigenschaften der Bandstruktur und sowohl der SHE als auch der Aharonov-Casher-Effekt sind eine Folge der ausgeprägten Spin-Bahn-Wechselwirkung. Obwohl überzeugende Erkenntnisse im Hinblick auf die verschiedenen Effekte gewonnen wurden, sind einige Gesichtspunkte noch nicht vollständig geklärt. Einige Fragen können eventuell durch umfangreichere Untersuchungen an schon vorhandenen Proben beantwortet werden. Andere wiederum erfordern z.B. weitere Fortschritte in der Probenherstellung oder neue Herangehensweisen mittels anderer experimenteller Methoden. Somit können zukünftige Experimente neue, fesselnde Einsichten mit sich bringen, sowohl in die hier untersuchten Effekte als auch im Allgemeinen in andere auf der Spin-Bahn-Wechselwirkung beruhende Transporteigenschaften. Darüber hinaus können die obigen Effekte in verschiedenartigen spintronischen Bauteilen eingesetzt werden.

Bibliography

- [1] S. A. Wolf, D. D. Awschalom, R. A. Buhrman, J. M. Daughton, S. von Molnár, M. L. Roukes, A. Y. Chtchelkanova, and D. M. Treger, *Science* **294**, 1488 (2001).
- [2] I. Zutíć, J. Fabian, and S. D. Sarma, *Rev. Mod. Phys.* **76**, 323 (2004).
- [3] G. Schmidt, D. Ferrand, L. W. Molenkamp, A. T. Filip, and B. J. van Wees, *Phys. Rev. B* **62**, R4790 (2000).
- [4] T. Dietl, H. Ohno, F. Matsukura, J. Cibert, and D. Ferrand, *Science* **287**, 1019 (2000).
- [5] E. I. Rashba, *Phys. Rev. B* **62**, R16267 (2000).
- [6] Y. A. Bychkov and E. I. Rashba, *Pis'ma Zh. Eksp. Teor. Fiz.* **39**, 66 (1984), [*JETP Lett.* **39**, 78 (1984)].
- [7] M. Khodas, A. Shekhter, and A. M. Finkel'stein, *Phys. Rev. Lett.* **92**, 086602 (2004).
- [8] U. Zülicke, *Appl. Phys. Lett.* **85**, 2616 (2004).
- [9] L. P. Rokhinson, V. Larkina, Y. B. Lyanda-Geller, L. N. Pfeiffer, and K. W. West, *Phys. Rev. Lett.* **93**, 146601 (2004).
- [10] S. Souma and B. K. Nikolić, *Phys. Rev. Lett.* **94**, 106602 (2005).
- [11] J. E. Hirsch, *Phys. Rev. Lett.* **83**, 1834 (1999).

-
- [12] S. Murakami, N. Nagaosa, and S. C. Zhang, *Science* **301**, 1348 (2003).
- [13] J. Sinova, D. Culcer, Q. Niu, N. A. Sinitsyn, T. Jungwirth, and A. H. MacDonald, *Phys. Rev. Lett.* **92**, 126603 (2004).
- [14] M. Berry, *Proc. R. Soc. Lond. A* **392**, 45 (1984).
- [15] Y. Aharonov and A. Casher, *Phys. Rev. Lett.* **53**, 319 (1984).
- [16] J. Nitta, F. E. Meijer, and H. Takayanagi, *Appl. Phys. Lett.* **75**, 695 (1999).
- [17] S. Datta and B. Das, *Appl. Phys. Lett.* **56**, 665 (1990).
- [18] C. L. Kane and E. J. Mele, *Phys. Rev. Lett.* **95**, 226801 (2005).
- [19] B. A. Bernevig and S. C. Zhang, *Phys. Rev. Lett.* **96**, 106802 (2006).
- [20] X. C. Zhang, A. Pfeuffer-Jeschke, K. Ortner, V. Hock, H. Buhmann, C. R. Becker, and G. Landwehr, *Phys. Rev. B* **63**, 245305 (2001).
- [21] Y. S. Gui, C. R. Becker, N. Dai, J. Liu, Z. J. Qiu, E. G. Novik, M. Schäfer, X. Z. Shu, J. H. Chu, H. Buhmann, and L. W. Molenkamp, *Phys. Rev. B* **70**, 115328 (2004).
- [22] J. Hinz, H. Buhmann, M. Schäfer, V. Hock, C. R. Becker, and L. W. Molenkamp, *Semicond. Sci. Technol.* **21**, 501 (2006).
- [23] B. A. Bernevig, T. L. Hughes, and S. C. Zhang, *Science* **314**, 1757 (2006).
- [24] Y. K. Kato, R. C. Myers, A. C. Gossard, and D. D. Awschalom, *Science* **306**, 1910 (2004).
- [25] J. Wunderlich, B. Kaestner, J. Sinova, and T. Jungwirth, *Phys. Rev. Lett.* **94**, 047204 (2005).
- [26] V. Sih, R. C. Myers, Y. K. Kato, W. H. Lau, A. C. Gossard, and D. D. Awschalom, *Nature Physics* **1**, 31 (2005).

-
- [27] E. Saitoh, M. Ueda, H. Miyajima, and G. Tatara, *Appl. Phys. Lett.* **88**, 182509 (2006).
- [28] S. O. Valenzuela and M. Tinkham, *Nature* **443**, 176 (2006).
- [29] T. Kimura, Y. Otani, T. Sato, S. Takahashi, and S. Maekawa, *Phys. Rev. Lett.* **98**, 156601 (2007).
- [30] E. M. Hankiewicz, L. W. Molenkamp, T. Jungwirth, and J. Sinova, *Phys. Rev. B* **70**, 241301 (2004).
- [31] A. F. Morpurgo, J. P. Heida, T. M. Klapwijk, B. J. van Wees, and G. Borghs, *Phys. Rev. Lett* **80**, 1050 (1998).
- [32] J. B. Yau, E. P. De Poortere, and M. Shayegan, *Phys. Rev. Lett.* **88**, 146801 (2002).
- [33] M. J. Yang, C. H. Yang, and Y. B. Lyanda-Geller, *Europhys. Lett.* **66**, 826 (2004).
- [34] V. Daumer, Ph.D. thesis, Universität Würzburg (2005).
- [35] J. R. Meyer, C. A. Hoffman, and F. J. Bartoli, *II-VI Semiconductor Compounds* (World Scientific, Singapore, 1993), chap. Novel Electronic Processes in Mercury-Based Superlattices, pp. 301–344, and references therein.
- [36] V. F. Radantsev, V. V. Kruzhaev, and G. I. Gulaev, *Physica E* **20**, 396 (2004).
- [37] K. C. Woo, S. Rafol, and J. P. Faurie, *Phys. Rev. B* **34**, 5996 (1986).
- [38] K. C. Woo, S. Rafol, and J. P. Faurie, *Surface Science* **196**, 665 (1988).
- [39] M. Schultz, F. Heinrichs, U. Merkt, T. Colin, T. Skauli, and S. Løvold, *Semicond. Sci. Technol.* **11**, 1168 (1996).
- [40] A. Pfeuffer-Jeschke, Ph.D. thesis, Universität Würzburg (2000).

-
- [41] E. G. Novik, A. Pfeuffer-Jeschke, T. Jungwirth, V. Latussek, C. R. Becker, G. Landwehr, H. Buhmann, and L. W. Molenkamp, *Phys. Rev. B* **72**, 035321 (2005).
- [42] M. Schultz, U. Merkt, A. Sonntag, U. Rössler, R. Winkler, T. Colin, P. Helgesen, T. Skauli, and S. Løvold, *Phys. Rev. B* **57**, 14772 (1998).
- [43] G. Dresselhaus, *Phys. Rev.* **100**, 580 (1955).
- [44] F. J. Ohkawa and Y. Uemura, *J. Phys. Soc. Jpn.* **37**, 1325 (1974).
- [45] G. Lommer, F. Malcher, and U. Rössler, *Phys. Rev. Lett.* **60**, 728 (1988).
- [46] J. Luo, H. Munekata, F. F. Fang, and P. J. Stiles, *Phys. Rev. B* **41**, 7685 (1990).
- [47] H. L. Störmer, Z. Schlesinger, A. Chang, D. C. Tsui, A. C. Gossard, and W. Wiegmann, *Phys. Rev. Lett.* **51**, 126 (1983).
- [48] D. Stein, K. von Klitzing, and G. Weimann, *Phys. Rev. Lett.* **51**, 130 (1983).
- [49] R. Winkler and U. Rössler, *Phys. Rev. B* **48**, 8918 (1993).
- [50] R. Winkler, *Phys. Rev. B* **62**, 4245 (2000).
- [51] G. Lommer, F. Malcher, and U. Rössler, *Phys. Rev. B* **32**, 6965 (1985).
- [52] A. Därr, J. P. Kotthaus, and T. Ando, in *Proceedings of the 13th International Conference on the Physics of Semiconductors*, edited by F. G. Fumi (North-Holland, Amsterdam, 1976), p. 774.
- [53] F. Malcher, G. Lommer, and U. Rössler, *Superlattices and Microstructures* **2**, 267 (1986).
- [54] E. A. de Andrade e Silva, G. C. L. Rocca, and F. Bassani, *Phys. Rev. B* **55**, 16293 (1997).
- [55] P. Pfeffer and W. Zawadzki, *Phys. Rev. B* **59**, R5312 (1999).

-
- [56] D. Grundler, Phys. Rev. Lett. **84**, 6074 (2000).
- [57] W. Yang and K. Chang, Phys. Rev. B **73**, 113303 (2006).
- [58] M. A. Skvortsov, JETP Lett. **67**, 133 (1998), [Pis'ma Zh. Eksp. Teor. Fiz. **67**, 118 (1998)].
- [59] J. Nitta, T. Akazaki, H. Takayanagi, and T. Enoki, Phys. Rev. Lett. **78**, 1335 (1997).
- [60] G. Engels, J. Lange, T. Schäpers, and H. Lüth, Phys. Rev. B **55**, R1958 (1997).
- [61] C.-M. Hu, J. Nitta, T. Akazaki, H. Takayanagi, J. Osaka, P. Pfeffer, and W. Zawadzki, Phys. Rev. B **60**, 7736 (1999).
- [62] F. Goschenhofer, J. Gerschütz, A. Pfeuffer-Jeschke, R. Hellmig, C. R. Becker, and G. Landwehr, J. Electron. Mater. **27**, 532 (1998).
- [63] C. R. Becker, C. Brüne, M. Schäfer, A. Roth, H. Buhmann, and L. W. Molenkamp, phys. stat. sol. (c) **4**, 3382 (2007).
- [64] V. Daumer, I. Golombek, M. Gbordzoe, E. G. Novik, V. Hock, C. R. Becker, H. Buhmann, and L. W. Molenkamp, Appl. Phys. Lett. **83**, 1376 (2003).
- [65] A. K. Geim and K. S. Novoselov, Nature Materials **6**, 183 (2007), and references therein.
- [66] L. Esaki, Phys. Rev. **109**, 603 (1958).
- [67] A. Pfeuffer-Jeschke, F. Goschenhofer, S. J. Cheng, V. Latussek, J. Gerschütz, C. R. Becker, R. R. Gerhardts, and G. Landwehr, Physica B **256-258**, 486 (1998).
- [68] C. R. Becker, Y. S. Gui, J. Liu, V. Daumer, K. Ortner, V. Hock, A. Pfeuffer-Jeschke, H. Buhmann, and L. W. Molenkamp, phys. stat. sol. (b) **229**, 775 (2001).
- [69] R. J. Haug, Semicond. Sci. Technol. **8**, 131 (1993).

-
- [70] L. Shubnikov and W. J. de Haas, *Leiden Commun.* **207**, 3 (1930).
- [71] K. von Klitzing, G. Dorda, and M. Pepper, *Phys. Rev. Lett.* **45**, 494 (1980).
- [72] S. Murakami, N. Nagaosa, and S. C. Zhang, *Phys. Rev. Lett.* **93**, 156804 (2004).
- [73] C. Wu, B. A. Bernevig, and S. C. Zhang, *Phys. Rev. Lett.* **96**, 106401 (2006).
- [74] C. L. Kane and E. J. Mele, *Phys. Rev. Lett.* **95**, 146802 (2005).
- [75] D. J. Thouless, M. Kohmoto, M. P. Nightingale, and M. den Nijs, *Phys. Rev. Lett.* **49**, 405 (1982).
- [76] S. Murakami, *Phys. Rev. Lett.* **97**, 236805 (2006).
- [77] M. Onoda, Y. Avishai, and N. Nagaosa, *Phys. Rev. Lett.* **98**, 076802 (2007).
- [78] C. Xu and J. E. Moore, *Phys. Rev. B* **73**, 045322 (2006).
- [79] S. Murakami, S. Iso, Y. Avishai, M. Onoda, and N. Nagaosa, *cond-mat/07053696*.
- [80] L. Fu and C. Kane, *cond-mat/0611341*.
- [81] M. Büttiker, *Phys. Rev. Lett.* **57**, 1761 (1986).
- [82] Z. J. Qiu, Y. S. Gui, T. Lin, J. Lu, N. Tang, B. Shen, N. Dai, and J. H. Chu, *Solid State Comm.* **131**, 37 (2004).
- [83] X. Dai, T. L. Hughes, X. L. Qiang, Z. Fang, and S. C. Zhang, *cond-mat/07051516*.
- [84] R. Danneau, O. Klochan, L. H. Ho, A. P. Micolich, M. Y. Simmons, A. R. Hamilton, M. Pepper, D. A. Ritchie, and U. Zülicke, *Phys. Rev. Lett.* **97**, 026403 (2006).
- [85] S. J. Papadakis, E. P. De Poortere, M. Shayegan, and R. Winkler, *Phys. Rev. Lett.* **84**, 5592 (2000).

-
- [86] Supporting Online Material of Ref. 23.
- [87] B. L. Altshuler, A. G. Aronov, and D. E. Khmel'nitsky, *J. Phys. C: Solid State Phys.* **15**, 7367 (1982).
- [88] M. I. Dyakonov and V. I. Perel, *Phys. Lett. A* **35**, 459 (1971).
- [89] P. Zhang and Q. Niu, cond-mat/0406436.
- [90] E. M. Hankiewicz, J. Li, T. Jungwirth, Q. Niu, S. Q. Shen, and J. Sinova, *Phys. Rev. B* **72**, 155305 (2005).
- [91] H. A. Engel, E. I. Rashba, and B. I. Halperin, cond-mat/0603306.
- [92] N. F. Mott and H. S. W. Massey, *The Theory of Atomic Collisions* (Oxford University Press, London, 1965).
- [93] M. I. Dyakonov and V. I. Perel, *JETP Lett.* **13**, 467 (1971).
- [94] L. Berger, *Phys. Rev. B* **2**, 4559 (1970).
- [95] B. A. Bernevig and S. C. Zhang, *Phys. Rev. Lett.* **95**, 016801 (2005).
- [96] J. Sinova, S. Murakami, S. Q. Shen, and M. S. Choi, *Solid State Comm.* **138**, 214 (2006).
- [97] E. M. Hankiewicz, private communication.
- [98] J. Sinova, private communication.
- [99] M. G. Pala, M. Governale, J. König, and U. Zülicke, *Europhys. Lett.* **65**, 850 (2004).
- [100] Y. Aharonov and D. Bohm, *Phys. Rev.* **115**, 485 (1959).
- [101] W. Ehrenberg and R. E. Siday, *Proc. R. Soc. Lond. B* **62**, 8 (1949).
- [102] R. G. Chambers, *Phys. Rev. Lett.* **5**, 3 (1960).

-
- [103] A. Cimmino, G. I. Opat, A. G. Klein, H. Kaiser, S. A. Werner, M. Arif, and R. Clothier, *Phys. Rev. Lett.* **63**, 380 (1989).
- [104] A. Görlitz, B. Schuh, and A. Weis, *Phys. Rev. A* **51**, R4305 (1995).
- [105] K. Zeiske, G. Zinner, F. Riehle, and J. Helmcke, *Appl. Phys. B* **60**, 205 (1995).
- [106] Y. Aharonov and J. Anandan, *Phys. Rev. Lett.* **58**, 1593 (1987).
- [107] A. Tomita and R. Y. Chiao, *Phys. Rev. Lett.* **57**, 937 (1986).
- [108] G. Timp, A. M. Chang, J. E. Cunningham, T. Y. Chang, P. Mankiewich, R. Behringer, and R. E. Howard, *Phys. Rev. Lett.* **58**, 2814 (1987).
- [109] Y. Meir, Y. Gefen, and O. Entin-Wohlman, *Phys. Rev. Lett.* **63**, 798 (1989).
- [110] H. Mathur and A. D. Stone, *Phys. Rev. Lett.* **68**, 2964 (1992).
- [111] Y. Oreg and O. Entin-Wohlman, *Phys. Rev. B* **46**, 2393 (1992).
- [112] T. Z. Qian and Z. B. Su, *Phys. Rev. Lett.* **72**, 2311 (1994).
- [113] A. G. Aronov and Y. B. Lyanda-Geller, *Phys. Rev. Lett.* **70**, 343 (1993).
- [114] D. Frustaglia and K. Richter, *Foundations of Physics* **31**, 399 (2001).
- [115] A. Stern, *Phys. Rev. Lett.* **68**, 1022 (1992).
- [116] S. A. van Langen, H. P. A. Knops, J. C. J. Paasschens, and C. W. J. Beenakker, *Phys. Rev. B* **59**, 2102 (1999).
- [117] M. Popp, D. Frustaglia, and K. Richter, *Phys. Rev. B* **68**, 041303 (2003).
- [118] D. Loss, H. Schoeller, and P. M. Goldbart, *Phys. Rev. B* **48**, 15218 (1993).
- [119] D. Loss, H. Schoeller, and P. M. Goldbart, *Phys. Rev. B* **59**, 13328 (1999).
- [120] H. A. Engel and D. Loss, *Phys. Rev. B* **62**, 10238 (2000).
- [121] H. D. Raedt, *Phys. Rev. Lett.* **83**, 1700 (1999).

-
- [122] A. G. Wagh and V. C. Rakhecha, Phys. Rev. Lett. **90**, 119703 (2003).
- [123] A. G. Mal'shukov and K. A. Chao, Phys. Rev. Lett. **90**, 179701 (2003).
- [124] S. Souma and B. K. Nikolić, Phys. Rev. B **70**, 195346 (2004).
- [125] F. E. Meijer, A. F. Morpurgo, and T. M. Klapwijk, Phys. Rev. B **66**, 033107 (2002).
- [126] B. Molnár, F. M. Peeters, and P. Vasilopoulos, Phys. Rev. B **69**, 155335 (2004).
- [127] D. Frustaglia and K. Richter, Phys. Rev. B **69**, 235310 (2004).
- [128] F. E. Camino, W. Zhou, and V. J. Goldman, Phys. Rev. Lett. **72**, 155313 (2005).
- [129] T. Koga, Y. Sekine, and J. Nitta, Phys. Rev. B **74**, 041302 (2006).
- [130] T. Bergsten, T. Kobayashi, Y. Sekine, and J. Nitta, Phys. Rev. Lett. **97**, 196803 (2006).
- [131] B. Grbić, R. Leturcq, T. Ihn, K. Ensslin, D. Reuter, and A. D. Wieck, Phys. Rev. Lett. **99**, 176803 (2007).

Acknowledgements

The results of scientific research, which are presented within the scope of this thesis, would not have been possible without assistance of many other people. So I wish to thank everyone, who supported me and contributed to this work:

- Prof. Dr. Laurens W. Molenkamp gave me not only the possibility to work at the Lehrstuhl für Experimentelle Physik III (EP3) and use the excellent equipment. He also provided a lot of input during various discussions, leading towards new ideas and experiments.
- Prof. Dr. Hartmut Buhmann supervised my work in a great way: he was always ready to discuss the progress of the experiments and develop new ideas, and allowed me to work independently on the project at the same time.
- Prof. Dr. Yong-Shen Gui and Dr. Volker Daumer introduced me to the peculiarities of transport experiments on HgTe and pioneered some of presented results.
- Ralf Scheibner was always willing to give good advice on low-temperature transport.
- Anna Tschetschetkin, Joachim Schneider and Steffen Wiedmann were significantly involved in the experiments presented in this thesis, either by assisting in the lab or by discussing the results and asking the right questions to improve the understanding of the observations.
- Andreas Roth and Erich Schirmacher did an excellent job in the fabrication of nanostructures and provided an ongoing supply of devices.

- Dr. Charles R. Becker, Christoph Brüne and Matthias Schäfer permanently improved the MBE growth, achieving sample properties undreamed-of at the beginning of my work.
- All former and current members of the Quantum Transport group, whether named above or unnamed, participated in numberless fruitful discussions and contributed to the pleasant atmosphere for everyday's work.
- Prof. Dr. Jairo Sinova and Dr. Ewelina M. Hankiewicz established the theoretical calculations, which were useful for both the SHE and the AC effect.
- Prof. Dr. Shou-Cheng Zhang, Xiao-Liang Qi, Taylor Hughes and Chao-Xing Liu provided the theoretical basis of the QSHE and were eager to discuss our experiments in this field.
- Dr. Alena Astakhova performed some of the band structure calculations included in this thesis.
- Roland Ebert not only fixed various problems with the cryostats, but also shared his extensive knowledge on cryo-technology. He and Gerd Manger also supplied the liquid helium necessary for the low-temperature experiments.
- Dr. Tanja Borzenko and Volkmar Hock helped to solve smaller and bigger problems in the cleanroom.
- Steffen Vierheilig proofread the thesis attentively.
- All members of EP3 contributed to my work in various situations in a lot of different ways.
- Last but not least: My parents supported me my entire life. Their encouragement was essential to my personal development.

Curriculum Vitae

NAME		Markus König
GEBOREN AM		20. Oktober 1976
IN		Würzburg
STAATSANGEHÖRIGKEIT		deutsch
PROMOTION	2003 - 2007	Promotion an der Julius-Maximilians-Universität Würzburg, wissenschaftlicher Mitarbeiter am Lehrstuhl für Experimentelle Physik III
STUDIUM	1997 - 2002	Physik (Diplom) an der Julius-Maximilians-Universität Würzburg Diplomarbeit am Lehrstuhl für Experimentelle Physik III: " <i>Transportuntersuchungen an Halbleiter-Heterostrukturen</i> " (2002)
ZIVILDIENST	1996 - 1997	Johanniter-Unfall-Hilfe Würzburg
SCHULISCHE AUSBILDUNG	1987 - 1996	Städt. Schönborngymnasium Würzburg, Abschluss: Allgemeine Hochschulreife
	1983 - 1987	Steinbachtal-Grundschule Würzburg

Würzburg, den 20. Dezember 2007

Markus König